ISSN 1343-361X

Readout

HORIBA Technical Reports

ENGLISH EDITION
No. 38
May 2011

America

HORIBA

http://www.horiba.com/publications/readout/

Readout
HORIBA Technical Reports
English Edition No.38
May 2011

HORIBA Group conducts R&D not only at Japanese Headquarters but also American and European group companies. We hope this issue of HORIBA Readout, featuring the research and technological development in our US companies, shows that HORIBA group is responding to the various needs in this fast-advancing world, pursuing our customers' satisfaction.

In the fresh May breeze by the Chikuma river, I encountered and captivated by the sweeping view of a vivid yellow carpet woven from fresh field mustard. So close to human habitat, clean air and clear stream run. Harmony between people and nature never ceases to impress me.
-Photographer Hideo Matsui (member of NIKA Association of Photographers)

Name of the book

This book is named "Readout" in the hope that "the products and technology we have created and developed will be read out and so become widely known".

America

Foreword

Technology - Responding to Social Needs

Masayuki Adachi

Senior Corporate Officer
General Manager, R&D Division
HORIBA, Ltd.
(former president and CEO of HORIBA International Corporation, U.S.A.)
Doctor of Engineering

After the Lehman collapse and the economic implosion, U.S. has been implementing major remedies for recovery, such as the long-lasting ultra-low interest rate policy and the government stimulus bills. As a result, recent U.S. economy has been characterized by improved corporate performance, coupled with continuing high unemployment. During this same period, U.S. government spending increased enormously in an effort to counterbalance the downturn in consumer spending, in hopes of stimulating the U.S. economy. The spending far in excess of the levels of tax revenue consequently generated massive annual deficits, which imposes considerable cut on 2011 U.S. Federal Budget.

The budget bill was eventually passed on April 14, 2011, far later than the original deadline. The late signing and the huge cuts will impact the funding for science and technology in the U.S. when high energy and raw material costs are beginning to affect businesses.

Regardless of such delay and cuts in the U.S. budget, there are great needs for technical improvements in the energy sector, in order to conserve resources and protect environment. With advancement in technologies, the economy in Michigan is recovering, though gradually. Both General Motors and Ford are steadily rebuilding and releasing new vehicles with state-of-the-art technologies, such as hybrid, plug-in, full electric, down-sizing, and high efficiency transmission systems. The petroleum industry is also experiencing the shift to shale oil, which is reducing the import to below 50%.

In the medical sector, the health care reform in the U.S. was enacted nationally in 2010 by the passage of two bills: the Patient Protection and Affordable Care Act (PPACA), and the Health Care and Education Reconciliation Act. With these changes, the industry will face significant transformation in political, regulatory, economic, and scientific environments. No one for sure knows what will happen in detail but it is obvious that, with an increase in patient population, diagnostic testing must satisfy the pressing needs for improved automation and higher throughput of the medical instruments.

Much of the innovation in the U.S. is in information technology, biological and pharmaceutical sciences with venture capital investment at record levels in these fields. Furthermore, in IT sector, it has been announced that five new semiconductor fabs will be built in the U.S. over the next few years on the initiative of Samsung, Intel, and Global Foundries. Similar to the discussion above, there will be demands for higher automation, precision and throughput in the semiconductor manufacturing.

And finally, the overall scientific instrumentation is continuing to play an important role in security, safety, health, food and agriculture fields. In spite of the significant cuts in government budget, more accurate identification of chemical compounds is strongly required in the ultra low concentration with a minimum amount of samples.

This issue of Readout features HORIBA group technologies in the U.S., bringing you the latest discussions for all the application segments of HORIBA. Despite the challenging local, economical and political environment, science and technology in U.S. are rapidly progressing everyday. Our team in HORIBA U.S.A. pledges to provide better and practical solutions to the industry and customers to innovate on the process and accelerate the advancement by fully utilizing our expertise and intellectual assets.

Review

The Conflict between Energy and Environmental Quality

Prof. G. Scott Samuelsen
University of California, Irvine
Professor Mechanical, Aerospace and Environmental Engineering
Director National Fuel Cell Research Center
Ph. D.

The 20th century is a period of remarkable energy technology advances that society today embraces and expects as essential for the quality of life. In parallel, a conflict has evolved between the utilization of energy resources and the quality of the environment. The current paradigm is not sustainable and major changes are not only needed, but arguably obligatory for the 21st century. The breadth of the changes anticipated is remarkable, encompassing automobile fuel, the automobile power plant, the generation of electricity, the utilization of electricity, mobility in personal transport, and the design and operation of buildings. The recognition that these changes are essential has taken fifty years through an intertwined matrix of advancing technology, political process, public policy, economics, and social behavior. The efficacy with which these changes will occur depends on the extent to which this matrix can be managed.

20世紀は，エネルギー技術が目覚しい進歩を遂げた時代であった。こうしたエネルギー技術の進歩は，生活水準を維持するために不可欠なものと信じられている。この進歩と同時に，エネルギー需要の増加と自然環境の質との対峙が生じている。現在の社会のパラダイムは持続可能なものではない。21世紀においては大きな変化が求められ，実際にエネルギー供給と利用の転換が不可避であると考えられる。自動車燃料，自動車の動力源，発電，電力利用，個人の移動手段，建築物の設計と運営など，極めて幅広い分野にわたるエネルギー技術の革新が予測される。先進技術，政策決定，公共政策，経済，社会的行動が絡み合ったマトリクスの中で，この革新が必要不可欠であると認識されるまで半世紀を要した。持続可能なエネルギー技術の革新がもたらす効果は，このマトリクスをどれだけ巧みに運用できるかにかかっている。

The Conflict

The world's conflict between ENERGY and ENVIRONMENTAL QUALITY is worsening and in crisis.

Society relies on ENERGY for both economic well being and mobility, and relies on ENVIRONMENTAL QUALITY for quality of life, the health of the public, and the health of the earth. The thirst for ENERGY is deteriorating ENVIRONMENTAL QUALITY at a rapidly increasing rate. Like a cancer or an addiction, denial preoccupies much of the world opinion and precludes, today, a systematic and unified response. The cancer, at one

time treatable with a high probability of healing, is today progressing at a rate that outpaces any politically acceptable treatment. Resolution will require an unusual courage by governing leaders. This notwithstanding, examples of proactive action are increasing in response to a discovery of increasing symptoms and growing recognition that the future health of the earth is, in fact, in crisis. California's AB-32[*1)] Act is the first major test. Remarkably,[*2)] the citizens of California recently affirmed the leadership of the California Legislature on this issue by rejecting a proposition designed to suspend the Act.[*3)] If successful, AB 32 will set a needed example for the United States and other similarly positioned countries.

*1 : Assembly Bill 32: A law passed by the California Legislature in 2006 to reduce the annual emission of carbon dioxide (CO_2). http://www.arb.ca.gov/cc/ab32/ab32.htm

*2 : "Remarkable:" Worthy of notice or attention; notably or conspicuously unusual; extraordinary.

*3 : Proposition 23: A proposition ("California Jobs Initiative") on the 2010 General Election California Ballot (November).

The Evidence

Smog.

Evidence of the conflict between ENERGY and ENVIRONMENTAL QUALITY was first witnessed on a major scale in 1948 when 20 lost their lives and thousands fell ill over five days of an exceptional atmospheric loading of particulate and oxides of sulfur in Donora, Pennsylvania. The reducing brew inflicted injury to the throat (through the formation of sulfuric acid) and the lung (by the transport of particulate laden with dilute sulfuric acid deep into the respiratory tract). The Donora incident was one of two major air pollution "episodes" where deaths were directly a result of the exposure. The second occurred in 1952 when thousands lost their lives in a London fog. The episodes established that coal, used to fuel boilers and furnaces for heating homes and businesses (London) or producing steel (Donora), was the source of the killer "smog" (coined as a combination of "smoke" and "fog").

Photochemical Oxidant.

A second major source of evidence for the conflict was chronicled by the Los Angeles Times in 1943 noting that a gray haze was "troubling" the city. While not responsible for recorded deaths, the atmospheric pollution was associated with stinging eyes, wheezing throats, shortness of breath, and an undesirable degradation in visibility. A decade later, in 1952, Professor Arie Haagen-smit at the California Institute of Technology established the

atmospheric photochemistry that gives rise to this oxidizing atmosphere. He demonstrated in a 72 liter flask that two pollutants from combustion, oxides of nitrogen (NO_x) and hydrocarbons (H_xC_y), react in the presence of the early morning sunlight to generate ozone, other oxidants (e.g., peroxyacelnitrates), and a gray haze. A few years later, a research group at the Stanford Research Institute established that the combustion process associated with the generation of electricity and the propulsion of automobiles was the principal source of the pollutants. Automobiles were also identified as a source of carbon monoxide (CO), a colorless and odorless pollutant that accumulates in the still of the morning commute hour to affect the health of a large population of unsuspecting citizens.

Criteria Pollutants.

During this period a formal distinction was made between "contaminants" in the atmosphere (i.e., chemical species that either are not present in the virgin atmosphere or increase the concentration of chemical species already present in the virgin atmosphere) and "pollutants" (i.e., contaminants that have a demonstrated adverse effect on the public health). The first "pollutant" designation was based on the nuisance of oxidant (e.g., visibility degradation, shortness of breath, stinging eyes, wheezing) and led to the first controls on automobiles and power plant pollutant emissions in California in the 1960's. The first pollutant emission controls directed to the automobile at the national level followed in 1968.

Beginning with the decade of the 1960's, health effects data were reviewed and additional studies were conducted, all of which are documented in a series of "Air Quality Criteria" documents, one for each of the criteria pollutants: Ozone (the principal component of photochemical oxidant), CO, SO_x, NO_x, Particulate, and Lead.

> Mother nature is incredibly subtle and powerful. On the one hand, fossil fuel is provided to satisfy the energy thirst of society. On the other hand, Mother Nature assigns a toxicity to trace species that, through environmental impact, is a gentle reminder for restraint.[*4)]

*4 : G.S. Samuelsen, THE RESPONSIBILITY OF SCIENTISTS AND ENGINEERS TO THE STEWARDSHIP OF THE EARTH AND ITS ENVIRONMENT (1990), Readout, No. 1, p. 4-7, July

Clean Air Act.

The experiences and discoveries in California during the 1960's set the stage for the Clean Air Act of 1970, led by Senator Edmund Muskie of Minnesota

and signed into law by President Richard M. Nixon in December. The Act established "National Air Quality Standards" based on the criteria pollutant documents, rolled back emissions from automobiles by 90% within five to six years, and created the U.S. Environmental Protection Agency. Research in the air chemistry, the public health impacts, and the meteorology associated with air pollution accelerated during the decade, and dramatic gains were realized in both combustion and post-combustion control technologies for the reduction in pollutant formation and emission. California continued to require more stringent emissions controls then the federal government for (1) automobiles through the Air Resources Board, (2) stationary sources of air pollutant emissions through regional agencies (lead by the South Coast Air Quality Management District). Ever since, California has served as a "living laboratory" for policy and policy implementation related to the challenge of improving the quality of air commeasurate with retaining a robust economy.

In the ensuing years, air quality in the major urban basins of California has improved. However, the reduction in emissions from combustion sources is (1) reaching an asymptote, and (2) being offset by an increase in both the number and operation of combustion sources. Principal examples include the increase in automobiles and the increase in miles driven, the increase in the port activity associated with international trade (ships, trucks, locomotives), and the increase in the demand for electricity. The negative impact of combustion on air quality is one reason that the conflict between energy and environmental quality is at a crossroads. A second is associated with greenhouse gases.

Greenhouse Gases (GHGs).

The first international meeting to acknowledge and proactively address increasing concentrations of GHGs in the atmosphere was held in Rio De Janeiro in 1992. Formally called the "United Nations Conference on Environment and Development" and referred to generally as the "Earth Summit," the 154 nations participating signed the "United Nations Framework Convention on Climate Change (UNFCCC)" with the goal to voluntary reduce atmospheric concentrations of greenhouse gases. Within two years, fifty nations ratified the UNFCCC and, following the terms, entered the instrument into force on March 21, 1994.

Subsequent meetings, beginning in Berlin in 1995, are referred to as the "Conference of the Peoples (COP)." COP 3 was held in Kyoto Japan in 1997 and concluded with the approval of the "Kyoto Accords" which challenged participating countries to curtail carbon dioxide (CO_2) emissions to a

percentage of 1990 levels. The percentage and acceptance of the challenge was left to the individual countries. Examples of countries that adopted the terms and proactively implemented change are Denmark, Sweden, and Germany. The United States, responsible for 25 % of the CO_2 emissions in the world, has yet to accept the Kyoto Accords.

The State of California, however, has adopted into law both the spirit and intent of the Kyoto Accords with a mandated reduction in CO_2 emissions by 2020 to 1990 levels. This translates to a mandatory requirement for the state to reach a 30% reduction over the currently projected emissions by 2020. The state also recognizes that, by 2050, an eighty percent reduction is likely. This initiative, known as AB-32,[1] is following a strict schedule of public input and implementation under a portfolio of regulations designed to meet the letter of the law. As one of the largest economies in the world and a model for meeting environmental challenges in an economically developed authority, the success (or failure) of California over the next decade will profoundly influence the world's ability to addresses the conflict between energy and the environment.

A Remarkable Time in History

The challenge of addressing the conflict between energy and the environment gives rise to a remarkable time in the history of the world that encompasses

-The natural resources of the earth
-The environmental quality of the earth
-The quality and distribution of the water resources of the earth
-The earth's human population and associated quality of life, food, and water

At the turn of the 19th to the 20th century, the automobile was just being introduced, electrical power generation was just being embraced, and the associated industrial revolution was just beginning, all of which would portend a profound impact on society and the economic engine throughout the 20th century. Combustion and fossil fuels were, and are today, the principal drivers for the revolution. Halfway through the 20th Century (in 1943 as noted above), the earth revealed its vulnerability to the pollutants emitted by combustion. Later in the century, attempts to control combustion pollutant emissions were impressive but revealed that the degree of reduction was finite and the increasing utilization of combustion powered automobiles and electric power generators offset these gains. Simply stated, during the 20th century, combustion emerged as the technology upon which society today relies for 80 % of its power, but is also the source of 90 % of the

criteria pollutants emitted in the world, and 94 % of the carbon dioxide emitted into the earth's atmosphere. Adding insult to injury, the combustion process removes oxygen from the atmosphere at the rate of approximately of 400 pounds of oxygen for every tank of gasoline consumed.

The industrial revolution and its ramifications during the 20th century were indeed remarkable, but the environmental impacts of the revolution reveal a crisis of profound proportions. With the transition from the 20th to the 21st century, we are witnessing the kernel of a new revolution (yet to be named although "green-technology" is garnering an early foothold) with the following expectations:

-Concurrent reduction of BOTH criteria pollutant and GHG emissions
-Maintenance and enhancement of a robust economy
-Conservation of natural resources

and, with even greater urgency following the events of September 11, 2001,

-Attaining fuel independence
-Enhancing national security

There is no greater cause around which the earth's peoples and governments must cooperate, and there is no greater question than whether and how this can be accomplished. The COP and California's AB-32 are key steps that may be sufficient. But time is of essence (and some would argue long past) to act proactively and aggressively.

Complicating the challenge is the entanglement between technology solutions per se, and technical solutions that are socially, economically, and politically tolerable. The diagram[*5)] below represents a "web" of interaction that makes the resolution of this conflict so forbidding (and some would argue unlikely). Historically, air pollution episodes (e.g., London and Donora) have forced the corrections needed. The current challenge with criteria pollutants and GHGs is tantamount to a cancer which is slowly eating away at the health of the earth's environment. Once the symptoms reach a crisis stage, the option for corrective action may not be available.

*5 : Samuelsen, G.S. (1971): AIR QUALITY: WHO IS RESPONSIBLE? California Air Environment, October-December .
AIR QUALITY IMPACT ANALYSIS (1979). In "Environmental Impact and Assessment Handbook," 3-1 to 3-165, McGraw-Hill.

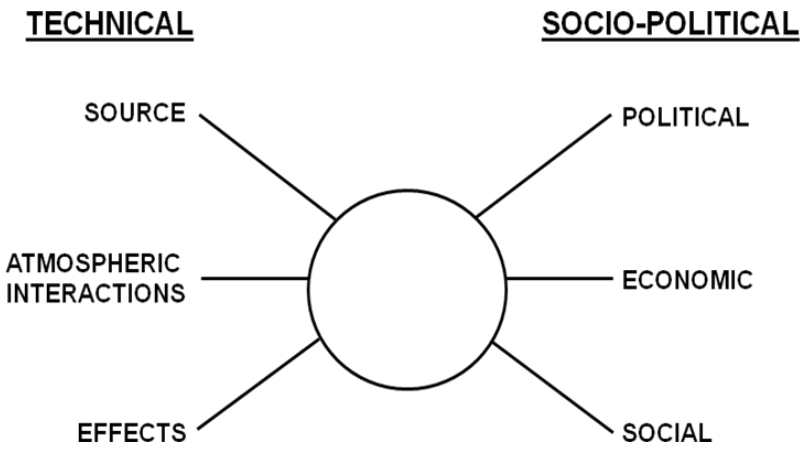

The Direction for the 21st Century

Given this background, a remarkable paradigm shift is occurring in not one, but six major areas of the modern human experience:

1. The automobile fuel.
2. The automobile.
3. The generation of electricity.
4. The utilization of electricity.
5. The mobility in personal transport.
6. The design and operation of buildings.

Any one change would dramatically affect the daily personal experience. In combination, the changes projected are unfathomable. A benchmark is the turn from the 19th to the 20st century. In retrospect, the emergence of automobile and electric power generation and utilization over the 20st century would have been viewed as unfathomable at the time. Technology evolution was driving the change then, unbridled by consideration for environmental impact. For the 21st century, environmental quality is driving the change and driving the requisite technology.

Automobile fuel is transitioning to "dual-fuel," which encompasses a combination of electricity and carbon-free hydrogen. The automobile is transitioning to electric drive power train and a fuel cell power plant. The generation of electricity is transitioning to include (1) distributed generation[*6)] powered by photovoltaic solar, stationary fuel cells, and fuel cell/gas turbine hybrids, (2) central power plants designed for high efficiency,

the production of transportation fuel, zero-emission of criteria pollutants, zero-net water use, and the production of a near-pure stream of CO_2 for capture and storage, and (3) central sources of renewable electricity generated from wind and solar, posing the challenge of intermittency, and requiring storage or other strategies to assure grid stability. The utilization of electricity is transitioning to smart grid technology, smart appliances, and customer control in setting an economic portfolio that will automatically manage electricity demand. Mobility in personal transport is transitioning to include a greater portfolio of options, following and expanding on established models in Japan and Europe. The established models encompass fixed rail transport while the expanding options include shared-use[*7)] vehicle transport, and shared-use/station-car[*8)] transport. The design and operation of buildings is transitioning to highly-efficient designs, abundant use of daylighting, smart sensors and controls, customer managed smart control algorithms, integration of DG, coupling to transport, and distribution and use of direct current (DC) power.

Fortuitously, the environmental and ancillary forces that are driving these transitions are occurring at a time when technology is available or emerging to provide the needed capabilities. These technologies include sensors, controls, microprocessors, advanced robust and secure algorithms, user-friendly interfaces for information, personal control, and the application of personal preferences. Modeling, measurements, and scientific and engineering research are being proactively applied in combination with an increasing population of political leaders who (1) recognize that the conflict must be resolved to assure the health of the earth, society, and the economy; and (2) recognize that the future of economic health will be anchored in the development and application of a wide portfolio of green technologies.

*6 : Distributed Generation (DG): Where electricity is generated at the site of its use, and the heat that would otherwise be vented is captured and utilized for heating and cooling.

*7 : Shared-use: Where one vehicle is shared by a population of customers who reserve the use through a web-based reservation system.

*8 : Shared-use/Station-car: A Shared-use vehicle which is connected to a mass transit commute “station” with a goal to facilitate movement to and from the station.

Closure

The past one hundred years witnessed a remarkable evolution of energy transformation technologies including vehicles from automobiles to rockets, and electrical power generation from wood fired steam boilers to nuclear fission reactors. The principal strategy anchoring this transformation was

the combustion of fossil fuels. In the second half of the 20th century, the earth revealed that its finite resources cannot sustain the continuation of this approach. The most telling challenges are the contamination of the earth's atmosphere with criteria pollutants and greenhouse gases, the copious amounts of water required to generate electricity, the limited supply of fossil fuels, the increasing demand for that limited supply, and the increasing world conflict associated with protecting the supply of fossil fuels. The "wake-up" call, the recognition and acceptance of the conflict between energy and the environment, has taken fifty years to mature, and we enter the second decade of the 21st century with an intriguing parallel to one hundred years ago. Place yourself in 1910 and project the remarkable "explosion" of combustion based technology that evolved throughout the 20th century. Then place yourself in 2010 and project the "explosion" of the transformative changes in the personal experience in 21st century. Remarkable indeed.

Guest Forum

Pragmatic Efficiency Limits for Internal Combustion Engines

Prof. David E. Foster
University of Wisconsin-Madison
Phil and Jean Myers Professor
Ph. D.

This article gives an overview of the thermodynamic principles demonstrating that the maximum efficiency theoretically possible with a hydrocarbon fueled internal combustion engine is one hundred percent. From this basis the focus turns to articulating irreversibilities that naturally occur within the processes of converting the chemical energy in the fuel into shaft work. These losses are classified as losses that cannot be eliminated when using the current embodiment of internal combustion engines, and losses that in principle could be reduced through application of advanced technologies. Because power is obtained from the engine via unrestrained chemical reaction, i.e. combustion, we must accept a loss of work potential of between 20 and 25 percent of the fuel's energy. Other losses, such as friction, heat loss and exhaust energy account for the balance of the useable energy that is not converted directly into shaft work. The interplay between combustion temperature, the ratio of specific heats of the combustion chamber gases, heat transfer and exhaust availability is presented as support for a postulate that the maximum pragmatic efficiency is most readily achieved through efforts to keep combustion temperatures low, which in turn maximizes the direct conversion of the fuel's chemical energy into shaft work while minimizing the available energy lost to heat transfer and exhaust flow.

炭化水素を燃料とする内燃機関において，理論上実現可能な最大効率が100%であることを裏付ける熱力学の原理について概説する。次に，それに基づき，燃料のもつ化学エネルギーを軸仕事に変換するプロセスにおいて，必然的に発生する不可逆性について明らかにする。このようなエネルギー損失は，現在の内燃機関の構造を用いる限り避けられないものと，原理的には先進技術の応用により低減の可能性があるものとに分類できる。内燃機関の出力が制御不可能な化学反応，すなわち燃焼によって得られるという性質上，燃料エネルギーの20%から25%にあたる潜在的仕事量の損失は避けられない。摩擦や熱損失，排気エネルギーなどその他の損失は，直接軸仕事には変換されないものの，利用可能なエネルギーの一部である。最大のエネルギー効率を得るには低い燃焼温度を維持するのが最も容易，という仮説を立証するため，燃焼温度，燃焼室内のガスの比熱比，熱伝達，排気の利用可能性の相互関係について示す。低温燃焼においては，燃料の化学エネルギーが直接軸仕事に変換される量が最大になると同時に，利用可能なエネルギーのうち熱伝達や排気の形で失われる分が最小になる。

Introduction

Internal combustion engines using liquid hydrocarbon fuels are an extremely effective combination of energy converter and energy carrier for mobility applications. The high energy density and specific energy of liquid hydrocarbons are well matched for applications in which the fuel must be carried onboard the vehicle; and the engine is a convenient and effective device for converting the stored energy in the fuel into mobile power. Together the IC Engine and HC fuel are a robust and economically viable power propulsion system and will remain so for

decades to come[1]

However, the principle source of fuel-petroleum, is a limited resource which is in high demand and with the global development currently underway the demand is likely to increase. Furthermore the impact of carbon emissions from our mobility systems is a concern relative to its impact on the global climate. Consequently, it is of utmost importance that our mobility systems achieve the maximum possible efficiency with minimal environmental impact, while still preserving utility to the user. In the author's opinion this is one of the grand challenges facing the propulsion technical community today.

Two reasonable questions arise when considering the powertrains of our propulsion systems. What is the maximum efficiency that is theoretically possible and how does the efficiency of our current powertrains compare to this maximum? And, what are practical limits to the efficiency when pragmatic engineering constraints are imposed on to the system? This latter question is very important in that it yields realistic stretch targets to which we direct our development efforts, and it allows us to identify the important phenomena that should be addressed to make our mobility systems consume less fuel, emit little to no emissions and still provide the desired utility.

The purpose of this article is to identifying the pragmatic limits of engine efficiency achievable using engine embodiments likely to be present for the next several decades, namely a piston cylinder configuration in which the high pressure and temperature gases from combustion are expanded to extract work. To do this I will first review the maximum theoretical efficiency for an internal combustion engine and then identify the losses which occur in a typical engine. From this perspective I will then offer discussion as to which losses are unavoidable and comment on how other losses can be minimized within the scope of practical technologies.

Maximum Possible Work

One of the most important concepts to realize when asking what is the maximum possible work that can be obtained from an internal combustion engine is that the engine we use in our propulsion systems is not a thermodynamic cycle. It is a chemical process. In a thermodynamic cycle the working fluid undergoes a cycle. This does not happen in an internal combustion engine. The air fuel mixture is brought into the engine, allowed to react to products, expanded, and then is exhausted. The next engine cycle uses a different air fuel mixture, that is, the working fluid is thrown away and not brought back to its initial condition. Consequently, using classic thermodynamic heat-engine cycle analysis is not appropriate to answer the question we are addressing in this paper.

A thermodynamic analysis addressing the maximum useful work that can be obtained from a chemical process, such as the combustion process in an internal combustion engine, shows that the maximum useful work obtainable is the negative of the change in Gibbs Free energy of the chemical reaction[2]:

$$W_{\max,\,\text{useful}} = -(\Delta G)_{T_0,\,P_0}$$

It is worth noting here that this is also the equation for the maximum theoretical useful work that can be obtained from a fuel cell. When describing a fuel cell it is usual to write:

$$(\Delta G)_{\text{rxn}} = -nFE$$

where:
n = number of moles of electrons transferred
F = Faraday's constant
E = Electrical potential difference

When the change in Gibbs Free energy is written in terms of the electrochemical potentials the above equation is called the Nernst Equation[3].

It is instructive to conceptualize what an engine would look like if it could be made to achieve this ideal result. Figure 1 is such a conceptualization. The embodiment of the ideal engine shown in Figure 1 appears to be similar to what is actually in development today. However, there are distinct pedagogical differences. In the conceptualization shown in Figure 1, it is assumed that everything is reversible in the engine. Namely the air and fuel enter the engine at atmospheric temperature and pressure, undergo reversible processes throughout the engine, including the chemical reaction, and then leave the engine as equilibrium products at atmospheric conditions. These reversible processes will dictate specific state histories so it may be necessary to invoke a heat transfer to get the products to atmospheric temperature. As depicted in the figure, any such heat transfer would be done through a reversible heat-engine which has its heat rejection at atmospheric conditions. The work obtained from this reversible heat-engine is then added to the work output of the engine shaft to give the maximum possible work.

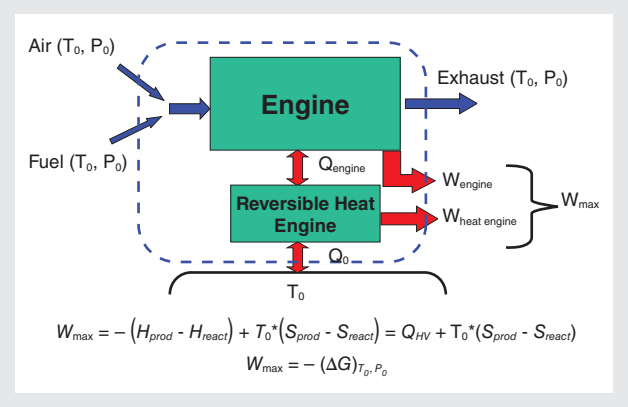

Figure 1 Conceptualization of an Engine to Achieve the Maximum Possible Work from a Charge of Air and Fuel Reacting to Products

Shown on the bottom of Figure 1 is the energy balance for determining the work from this reversible engine. It is worth noting that the maximum work theoretically obtainable is equal to the heating value of the fuel, Q_{HV}, adjusted by the unusable heat which is rejected at atmospheric temperature, $T_0*(S_{prod} - S_{react})$. The combination of these two terms is equal to the negative of the change in the Gibbs Free energy of the chemical reaction.

The Relationship between the Fuels Heating Value and Gibbs Free Energy

One interesting subtlety of this result is the realization that the maximum theoretical work obtainable from an internal combustion engine, or fuel cell, is given by the change in Gibbs Free energy as opposed to the fuel's Heating Value. A table comparing the Heating Value and the negative of the Gibbs Free energy for several fuels when oxidized with air at atmospheric conditions is shown below.

Table 1 Enthalpies and Free Energy Changes of Several Fuels when reacted with air at atmospheric conditions (adapted from Heywood[2])

Fuel	Heating Value (MJ/kmol)	- Gibbs Free Energy (MJ/kmol)
Methane	802.3	800.6
Methanol	638.59	685.35
Propane	2044.0	2074.1
Octane	5074.6	5219.9

Two observations are apparent in examining the values given in Table 1. First the heating values and changes in Gibbs Free energy of reactions for typical hydrocarbon fuels are very close to the same value. That is the maximum theoretical efficiency of an internal combustion engine is effectively one hundred percent. The second observation is that some of the changes in Gibbs Free energy are larger than the Heating Value. This indicates that theoretically it is possible to extract more work from the engine than the heating value of the fuel, which is typically referred to as the energy input. This circumstance is a result of expansion of the products of combustion all the way to atmospheric pressure as part of maximizing the work output. In some cases, this expansion to atmospheric pressure would result in a temperature below atmospheric, which means that the heat transfer between the engine and the environment is from the environment to the engine. Thus work is obtained from the auxiliary heat-engine through a heat transfer from the environment into the engine to bring the engine back up to the atmospheric temperature.

Identifying Irreversibilities within the Engine

There are two underlying precepts in understanding the maximum theoretical work that could be obtained from an internal combustion engine. The first is that all processes are conceptualized to be reversible, that is, there are no losses. This means that all of the energy within the fuel that could have been converted into useful work, actually is converted into useful work. This recognizes the second precept underlying the development, namely that energy has quality, called exergy or availability, and that irreversible processes degrade useable energy into unusable energy; namely exergy or availability can be destroyed. Evaluating the availability destruction that occurs in the processes of a real engine is an instructive exercise for quantifying losses relative to the ideal engine described above. Furthermore it is possible to assess whether technological development can make inroads into reducing those losses and thus improve the efficiency of the engine. An analysis of the losses is brought about by performing an availability, or exergy, balance. Such a balance is shown in Figure 2.

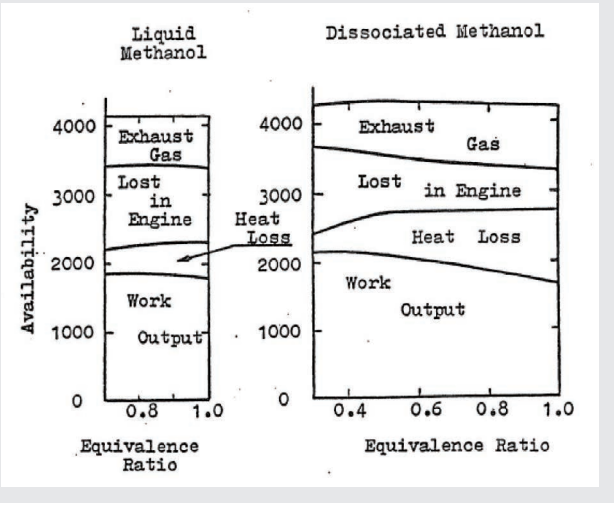

Figure 2 Availability Accounting per Mass of Fuel for Engine Operation for Different Equivalence Ratios for Methanol and Dissociated Methanol[4]. The units of the availability are kcal/liter of Methanol.

From the discussion above recall that for an internal combustion engine, the usable energy in the fuel is equal to the change in the Gibbs Free energy between the reactants and the products. The graphs given in Figure 2 are displayed in terms of availability, and are plotted on a kcal per liter of methanol basis, in recognition that in a real engine, some of the Gibbs Free energy is degraded into non useable forms, i.e. an availability destruction or "loss". The energy is conserved but its usability has been degraded.

Figure 2 is the equivalent of a stack chart of what happens to the useable energy for each operating condition. The work output represents energy leaving the engine as shaft work, the desired outcome for the engine. The heat loss represents useable energy that left the engine as a heat transfer as opposed to shaft work. The term "lost in engine" is a measure of the irreversibilities of the combustion process itself. It is not an inefficiency of combustion. It is a degradation of useable energy because of the unconstrained chemical reactions taking place within the combustion chamber, even though the combustion has gone to completion. Finally, the exhaust gas availability is the useable energy leaving the engine in the exhaust. Realize, the available energy contained within the heat transfer and exhaust gases leaving the engine represent that portion of the energy in the heat transfer and exhaust flow that is useable, as opposed to the amount of energy within those respective energy flows.

Several interesting observations can be made from Figure 2. First, there is a significant irreversibility associated with the combustion process and this loss gets bigger when the engine is operated under lean conditions. This loss represents approximately 20 percent of the fuel's useable energy. Second, there are significant available energy flows leaving the engine in the forms of heat transfer and exhaust flow. And finally, the work out of the engine per unit mass of fuel increases for lean mixtures, even though the irreversibilities of combustion increase. This is so because the available energy thrown away in the exhaust and with the heat transfer decreases as the engine is operated with progressively lean air-fuel ratios. These decreases more than compensate for the increased losses that occur within the lean combustion.

Detailed Analysis of the Individual Losses

A more detailed assessment of the individual losses is insightful as to where potential for improving the efficiency of real engines lie. As a prelude to this discussion I point out that the analysis of the losses presented in Figure 2 did not include engine friction. Indeed, reduction in engine friction is an important component of improving efficiency. Friction represents work that was leaving the engine as shaft work but got diverted. Any reduction in friction manifests itself immediately as a one-to-one increase in shaft work. The discussion here is focused on the thermodynamic phenomena associated with the losses.

Availability Destruction from Combustion

A loss for approximately 20 percent of the fuel's useable energy in combustion is discouraging and would seem to represent an opportunity for improvement. This has been the subject of much discussion and analysis[5, 6, 7, 8]. However, the combustion irreversibility is a result of allowing the gradient between chemical potentials of the reactants and products, the affinity, to relax unconstrained. Thermodynamics teaches us that when any large gradient is allowed to relax unconstrained there will be large losses, viz. heat transfer across a large temperature gradient, or the irreversibilities associated with fluid flow associated with a large pressure gradient. Even if it were possible to extract work from the cylinder at the same rate at which the chemical reaction were occurring-constant temperature combustion, the irreversibilities of combustion would not be reduced[9]. The only way to reduce the irreversibilities of combustion is to raise the temperature at which the chemical reactions occur. This is why the losses of combustion increase with lean operation, the combustion temperatures are lower. Within the practical combustion temperatures for internal combustion engines the irreversibilities of combustion

will range from 20 to 25 percent[9].

Consequently using unconstrained chemical reactions as part of the process of converting the chemical energy of the fuel into work means we will have to accept a loss of approximately 20 to 25 percent of the work potential of the fuel. We will not be able to engineer our way around this. It is worth noting that this same analysis is also true for fuel cells.

The paradox of increased combustion irreversibilities and increased work output per unit mass of fuel with lean combustion is resolved through a more detailed assessment of the availability transfers occurring during the expansion process, which impacts the availability leaving the engine in the exhaust gas and as heat transfer.

Work Extraction via Cylinder Gas Expansion and Useable Exhaust Energy

The work obtained from the gases being expanded within the cylinder is given by the expression:

$w = \int P dv$

The pressure and the volume are related via the expression:

Pv^{γ}

where:
w = work per unit mass
P = cylinder pressure
v = Specific volume of the gases in the cylinder
γ = ratio of specific heats

The ratio of specific heats, which is a function of gas composition and temperature, plays an important role in determining the work output from the engine.

Figure 3 is a simple plot showing the effect of composition and temperature on the ratio of specific heats, γ, and the impact of the value of γ on the engine efficiency. One can see from Figure 3 that as the temperature increases, γ decreases. It is also apparent that at a given temperature γ is lower for a mixture of combustion products than it is for air, and similarly a mixture of air and fuel. The right hand plot shows the efficiency of an engine at different compression ratios for different values of γ. For ease of presentation the calculation of the efficiency shown here was done using a simplified ideal gas analysis. From the two graphs in Figure 3 it is evident that if γ is larger there is more work extraction per unit of volume expansion in the engine. Furthermore it is apparent that small changes in γ can have measurable impact on the efficiency.

Herein lies one of the reasons for the higher efficiency of lean burn engines. Lean burn engines have lower combustion temperatures than stoichiometric engines.

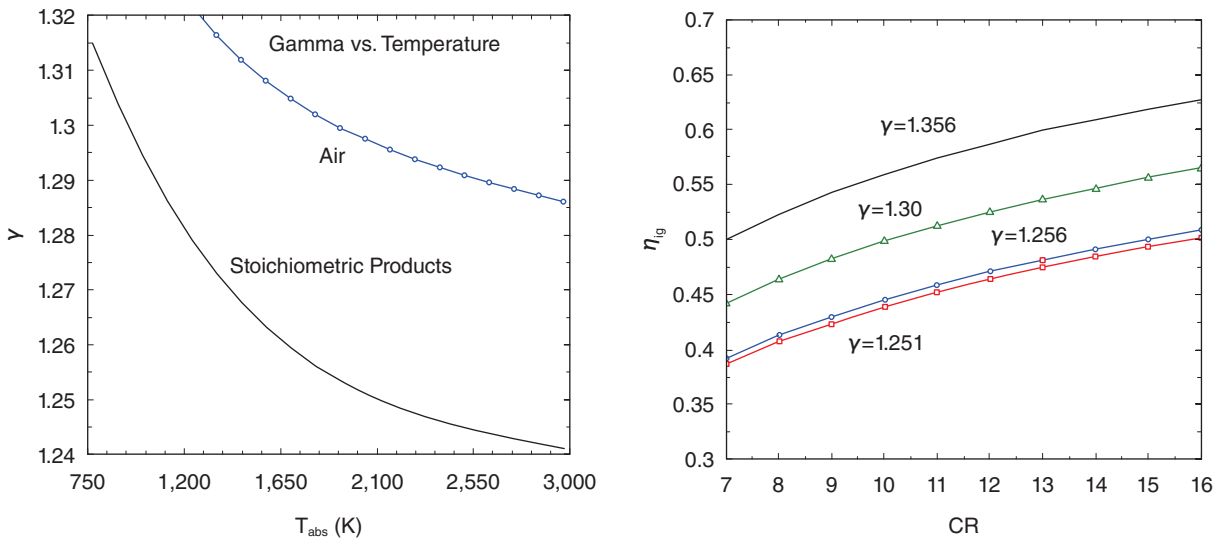

Figure 3 The Effect of Mixture Composition and Temperature on, and the Effect of γ on the Efficiency of an Internal Combustion Engine-Plotted vs. Compression Ratio (CR)

Even though there is a decrease in γ because of the composition change and the increase in temperature from combustion, the lower temperature of the lean combustion results in a γ that is larger than that for the stoichiometric combustion products. The larger relative γ of lean combustion results in a larger work extraction per increment of volume expansion than occurs with stoichiometric combustion products. Because of this there is less useable energy thrown away in the exhaust for lean combustion. This is what is shown in the availability balance given in Figure 2.

Useable Energy in the Heat Transfer

The available energy in heat transfer depends on the temperature at which the heat transfer takes place. Heat transfer occurring at higher temperatures has the ability to do more useful work than lower temperature heat transfer.

Figure 4 shows the portion of the heat transfer that could theoretically be converted to work as a function of the temperature at which the heat transfer takes place. The range of temperatures shown in the Figure was chosen to represent temperatures that might typically be experienced during combustion.

As shown in the Figure, as the temperature at which the heat transfer takes place increases a larger portion of the heat transfer energy has the capacity to be converted into work. The two illustration lines on the Figure show the portion of the heat transfer energy that could be converted into useful work for heat transfer occurring at temperatures of 2600 K and 1900 K respectively. These temperatures could be considered representative of those occurring during stoichiometric and lean combustion. It

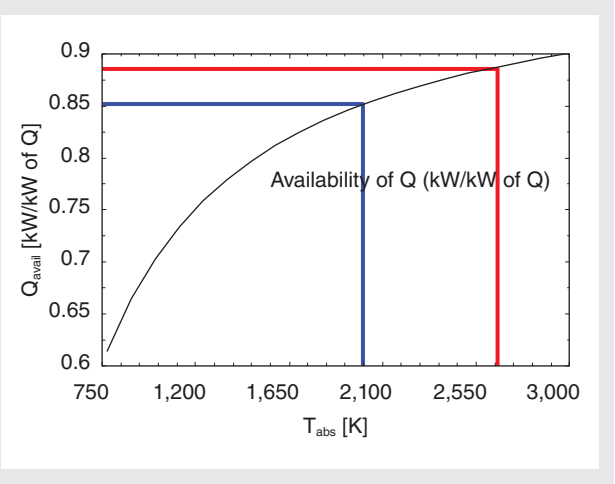

Figure 4 Proportion of the Heat Transfer that Could be Converted into Useful Work vs. Temperature at which the Heat Transfer Takes Place.

is noted that each unit of energy lost as heat transfer at 2600 K has approximately a 3 percent larger proportion that could be converted into useful work than a similar quantity of heat transfer at 1900 K. That is each unit of energy lost to heat transfer at 2600 K represents a 3 percent greater loss of work potential than the same quantity of heat transfer lost at 1900 K.

There is an added subtlety to this analysis. The rate of heat transfer is proportional to the temperature difference driving it. The lower in-cylinder temperatures associated with lean or low temperature combustion results in a lower driving potential for heat transfer. So, with lower in-cylinder temperatures both the quantity of the heat transfer and the work potential of each unit of energy lost is reduced.

Summary

Through the discussion presented in this article it has been shown that for purposes of assessing the maximum theoretical efficiency of an internal combustion engine running on hydrocarbon fuels, one can essentially consider all of the energy in the fuel to be available to do work. That is the maximum theoretical efficiency of an internal combustion engine is 100 percent.

However, because we use an unconstrained chemical reaction as part of the energy conversion process approximately 20 to 25 percent of the fuels available energy is destroyed. As long as unrestrained chemical reaction is used in our propulsion systems with current combustion temperature ranges, this loss is unavoidable.

Reducing the loss of work potential associated with heat transfer and exhaust gas leaving the engines is tenable. To this end, efforts which minimize the reduction in γ from combustion help to maximize the work extraction per unit of volume expansion, which increases efficiency and results in less usable energy being thrown away in the exhaust. Minimizing the reduction in γ can be achieved by keeping in-cylinder combustion temperatures as low as possible, even though this results in slightly larger combustion irreversibilities.

In addition lower in-cylinder temperatures also have a beneficial effect on heat transfer losses. Not only does the magnitude of heat loss decrease with lower in-cylinder temperatures, but the proportion of that energy that has the capacity to be converted into work is also reduced.

It is interesting to observe that much of the work taking place within engine combustion development laboratories

is directed at reducing in-cylinder temperatures. Many approaches are being pursued, which can be described generically as low temperature combustion (LTC). The original motivation for activities in LTC was to minimize emissions of nitrogen oxides and particulates. However a side benefit is emerging. Successful control of low temperature combustion processes is also yielding benefits of improved efficiency.

Finally, one is tempted to opine as to whether there is a maximum pragmatic efficiency that can be achieved with the internal combustion engine. We must accept a loss of approximately 20 to 25 percent because of combustion, so an upper limit to the maximum pragmatic efficiency becomes 75 to 80 percent. From this basis, the question becomes how effective can we manage the thermal energy and exhaust energy flows from the engine. It is unlikely that these losses can ever be completely eliminated, however good progress is being made at reducing the losses associated with these energy flows. Engine efficiencies in excess of 50 percent have been achieved in very large slow RPM diesel engines. The Future Truck Program of the US DOE is supporting programs to demonstrate 50 percent brake thermal efficiency in heavy duty truck engines, along with identification of technical pathways to achieve 55 percent efficiency. And, a recent DOE workshop suggested that a stretch goal of approximately 60 percent might be an ultimate pragmatic limit[8].

References

[1] Real Prospects for Energy Efficiency in the United States, report by the National Academy of Sciences, Washington, D.C., 2009.
[2] Heywood, J.B., Internal Combustion Engine Fundamentals, McGraw Hill, Inc., 1988, ISBN 0-07-028637-X
[3] O'Hayre, R.P, Cha, S-W, Colella, W.G, Prinz, F.B., Fuel Cell Fundamentals, John Wiley and Sons, Inc. 2009, ISBN978-0-470-25843-9
[4] Edo, T., and Foster, D.E., VI International Symposium on Alcohol Fuels Technology, Ottawa Canada, 1984
[5] C.D. Rakopoulos and E.G. Giakoumis, "Second-law analysis applied to internal combustion engine operation," Progress in Energy and Combustion Science, 32, 2-47 (2006).
[6] N. Lior and G.J. Rudy, "Second-Law Analysis of an Ideal Otto Cycle," Energy Conversion and Management, 28(4), 327-334 (1988).
[7] R.J. Primus, K.L. Hoag, P.F. Flynn, and M.C. Brands, Appraisal of Advanced Engine Concepts Using Second Law Analysis Techniques, SAE 840032
[8] C.S. Daw, R.L. Graves, R.M. Wagner, and J.A. Caton, Report on the Transportation Combustion Engine Efficiency Colloquium Held at USCAR, March 3-4, 2010, ORNL/TM-2010/265
[9] Druecke, B.C., Foster, D.E., Klein S.A., Daw, C.S., Chakravarthy, V.K., and Graves, Second Law Analysis of Constant Temperature Combustion", Central States Section Combustion Institute, Chicago, IL, March 2006, also MSME University of Wisconsin-Madison 2006

Guest Forum

Water Vapor Delivery for Thin Film Vacuum Processes

Said Boumsellek
Implant Sciences Corp.,
San Diego, California, USA
Ph. D.

Jeffrey Spiegelman
RASIRC, San Diego,
California, USA

Water vapor is known to play a significant role during thin film deposition in ALD, MOCVD, and sputtering processes. Such processes are commonly used to generate transparent conductive layers (TCO) and modify crystal structures via grain size or defect repair. The ability to supply water vapor free from atmospheric contaminants is critical to film integrity. A novel method for control and delivery of water vapor using ionic fluoro-polymer membranes has been tested and results are presented in this paper. One side of the membrane was exposed to ambient air and then de-ionized (DI) water. The other side of the membrane was exposed to high vacuum where a miniature mass spectrometric Residual Gas Analyzer (RGA) was used to monitor pressures of individual gas species. When the membrane was exposed to air the water-to-nitrogen ratio was 10:1 by volume. When the outer surface of membrane was submerged in water the ratio increased to 200:1. Separately on a humidity test stand and under a 20 sccm purge flow of dry nitrogen, 2.8×10^{-3} sccm of water was added, raising the concentration of water to 1400 ppm from less than 1 ppm.

ALD法, MOCVD法, およびスパッタ法による薄膜形成過程において, 水蒸気が重要な役割を果たすことが知られている。これらの薄膜形成法は, 透明導電膜(TCO)の形成や粒度・欠損の修復による結晶構造転位の目的で一般的に使用されている。高品質の薄膜を形成するためには, 大気由来の不純物を含まない水蒸気を供給することが重要である。本稿では, イオン透過性フッ素樹脂膜を用いて, 水蒸気を制御・供給する新しい手法についてその試験結果を報告する。イオン透過性フッ素樹脂膜の一方の側は, 最初は大気に, 続いて脱イオン(DI)水に接触させた。もう一方の側は高真空状態とし, 小型の質量分析法残留ガスアナライザ(RGA)により各ガス種の分圧を測定した。膜が大気に曝されていたときの水蒸気と窒素の体積比は10:1であった。膜の外側表面を水に曝すと, 水蒸気の比率は200:1まで増加した。これとは別に, 湿度試験装置上にて, 流量20 sccmの乾燥窒素によるパージ流に2.8×10^{-3} sccmの水を添加したところ, 水分濃度は1 ppm未満から1400 ppmまで上昇した。

INTRODUCTION

Water vapor is critical to ZnO deposition[1] and insertion of TiO layers under ZnO during sputtering[2]. Water vapor reduces optical losses at the TCO interface in indium-tin-oxide (ITO) devices[3]. CIGSe solar cells grown with water vapor using MBE were found to have efficiencies of 18.1% as water was responsible for the decrease in donor defect density[4]. Many ALD films use water as the oxygen source. The use of water as a precursor has economic and safety benefits compared to other oxide sources. However the controlled delivery of pure water vapor is challenging.

Direct flow control of the water needed in such applications is difficult due to the expansion of 1 gram of water to 1,244 cc of gas at room temperature and atmospheric pressure. Volume flows needed in sputtering applications are often less than 0.1 sccm. In its vapor phase water typically condenses unless it is added to a carrier gas stream. This requires the use of water bubblers, which add water vapor based on the partial pressure of the water relative to that of the carrier gas. Bubblers have problems with contamination and bacterial growth, as well as variability with temperature, pressure and fill level. Microdroplet entrainment can also increase variability in the delivered water. The DI water in the bubbler must be degassed before use in order to remove residual oxygen and nitrogen in the water. Most problematic is that the bubbler cannot be directly exposed to the vacuum environment as violent boiling can occur. Furthermore water droplets varying with the vacuum level are carried into the process chamber making the actual volume of water delivered neither controlled nor repeatable.

In this paper we present the performance results of a new technique developed by RASIRC in collaboration with Implant Sciences. The method consists of using a membrane for the control and delivery of water vapor into vacuum processes. Due to differences in permeation rates the membrane process selectively allows water into a gas or a vacuum process at the detriment of other components. Needing only house DI water and power, it can humidify inert gases, as well as oxygen, hydrogen, and corrosive gases at atmospheric or vacuum process pressures. The membrane is now part of the RainMaker Humidification System (RHS), which adds controlled amounts of water vapor to any carrier gas.

Membrane processes can be thought of as simple separation techniques which employ the membrane as partitioning phase. In the process, a driving force, usually pressure or concentration, is applied to one side of the membrane and the selective component(s) preferentially pass to the other side as the permeate. The permeation can be described by Fick's Law. The non-porous ionic perfluoropolymer membrane (Figure 1) excludes particles, micro-droplets, volatile gases, and other opposite charged species from being transferred to the carrier gas and ensures only water vapor is added. The membrane is highly selective, preventing most carrier gases from crossing over into the source. This allows the safe use of gases that should be constrained from mixing

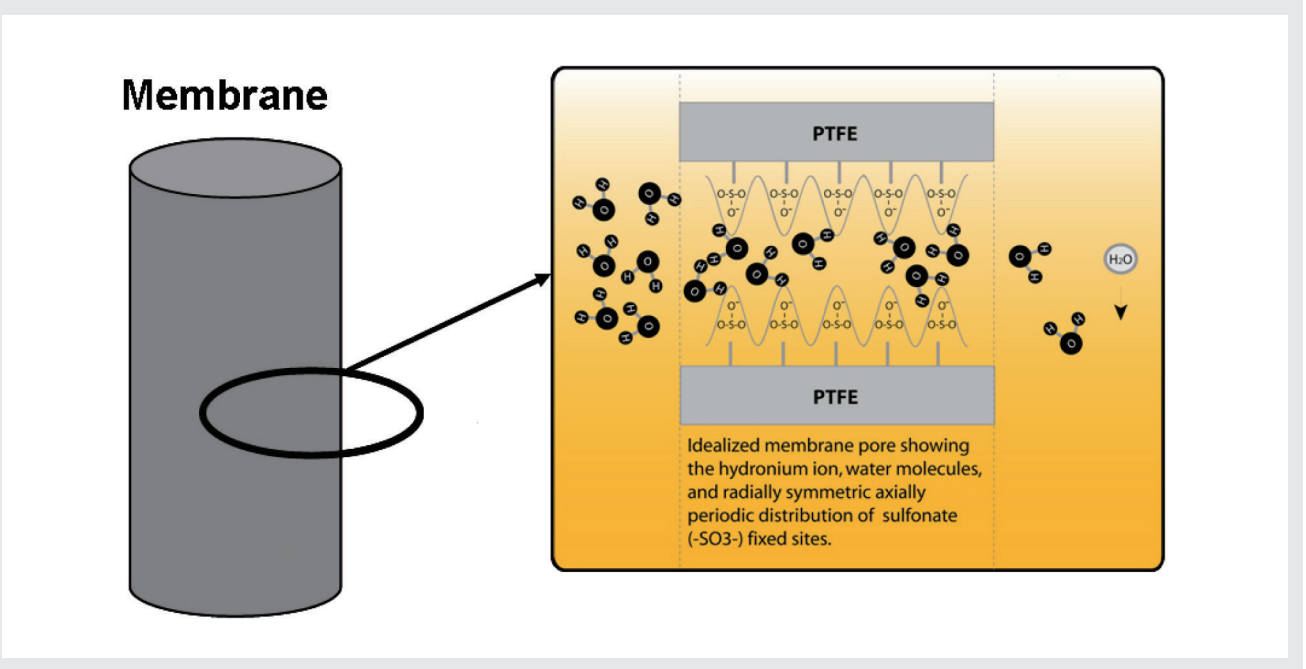

Figure 1 Non-porous ionic membrane is selective for water vapor

with liquid water. Other contaminants in the liquid source cannot permeate across the membrane or enter the carrier gas stream, resulting in a saturated product that is consistent and pure. The membrane allows the rapid transfer of water vapor into carrier gas such as nitrogen, compressed clean dry air, forced ventilation air, helium, oxygen or hydrogen.

MICRODROPLET CONTROL

Microdroplets lead to entrainment of ion contamination and particulates. Furthermore cold spots occur where microdroplets land leading to non-uniformity and warpage. In order for oxide films to work properly, the film thickness and uniformity are critical. The membrane process solves many of the challenges for direct delivery of water vapor by completely changing the way water molecules make the transition from liquid to gas phase. Where bubblers and vaporizers depend on water molecules overcoming the surface tension and water molecule binding energies, the RASIRC products are based on a hydrophilic membrane that uses the ion charge of the membrane to separate each water droplet into its molecular components. The energy required to enter the membrane is equal to the heat of vaporization. Transfer across the membrane is restricted to single and small channel transfer rates. Once molecules cross the wall of the membrane, they are energized and ready to enter the gas phase based solely on the vapor pressure curve that relates to the temperature of the water. Using the membrane as the phase separator prevents water droplets from permeating the membrane and ensures very smooth and consistent flow.

EXPERIMENTAL

Four ionic perfluoropolymer membrane assemblies were fabricated (Figure 2); one blank and three devices under test (DUT). Each assembly consists of a 3" long 1/8" O.D. stainless steel (SS) tubing terminated at both ends with 1/4" VCR fittings. The 1/8" O.D. SS tube of the DUT units features two diametrically opposed 0.04" diameter holes drilled through the tube. The entire length of tube was then sleeved with 0.005" I.D. tubular membrane.

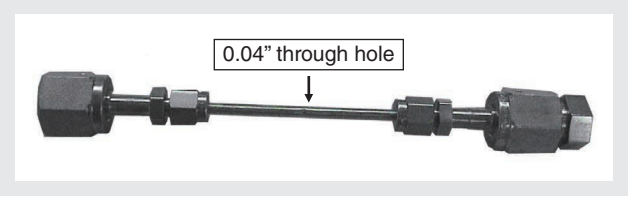

Figure 2 Membrane assembly (DUT)

A Teflon sleeve (not shown on Figure 2) was machined to snap over the hole to allow water drops to be added directly in a controlled manner.

These assemblies were first leak tested using a mass spectrometer leak detector and then mounted onto the vacuum test station. A miniature 100 amu mass spectrometric residual gas analyzer (RGA)[5] manufactured by Horiba, was used to perform permeation analysis (Figure 3). The Horiba device is a high pressure RGA with an dynamic range extending from ultra high vacuum up to 11 mTorr. It is therefore capable of withstanding large pressure excursions anticipated in this project.

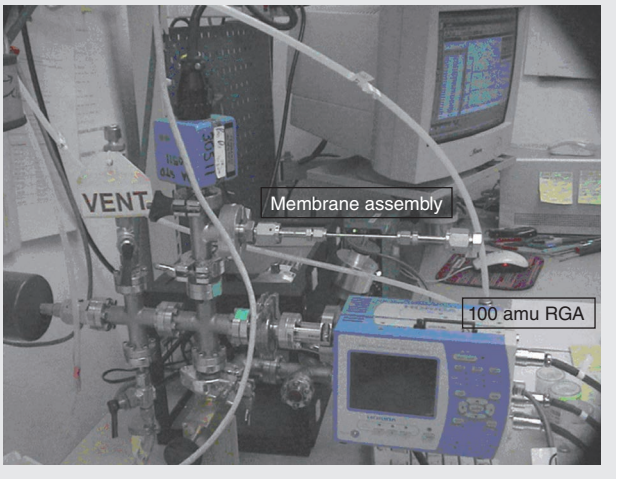

Figure 3 RGA test setup

The testing procedure consists of:

1. Acquiring a baseline spectrum using the blank membrane assembly unit
2. Acquiring a baseline spectra using each of the three DUTs
3. Assembling Teflon sleeves on the three DUTs
4. Acquiring spectra with the three DUTs "immersed" in water
5. Testing for water permeation rate under internal nitrogen purge

RESULTS AND DISCUSSION

The Helium leak test results for all four assemblies are shown on table below:

Table 1 Helium Leak Test results

Assembly	Leak Rate (sccs)
Blank Unit	$< 10^{-9}$
DUT #1	1.2×10^{-8}
DUT #2	2×10^{-8}
DUT #3	5×10^{-9}

These results show negligible leak rates compared to the anticipated permeation under water conditions rates. The assemblies were then mounted on the RGA vacuum test stand one after the other to ensure repeatable performance.

The results showed stable background with a 10:1 water to nitrogen rate and 25:1 water to oxygen rate when exposed to air with 50% relative humidity. The Teflon water trap was added to allow for local application of water. When the droplet was added away from the orifice in the tube, the diffusion increase was slight. However, when directly aligned with the orifice, the gas diffusion rates increased significantly. The water vapor pressure increased 20 times while oxygen increased 10 times and nitrogen pressure increased by 60%. There was a significant swing in oxygen pressure exceeding nitrogen pressure when water was added to the membrane. The results were repeatable (see Figure 4).

Figure 5 show superimposed mass spectra of dry versus wet. Upon submerging the membrane in water the total pressure increased from high 10^{-6} to about 2×10^{-3} Torr. Such a pressure excursion is mostly accounted for by the surge of the partial pressure of water. Given the pumping speed inside the vacuum chamber the water permeation rate through the 0.04" diameter hole at 22 °C is calculated to be 0.29 sccm.

The Nafion membrane permeation rate is therefore calculated to be 142 sccm/in^2. Higher water enrichment factors can be obtained at higher water temperatures as can be seen on Figure 6.

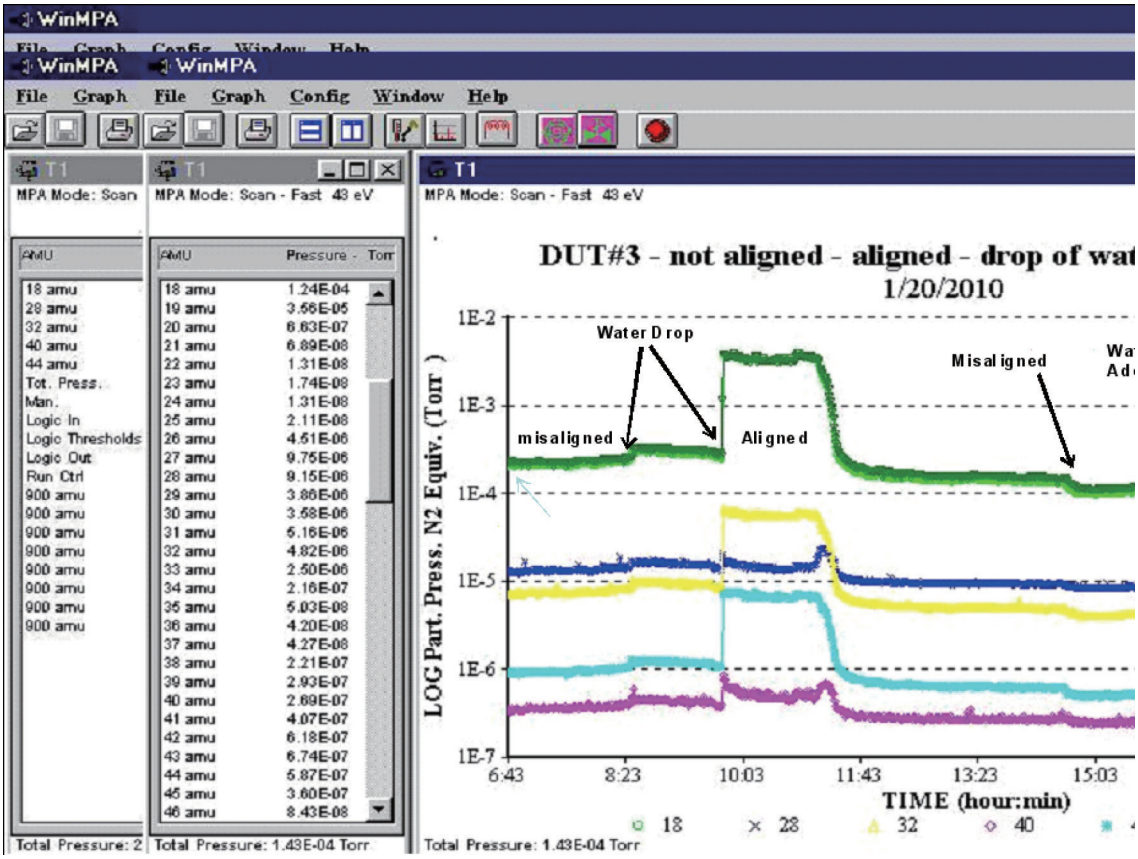

Figure 4 Screen shot of RGA of DUT #3 over time sequence. The diffusion through the membrane increased with water. Nitrogen diffusion rate was not significantly influenced while oxygen increased 10 fold.

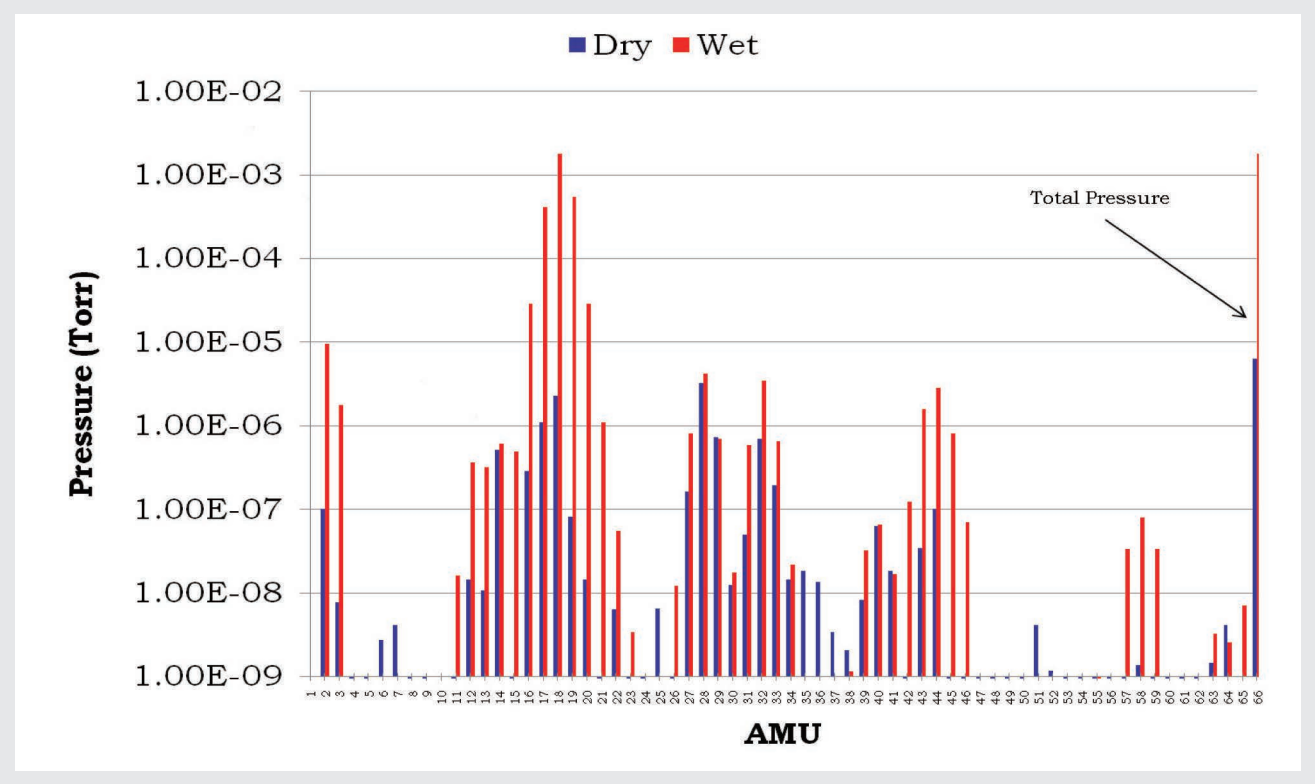

Figure 5 Histogram of mass peaks of dry versus wet performance

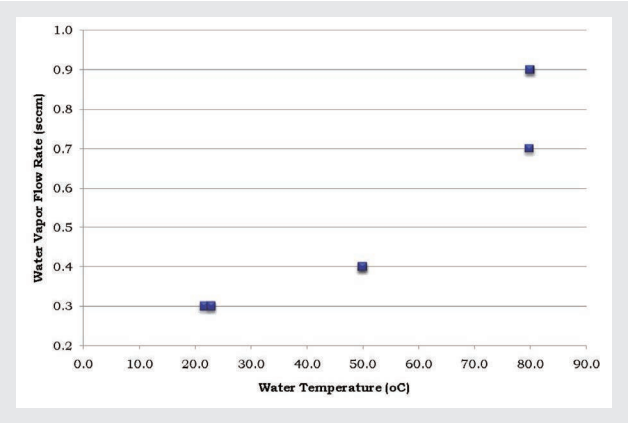

Figure 6 Water permeation rate versus temperature

Following the RGA testing, water permeation was measured using a Vasalia humidity probe. For comparison purposes DUT#3 was used. 20 sccm of dry nitrogen was run through the device as set by a 100 sccm Unit Instruments mass flow controller. The humidity was recorded downstream. The water ppm value was 272 ppm in air at 20 sccm and 2045 ppm in water. Relative permeation rates are shown on table 2 below.

Table 2 Results of relative permeation tests

Relative Permeation		
Species	Dry	Wet
H_2O	24	684
N_2	1.6	1.1
O_2	2.1	4
H_2O/N_2	10	430
H_2O/O_2	34	522

While the permeation ratios are qualitatively similar to the ones obtained with the RGA more accurate control of the surface area of the membrane exposed to water is needed for quantitative comparisons.

SUMMARY AND CONCLUSION

An ionic perfluoropolymer membrane was tested under vacuum conditions to determine if it could selectively allow water vapor to diffuse into the vacuum process. The results indicated that in ambient air, water could be added in a 10:1 ratio relative to nitrogen and 200:1 when immersed in water. The ability to add ppm levels of water make the membrane ideal as a water source for MBE processing of CIGSe films and for sputtering applications including ITO, TiO, and ZnO.

References

[1] S. Fay et al., “Rough ZnO Layers by LP-CVD Process and the Effect in Improving Performances of Amorphous and Microsrystalline Silicon Solar Cells”, Institut de Microtechnique (IMT), Rue A.-L. Breguet 2, 2000 Neuchâtel, Switzerland.

[2] P. Buehlmann et al., “Anti-Reflection Layer at the TCO/Si Interface for High Efficiency Thin-Film Solar Cells Deposited on Rough LP-CVD Front ZnO”, Twentysecond European Photovoltaic Solar Energy Conference, Milan, 2007.

[3] T. Koida et al., “Structural and Electrical Properties of Hydrogen-Doped In2O3 Films Fabricated by Solid-Phase Crystallization”, Journal on Non-Crystalline Solids, 354 (2008) pp. 2805-2808.

[4] S. Ishzuka et al., “Progress in the Efficiency of Wide-Gap Cu(inGa)Se2 Solar Cells Using CIGse Layers Grown in Water Vapor”, Japanese Journal of Applied Physics, Vol. 44, Nov 22, 2005 pp. L679-682.

[5] R.J. Ferran and S. Boumsellek., “High pressure effects in miniature arrays of quadrupole analyzers from 10^{-9} to 10^{-2} torr” J. Vac. Sci. Tech. A 14, 1996 pp. 1258-1264.

Feature Article

Wheel Slip Simulation for Dynamic Road Load Simulation

Bryce Johnson

Increasingly stringent fuel economy standards are forcing automobile manufacturers to search for efficiency gains in every part of the drive train from engine to road surface. Safety mechanisms such as stability control and anti-lock braking are becoming more sophisticated. At the same time drivers are demanding higher performance from their vehicles. Hybrid transmissions and batteries are appearing in more vehicles. These issues are forcing the automobile manufacturers to require more from their test stands. The test stand must now simulate not just simple vehicle loads such as inertia and windage, but the test stand must also simulate driveline dynamic loads. In the past, dynamic loads could be simulated quite well using Service Load Replication (SLR*1). However, non-deterministic events such as the transmission shifting or application of torque vectoring from an on board computer made SLR unusable for the test. The only way to properly simulate driveline dynamic loads for non-deterministic events is to provide a wheel-tire-road model simulation in addition to vehicle simulation. The HORIBA wheel slip simulation implemented in the SPARC power train controller provides this wheel-tire-road model simulation.

*1: Service load replication is a frequency domain transfer function calculation with iterative convergence to a solution. SLR uses field collected, time history format data.

Introduction

To understand why tire-wheel simulation is required, we should first understand the type of driveline dynamics that need to be reproduced on the test stand. Figure 1 is the speed and torque of the left wheel of a manual transmission vehicle accelerating aggressively from rest at the test track. The clutch is released quickly and the tire spins on the dry pavement creating large torque and speed deviations at the vehicle axle shaft. The important characteristics of the torque and speed response are the frequency, the amplitude and the damping of the torque and speed oscillations.

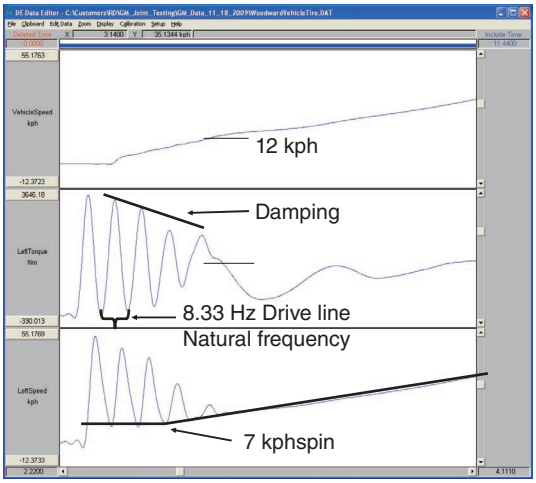

Figure 1

Driveline response of the vehicle

The oscillatory response of the tire-wheel speed and torque is caused by the numerous spring-mass-damper components in the driveline. The predominant frequency seen at the clutch release is the driveline natural frequency. The frequency will typically manifest itself between 5 and 10 Hz for cars and light trucks. (see Figure 2) It is highly dependent on the two inertias and the driveline spring rates.

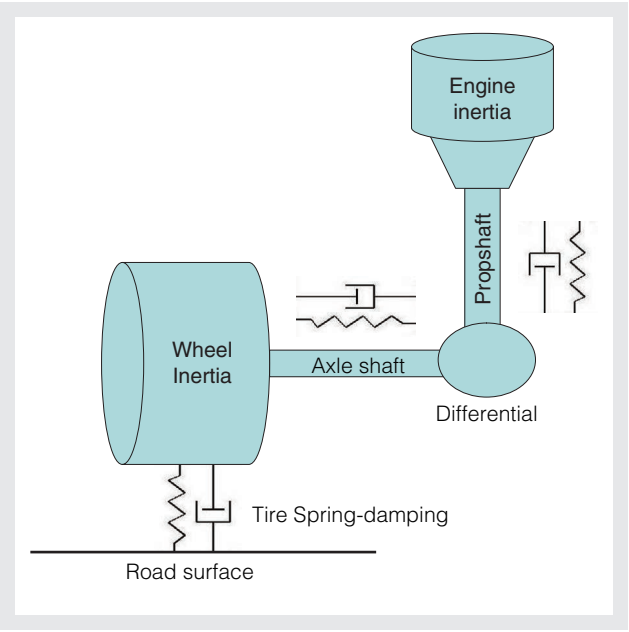

Figure 2

Vehicle on the test stand

When the vehicle is moved to the test stand, the tires and wheels are removed and replaced with a dynamometer (see Figure 3. yellow). To preserve the driveline response, the tire inertia, the tire damping, the tire spring rate and the tire-road surface must be simulated.
Traditionally, the tire-wheel inertia must be replaced by a dynamometer with inertia of identical value. That was the only way to get the correct driveline natural frequency response. The problem is that a dynamometer motor of such low inertia is very expensive to manufacture.
HORIBA's solution is to use a relatively inexpensive dynamometer and use special controls to simulate the tire-wheel inertia. The software and hardware Horiba uses to simulate the wheel-tire-road is called "wheel slip simulation". An additional component is the "vehicle simulation" that provides road loads based on the vehicle design. The software executes on a SPARC controller and is an integral part of the HORIBA power Train controller.

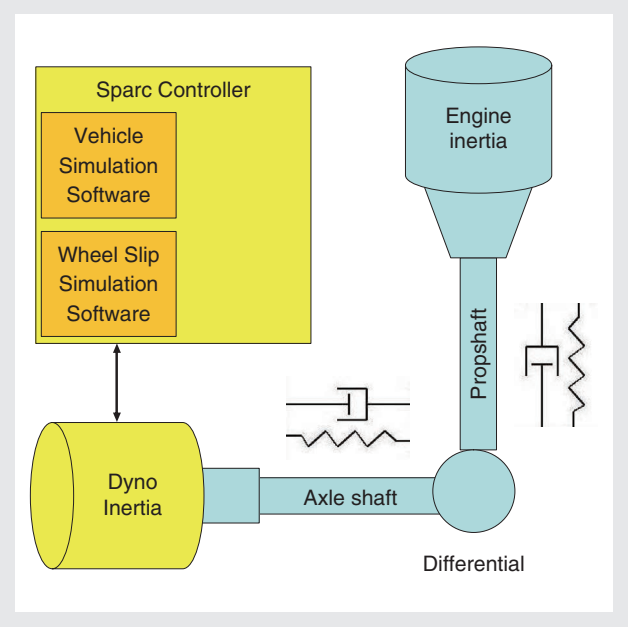

Figure 3

Vehicle Simulation

Vehicle simulation software known as Road Load Simulation (RLS) has been used to provide loads to the driveline via the dynamometers to simulate the vehicle loads. The most basic form of RLS includes vehicle mass simulation, frictional force simulation, windage force and hill incline simulation. The vehicle mass simulation assumed the mass was concentrated at the vehicle center of gravity. Wheel slip simulation distributes this mass to the individual tires depending on vehicle dynamics. A vehicle dynamics simulation in STARS[*2] provides a means to distribute the mass to each tire model in real-time to simulate steering, acceleration and braking weight transfer.
RLS is still used to provide vehicle simulation. Wheel slip is used in conjunction with vehicle simulation to support high dynamic torque events. The road load force is given by an equation that is a function of the vehicle speed.

$$F_{Road} = K_A + K_B * v + K_C * (Speed_{Vehicle} + v_{Headwind})^X + m * g * \sin(Incline_{Hill})$$

$$F_{Veh} = T_{Measured} / Radius_{Wheel}$$

$$Speed_{Vehicle} = 1/m_{Vehicle} * \int (F_{veh} - F_{Road})\, dt$$

*2: STARS is the name of the software product and trademark that

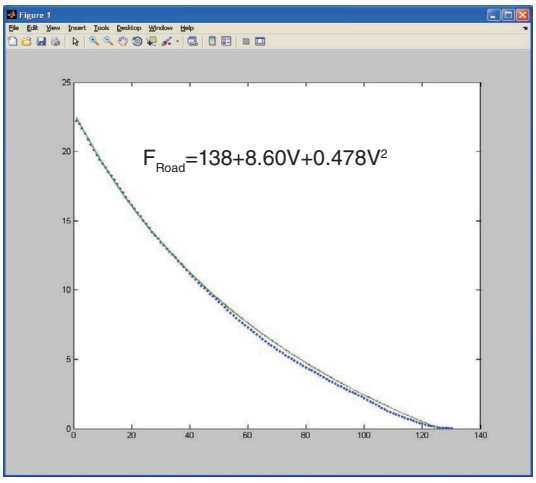

Figure 4

provides all test automation functions.

The difference between vehicle force and road force is the force used to accelerate the vehicle. If we integrate this force acting on the vehicle inertia, the result is simulated vehicle speed. Figure 4 is a comparison of the real vehicle and a simulated vehicle during a coast from 50 mph to zero. This comparison shows how well the simulation (green) matches the real vehicle (blue).

Wheel slip simulation

There are 3 characteristics of the test stand that must be controlled to get proper drivelive dynamics in the simulation. First, the tire forces and tire slip must be simulated using a tire model. Second, the wheel-tire inertia must be simulated to get the proper drive line natural frequency. Third, the damping of the oscillations must be controlled.

The tire model, what is slip?

Most of us are intimately familiar with tire spin events when a tire spins on wet roads or ice. However, not everyone understands that the tire is always slipping slightly; even when a vehicle is moving on a dry pavement. Figure 5 is the data from a real vehicle at a test track on dry pavement. The vehicle speed is 39.4 kph, the front tire speed is 367 rpm and the rear wheel speed is 383 rpm. This is a rear wheel drive vehicle whose rear tires are transferring 4600 N of force. What is seen in this graph is that the rear tires are rotating 16 rpm faster than the front tires. Saying another way, the rear tires are slipping at 16 rpm on the road surface when rotating at

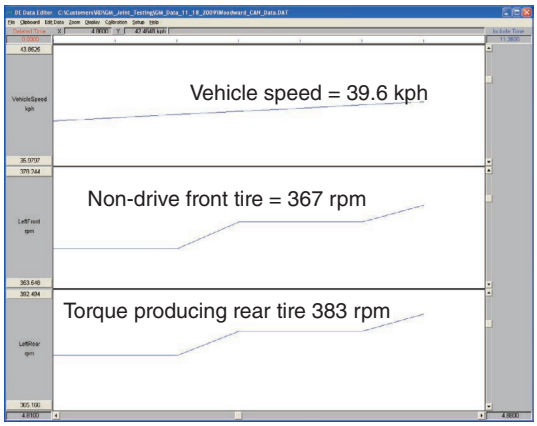

Figure 5

383 rpm while transferring 4600 N of force.
What we find is that vehicle tires slip at a rate proportional to the amount of force they transfer to the road surface. This slippage is what is referred to as wheel slip. If we continue to increase the tire force by accelerating the vehicle more aggressively, a maximum force will be reached and the tire will slip quite dramatically as the tire on ice. One often says the tire is spinning. The test stand must implement a tire model to reproduce this force-slip functionality.
The definition of slip is: Slip= $(V_{Tire}-V_{Vehicle}) / V_{Vehicle}$. If we take vehicle speed as the front tire speed or 367 rpm and the tire speed as the rear tire speed or 383 rpm, we get a slip of 4.4%.

Simulation of tire forces and slip using Pacejka

The traditional way to simulate tire forces and slip is to use a tire model. The traditional tire model describes a functional relationship between slip of the tire and the force transferred through the tire. Although there are a number of tire models in the literature, one of the most well known tire models is the Pacejka-96 longitudinal tire model. This is function that describes the tire force as a function of tire slip. The Pacejka function is $F = D \sin (b_0 \tan^{-1} (SB + E (\tan^{-1} (SB) - SB)))$. "F" is tire force and "S" is tire slip. The parameters D, B, E and S are values based on the tire normal force and the Pacejka parameters b0 to b10. The value F_z is the normal force applied to the wheel. By adjusting the normal force of each tire in real-time using STARS, the test engineer accounts for vehicle body movements that change the weight distribution of the vehicle. (Figure 6)

$$mu_p = b_1 F_z + b_2$$
$$D = mu_p F_z$$
$$B = (b_3 F_z + b_4) e^{-b5 Fz} / (b_0 mu_p)$$
$$E = b_6 F_z^2 + b_7 F_z + b_8$$
$$S = 100 S_{frac} + b_9 F_z + b_{10}$$

Simulation of tire forces and slip using a simple model

Quite often, the test engineer does not have access to the Pacejka parameters. In such a case, the customer can use a simple model to describe the tire forces and slip. The simple model consists of two numbers: the maximum force and the force-slip gradient. These two numbers can be calculated reasonably easy from road data. The tire

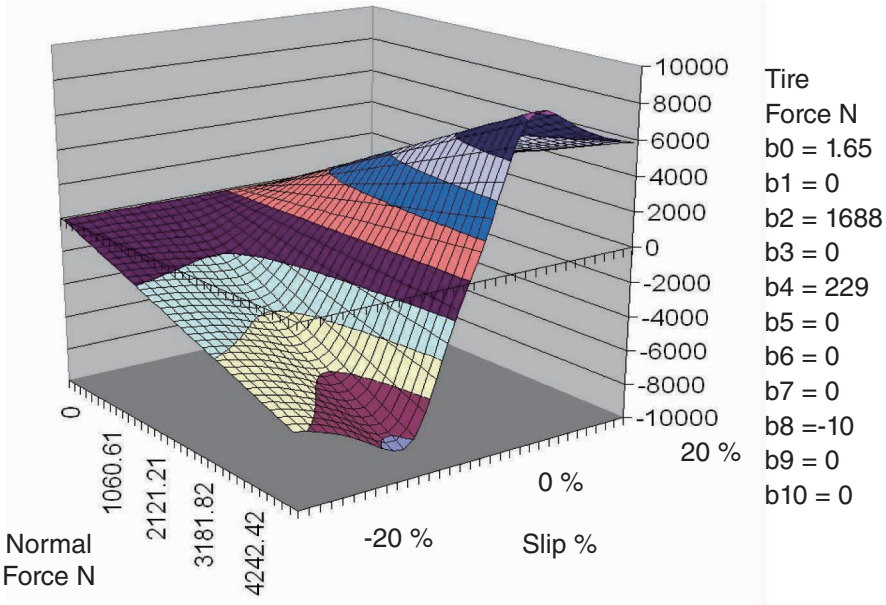

Figure 6

gradient represents the region of operation where the tire slips as a function of torque. The maximum force represents the region of operation where the tire spins quite dramatically rather than slipping slightly. The maximum force also represents the tire force given that a particular normal force F_z exits. As the tire normal force changes, the maximum value changes proportional to the normal force. (Figure 7)

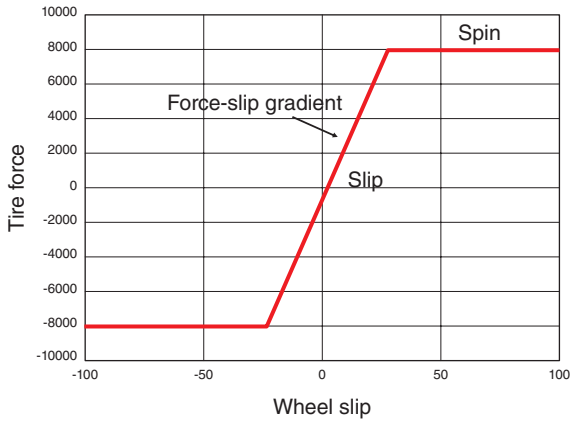

Figure 7

Inertia simulation and damping

A tire model simulation as a requirement for proper wheel slip simulation has been describe as part of a three part solution. Two other critical requirements for wheel slip simulation are controlling the natural frequency and controlling the damping. The natural frequency is highly dependent on the wheel inertia. So it is crucial that the inertia of the tire-wheel combination is simulated. The typical problem is that the dynamometer inertia is greater than the tire-wheel inertia. So the simulation must apply a force to the dyno inertia to compensate for the inertia difference between the dyno and the tire-wheel. The actual means by which Horiba does this is proprietary, but suffice to say it is adjustable with a parameter. Likewise, damping is also controlled by a parameter.

Road surface simulation

Actual road surface simulation is embodied in the Pacejka parameters as mu_p. This value represents the peak longitudinal friction coefficient. A reasonable approximation to the actual friction coefficient is to multiply this value by a normalized coefficient of friction mu_n, which takes on values between 1/10 and 1. Below is a table that provides a reasonable approximation to the road surface mu_n.

Table 1

Surface type	Normalized mu_n
Perfect surface	1.0
Asphalt and concrete (dry)	0.8-0.9
Concrete (wet)	0.8
Asphalt (wet)	0.5-0.6
Earth road (dry)	0.7
Earth road (wet)	0.5-0.6
Gravel	0.6
Snow (hard packed)	0.3
Ice	0.1

The normalized coefficient of friction mu_n is a dynamic value that can be changed in real-time by STARS as a function of road surface. The test engineer simulates a change in road surface by changing this value. A typical test might be to set both tires to dry pavement, then as the test vehicle accelerates, change one of the tires to say snow. A split mu test, as it is called, exercises the traction control logic of the vehicle computer.

Issues of dynamometer sizing

Dynamometers are often sized based on compromises between cost and performance of the components. Typically, high dynamics require low inertia motors and large drives. One must discuss extensively the requirements with the customer to determine the proper dynamometer sizes. A good example is the test in Figure 1 requires a dynamometer which accelerates at 8000 rpm/s. Such a test stand could be built with the following: (Figure 8)

223 kW, Dynas3 4000WH with 600 kW drive
Inertia = 8.8 kgm^2
Peak torque 8109 Nm
Peak acceleration rate 8800 rpm/sec

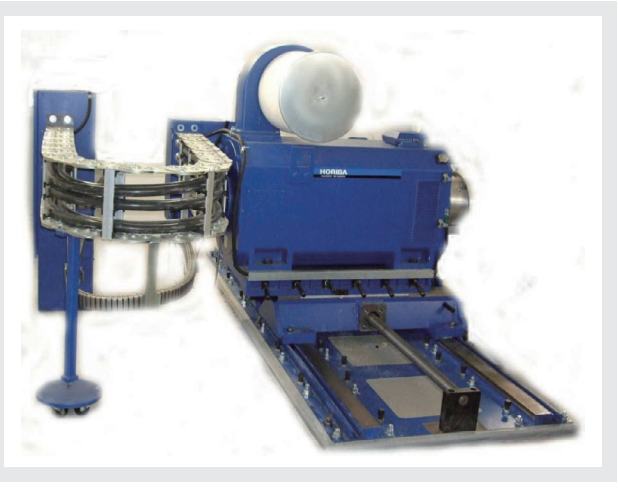

Figure 8

Or it could be built with a high performance PM4000 motor and drive using the following: (Figure 9)

330 kW, Dyas PM4000 WH with 600 kW drive
Inertia = 1.0 kgm^2
Peak torque 4200 Nm
Peak acceleration rate 38,000 rpm/sec

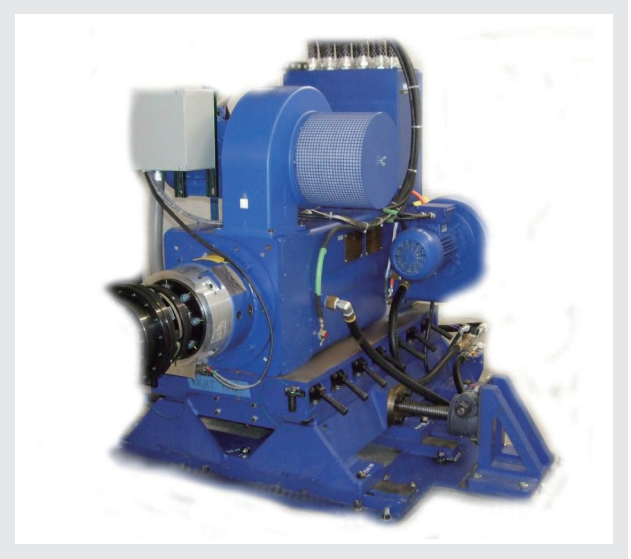

Figure 9

In this case, a less expensive Dynas3 provides the minimum acceleration rate required for the customer requirements at less than ~50% the cost. All dynamometers can provide wheel slip capability; however, the dynamic performance for wheel slip will be determined heavily by the torque-to-inertia ratio, which determines the acceleration rate. As a trade off, the customer may elect to reduce his wheel slip events to lower amplitudes and/or frequency in an effort to reduce the dynamometer costs.
Typically, low frequency tests with large vehicles and less aggressive wheel slip events are suitable for the Dynas3 dynamometers. High frequency tests with smaller vehicles and very aggressive slip events are suitable for the Dynas PM dynamometers.

Results

Driveline natural frequency

The test stand was not able to reproduce the aggressive acceleration event by the vehicle at the test track depicted in Figure 1 because the test stand dynamometers were rated to 6000 rpm/sec and the test required dynamometers rated to 8000 rpm/sec. However, the dynamometers were able to excite the drive line natural frequency at lower amplitudes in other events.
The drive line natural frequency is a function of the inertias and spring rates and is affected only slightly by the damping. As a result, most any step event can excite the natural frequency. Shown below is a spin event on

snow created by a sudden acceleration by the engine. It clearly shows the driveline natural frequency of 8.33 Hz that we saw in Figure 1 during the aggressive acceleration event of the vehicle on dry pavement at the test track. (Figure 10)

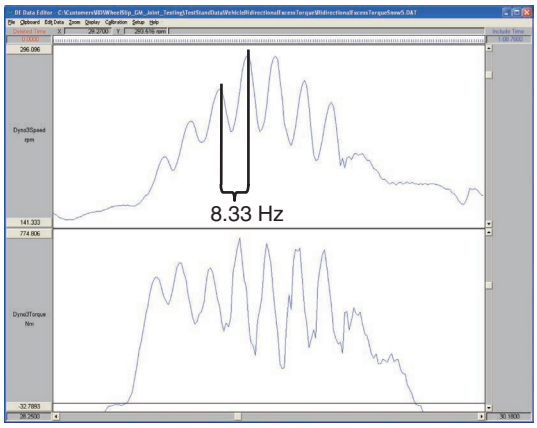

Figure 10

Wheel slip model check

As a check to verify the wheel slip model, the slip gradient as calculated the slip gradient from the tire force and slip. It should agree with the slip gradient for the model of 101904 N/slip. Below, the measured slip gradient is 102,639 which is within 0.7% of the expected value. This value is derived by first calculating the tire force from the torque transducer. Then calculate the slip as the difference between the vehicle speed and the measured tire speed. The gradient is calculated by dividing the tire force by the slip. (Figure 11)

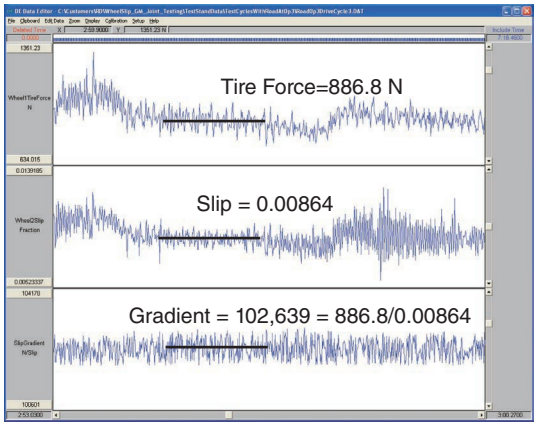

Figure 11

Conclusion

Wheel slip is a current development at Horiba. Near future development will provide correlation between the vehicle data and the wheel slip simulation data. The current test stand is limited by the dynamic capabilities of the current dynamometers at 6000 rpm/s compared to the required acceleration rate of 8000 rpm/s, so some verification is yet to be done.

Future development might include sophisticated road surface simulation including bumps. Yaw sensor simulation for vehicle computers would provide inputs for onboard vehicle computers for testing stability controls.

Currently, the algorithm successfully recreates the driveline natural frequencies, which means inertia simulation works correctly. This is an industry first in dynamometer test stand simulation for wheel slip. Also successfully implemented are the two tire models as presented. Testing included the slip-spin events working correctly with proper wheel forces. Dynamic split mu tests are possible. In addition, dynamic weight adjustment on individual wheels is provided supporting varying weight distribution caused by body roll, cornering and acceleration.

The current implementation provides a longitudinal model which is expected to provide the 99% market requirement. Two tire models are provided as discussed. If the market demands change, the SPARC controller is flexible enough that the models can be extended as required.

Bryce Johnson
Principle Engineer
Automotive Test systems
HORIBA Instruments Inc.

Feature Article

Testing Electrified Drivetrains for Vehicles without the Battery or Engine.

Norm Newberger, Bryce Johnson

The hybrid electric vehicle (HEV) is becoming a sustainable vehicle architecture with the US government pouring 14.4 billion[1] into stimulus projects that support drivetrains of new vehicles that are hybrid or battery powered (BEV). Both the series hybrid and BEV have 100% of propulsion energy coming from electricity. The series hybrid uses an internal combustion engine (ICE) to power a generator that produces electricity. The parallel hybrid powers the vehicle by a mechanical combination of electric motors and ICE. In all cases, the drivetrain needs an electric motor, a traction battery and an auxiliary method of obtaining electricity. These auxiliary power units (APU) are typically a downsized, highly efficient ICE or fuel cells for a zero emissions alternative. Horiba's Virtual Engine (VE) and Virtual Battery (VB) are HIL[2] products that allow electric motor based drivetrain development without waiting for the new battery pack and ICE to become available. Relevant product features for HEV development are discussed in terms of form, function, and verification with data.

INTRODUCTION

Historically, the verification, validation & controller calibration of vehicles was brought in from the proving grounds to the laboratory using chassis dynamometer simulating the road. Figure 1 illustrates this concept using HORIBA's automation system (STARS) and dynamometer controller (SPARC). The difficulty here is that the entire vehicle needs to have all its intended components in a pre-production state. By expanding the simulation capabilities of the dynamometer controller to include simulation of missing subsystems not under development, subsystem or component testing can occur anywhere a dynamometer can be conveniently connected, Figure 2 illustrates this concept for the physical ISG[4] electric motor being developed for a HEV. The vehicle's kinematic characteristics, tires, differential, transmission, and torque converter are simulated for their power flow to result in torque or speed set points to the dynamometer attached to the ICE crankshaft output. This configuration suffers form the lack of availability of the ICE and battery pack intended for the vehicle. Both are high value, sophisticated subsystems undergoing their own development process involving different parts of the organization and supplier network. E-motors are also being considered at other locations in the drivetrain. They can be located in the wheels, differential, transmission, or front end accessory drive (FEAD) in addition to the end of the crankshaft. These various alternatives add to the complexity of integration and calibration for the vehicle, thus requiring very early testing in the development process. The power of the battery pack can be simulated by controlling the voltage output of a high power, programmable DC to DC converter using a real time model of the battery chemistry. Additionally, the torque output of the ICE can be simulated by a real time model of the ICE combustion process and mechanical configuration. Figure 3 illustrates the use of a VB and VE with actual hardware to produce the electrical and mechanical power. This report will point out VB and VE implementation, relevant features exclusively for HEV development, and comparisons to measured data from real battery packs and ICE.

Figure 1[3]

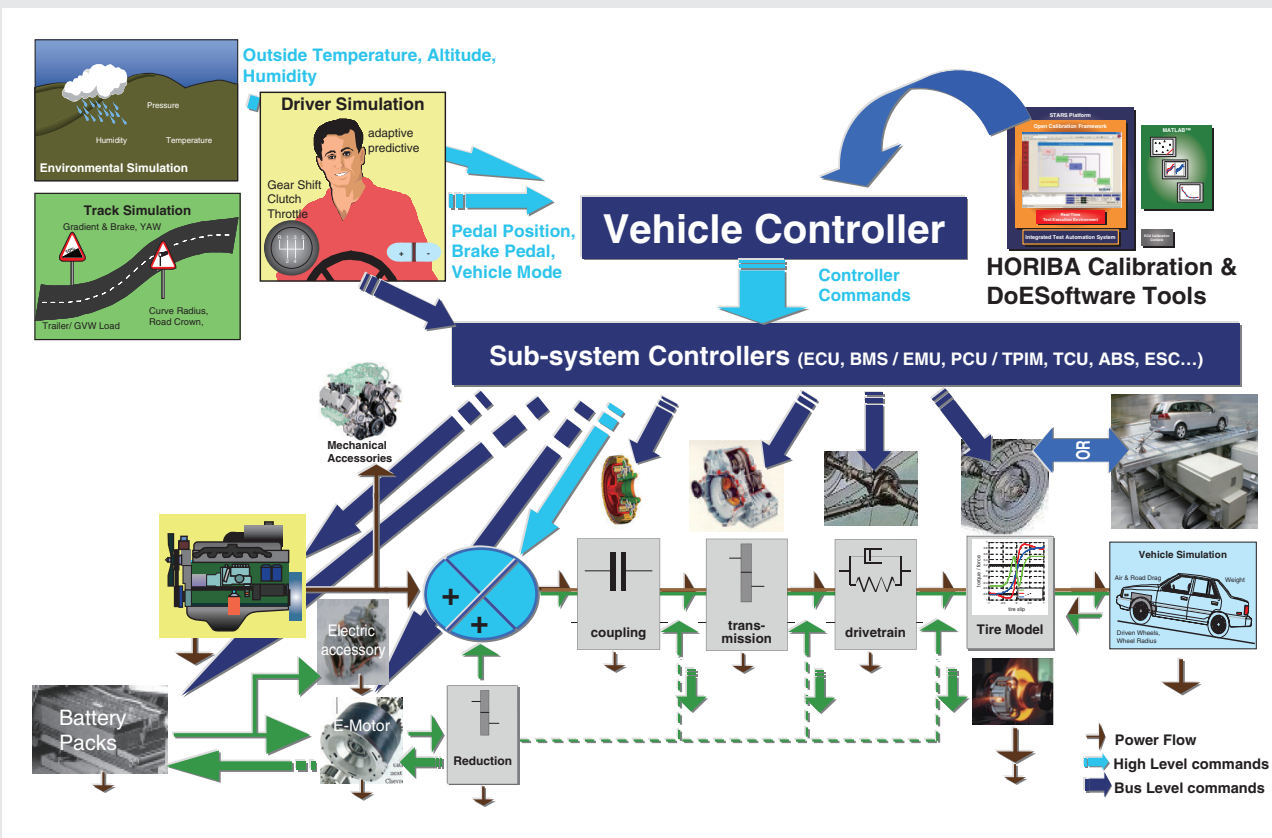

Figure 2

Feature Article Testing Electrified Drivetrains for Vehicles without the Battery or Engine.

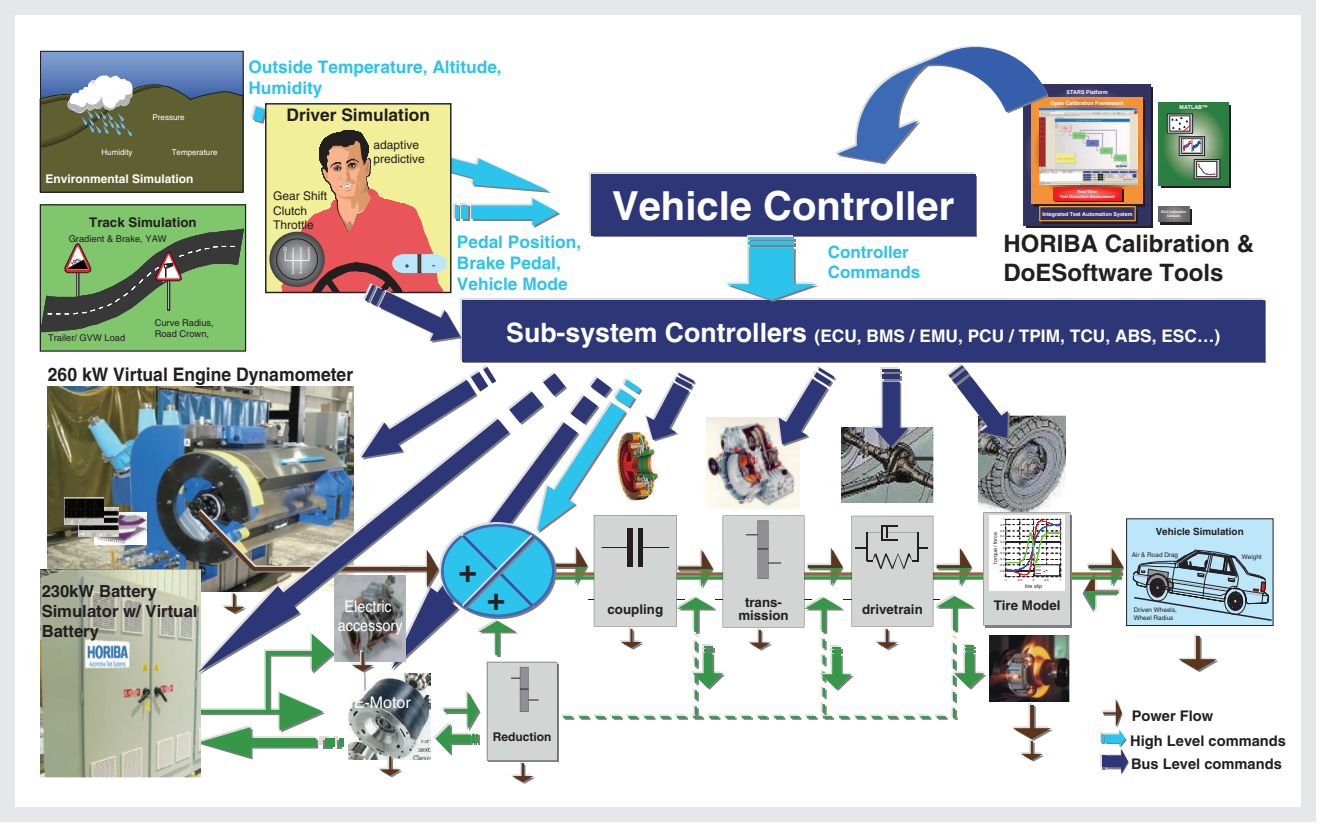

Figure 3 Simulation Diagram: VB & VE in drivetrain test stand (loading dynamometer not shown)

Virtual Engine Capabilities

The engine simulation controls the input dynamometer. Engine simulation provides sensor and data communication inputs to the transmission control unit (TCU) to mimic being connected to a the real engine. The engine simulation is influenced by ambient conditions (simulated or measured in the test cell) such as atmospheric pressure. Pedal position controls engine torque. Figure 4 is a block diagram of VE interface capabilities.

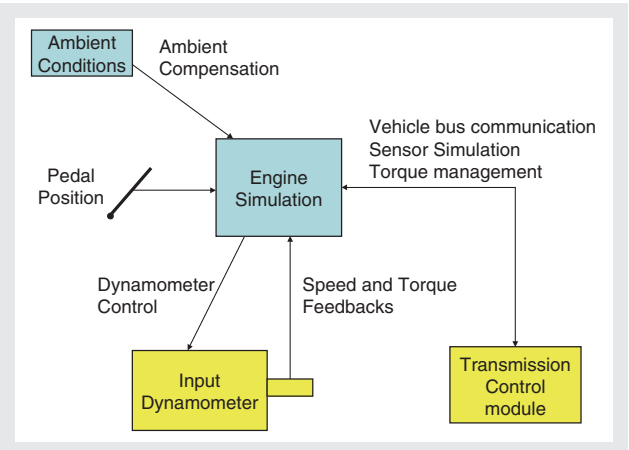

Figure 4

Engine simulation functions for the transmission input

The engine simulation consists of maps, an engine controller, a parametric model similar to the mechanical engine, and an adaptive mechanism. The engine controller controls cranking (start & stop), idling and torque reduction during a gear shift. It also simulates the various engine/ECU delays. A parametric engine model calculates torque due to the kinematics of the parts (pistons, connecting rod, crankshaft, and flywheel) and gas pressures. An adaptive mechanism assures that the response torque amplitude follows the demand amplitude. It also provides a means to limit frequencies and orders. Engine simulation provides the following functions:

1) inertia simulation,
2) throttle and pedal map simulation,
3) torque reduction during shift,
4) ECU torque management interventions,
5) engine cranking,
6) engine idle control,
7) ignition simulation,
8) coast simulation,
9) fuel cut and closed throttle simulation,

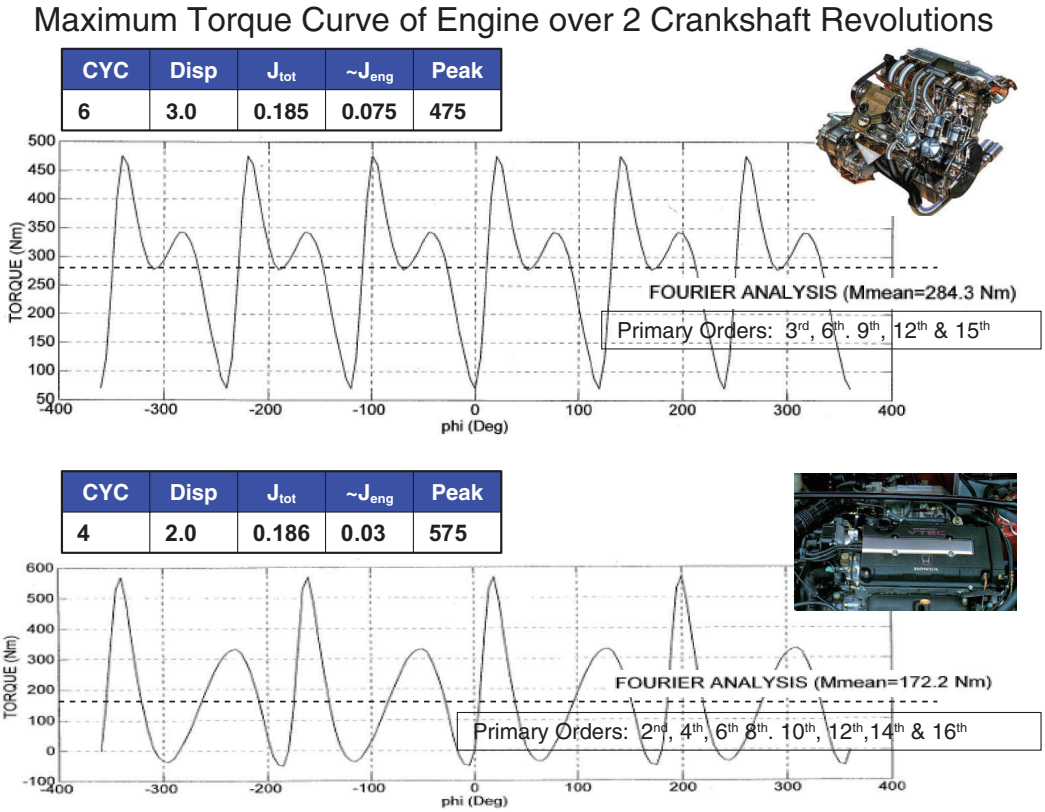

Figure 5

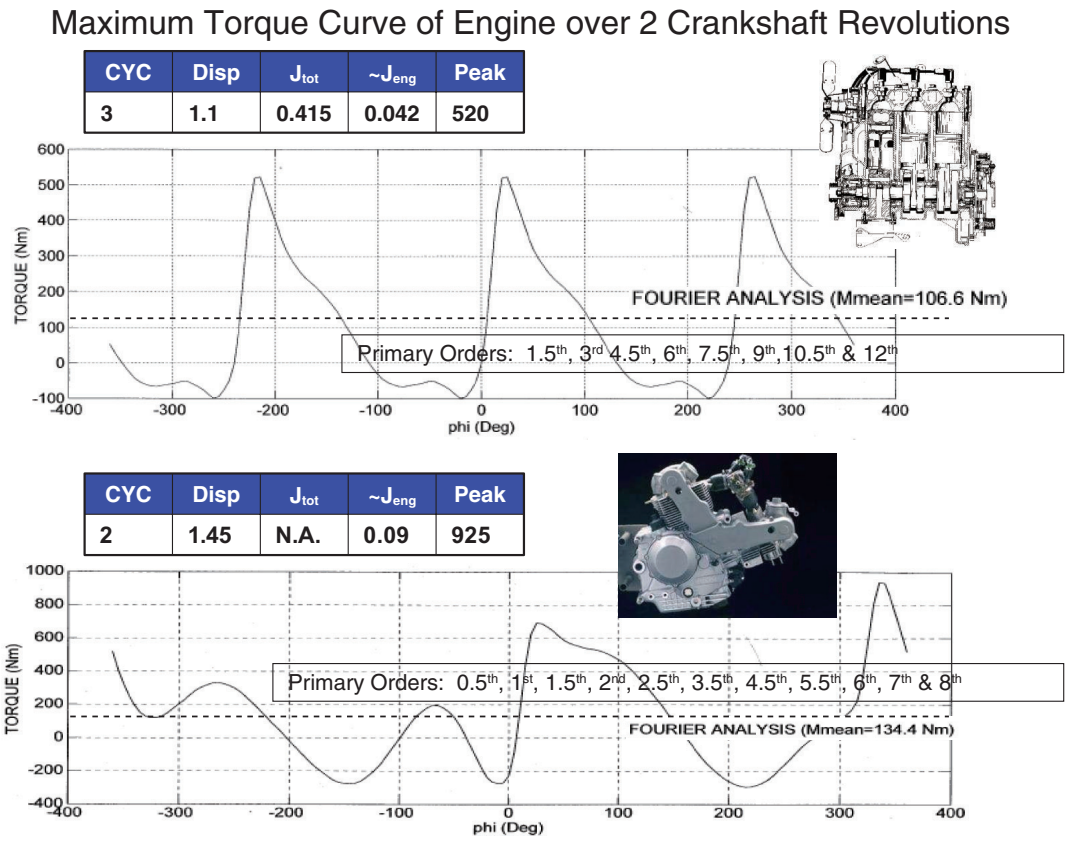

Figure 6

10) engine torque pulse simulation (ETPS) from the combustion process,
11) cylinder firing reduction,
12) front end accessory & generator loading, and
13) ambient condition adjustment.

ETPS includes simulation of fuel type (gasoline, diesel) and boost (turbo-charged, super charged or normally aspirated). Two and four cycle engines are supported from 1 to 16 cylinders. The following two figures show torque pulse waveforms at peak power of ICE engines being refined for HEV. These are characteristic torque signatures of the engine's mechanical configuration.

Pedal map simulation

Current generation engine technology uses fly-by-wire throttle control. This imposes additional simulation responsibility on the engine simulation to reproduce the demand from the "gas" pedal to throttle demand in the engine simulation. Typically this requires a set of maps found in the ECU to interpret pedal demand into throttle position. The throttle position is then sent to an engine map to create the proper engine torque output. Pedal mapping is highly dependent on vehicle calibration. Figure 7 shows an open loop approximation of pedal to throttle simulation.

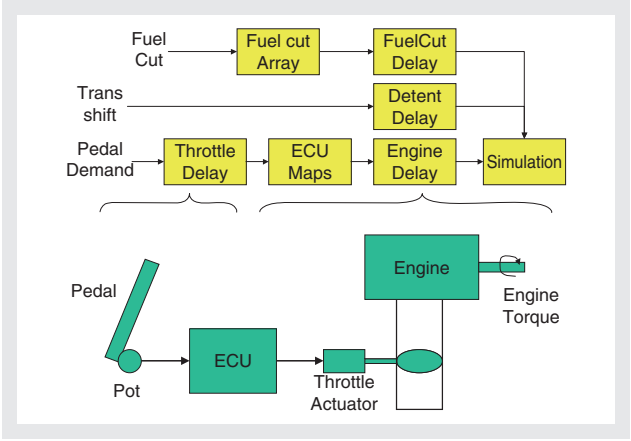

Figure 7

Engine torque map simulation

An engine is typically throttle controlled. Based on the throttle setting and the current engine speed, the engine will produce a given torque. On the other hand, a dynamometer is speed or torque controlled. Unlike an engine, the electric dynamometer can produce maximum torque at zero speed. Some method is required in the engine simulation to limit the dynamometer torque to the average torque that the engine would produce and to create the throttle-to-torque function to mimic the engine. Engine torque map simulation provides this capability. Figure 8 is an engine map for the engine simulation. A throttle demand sent to the engine simulation is used along with the dynamometer's measured speed to determine the torque that the engine simulation should produce. Since many vehicles are now "fly-by-wire," ECU implementations also provide additional mapping to map the pedal position to an internal throttle or torque demand. This additional pedal mapping may be a function of vehicle speed, battery state of charge, and other parameter(s) as the vehicle controller calibration deems appropriate.

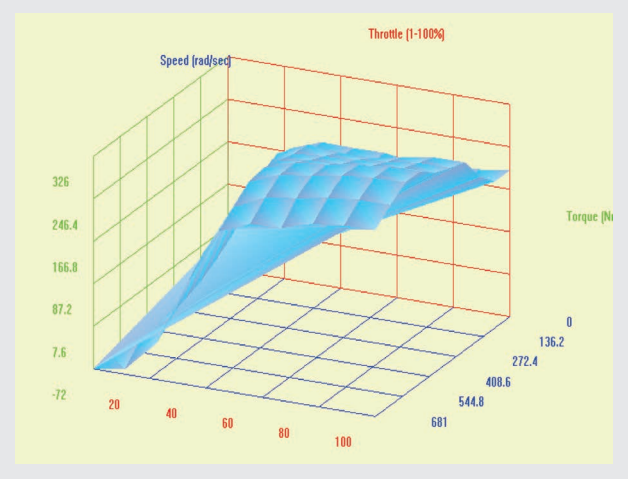

Figure 8

Engine inertia simulation

Drivetrain testing requires that the engine inertia is correct so that the load on the transmission is equivalent between the real engine and the dynamometer performing the engine simulation. Often, the dynamometer inertia is larger than the engine inertia, so compensation (inertia simulation) is required. A combination of engine speed observers and feed forwards allow a robust implementation of the dyno torque (T_{el}) needed to simulate the inertia of the engine and its flywheel. This torque is added to the torque being from the torque map simulation.

$$T_{el} = \frac{J_{el} + J_{FW}}{J_{sim} + J_{FW}} T_{eng} + \left(1 - \frac{J_{el} + J_{FW}}{J_{sim} + J_{FW}}\right) T_{trans}$$

$$= K^{*} T_{eng} + (1 - K)\, T_{trans}$$

In Figure 9, the VE is run in throttle/speed with the throttle ramped in an attempt to hold the torque relatively constant during a shift. During this part of the shift, the deceleration is constant. This results in the engine speed decelerating from 3900 rpm to 900 rpm. The speed change results in an inertia torque. If the dynamometer inertia and engine inertia are the same (top Chart), no compensation is required. The bottom chart shows where the dynamometer inertia is twice the engine inertia and the need to add compensation torque.

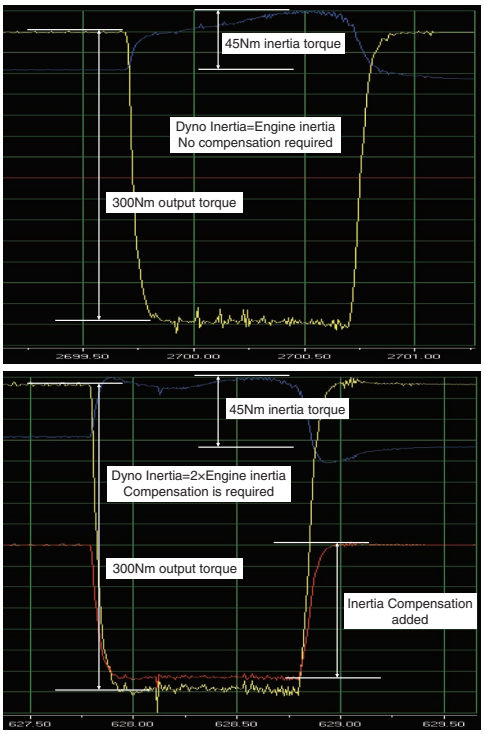

Figure 9

Engine torque pulse simulation

Figure 10 shows an 8 cylinder engine running at 2000 rpm, part throttle with a mean torque of 118 nm. The mean torque is not shown on this display. Only the torque pulses are shown. We clearly see 8 distinct pulses, one combustion event in each cylinder, over the 720 degrees (two crankshaft rotations). To produce 118 Nm of mean torque, we must produce 145 Nm of firing pulses.

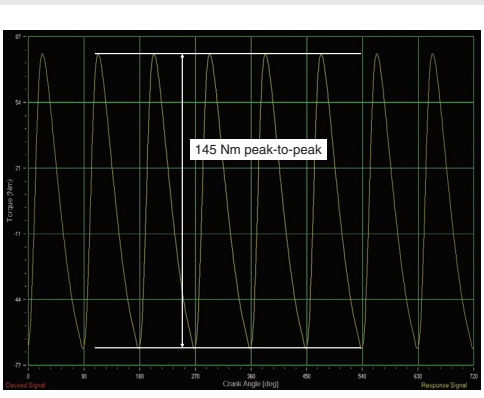

Figure 10

Validation of simulation to real engine data

Validation of the engine simulation is crucial to the acceptance of the algorithm. A comparison between in instrumented crankshaft in a 4 cylinder gasoline engine (bottom chart) and the engine simulation (top chart) is shown in Figure 11. The correlation between simulation and the engine is excellent with the matching of firing order frequencies and closeness in amplitude.

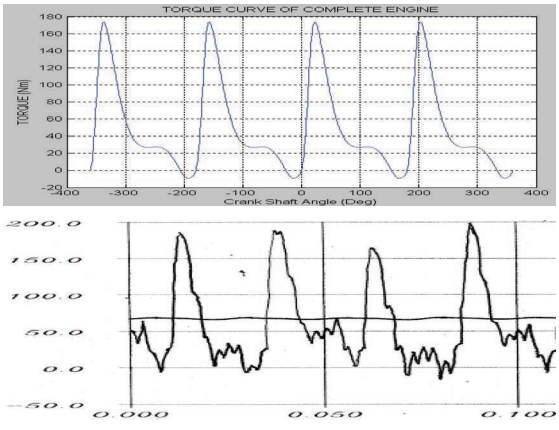

Figure 11

Table 1 shows the amplitude of the spectral components of the engine simulation and the real engine. Inconsistent firing and certain torsional resonances from the transmission present in the measured data may attribute for the minor differences.

Table 1

	Real Engine	Simulation
40 hz	37 nm	37 nm
80 hz	23 nm	30 nm
120 hz	8 nm	15 nm
120 hz	8 nm	15 nm
160 hz	5 nm	7 nm
200 hz	3.7 nm	5 nm
240 hz	1.4 nm	2.5
280 hz	1.1 nm	2
320 hz	0.9 nm	1.5

Startup/shut down simulation including HEV start

The typical startup profile for an engine is shown below. Idle speed, crank speed and their ramp rates are controlled. After cranking for a fixed period of time, the

speed ramps up to idle speed and the idle speed controller takes over. Torque limits are placed on both cranking and idling. HEV startup for hybrids is easily parameterized by adjusting these parameters to shorter time intervals.

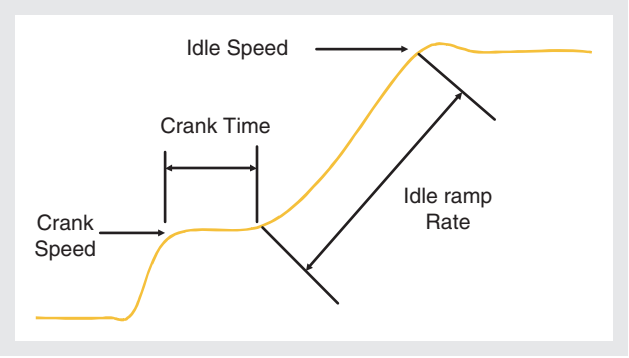

Figure 12

Engine shutdown/coast is controlled by the ignition, engine map near zero speed and the **StandStillSpeed** value. The engine map determines what torque is applied to cause the engine to stop. The StandStillSpeed value determines when the dyno command is zeroed.

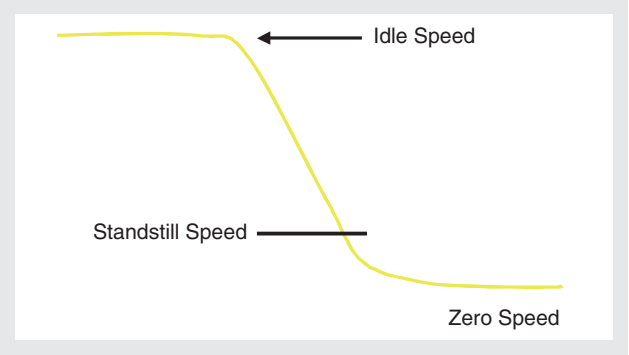

Figure 13

Figure 14 shows engine startup simulation with ETPS (engine torque pulse simulation) turned on. Note that for all engine simulation, torque pulses can be turned on or off. If turned off, then only mean engine torque is simulated. The engine first cranks for a short time after which the engine starts firing and accelerates to idle speed. Prior to firing and during cranking, engine torque pulses are the result of pumping forces in the engine.

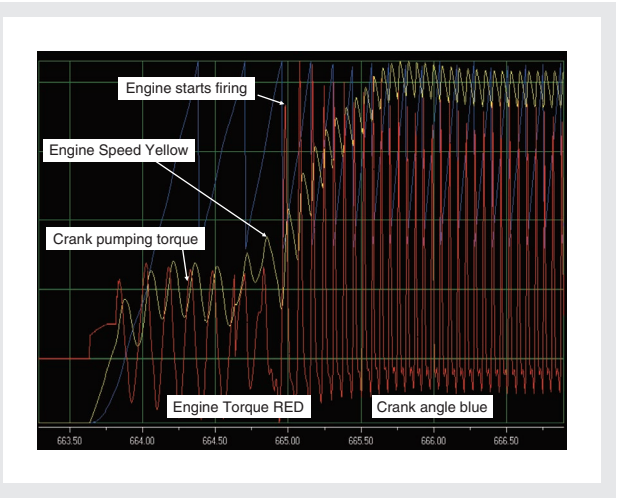

Figure 14

Special requirements for dynamometer motors and drives for engine simulation

The dynamometer needs a proper torque to inertia ratio to accomplish > 50,000 RPM/sec accelerations and sub millisecond current rise times required for engine torque pulse simulation. Physical rotor properties (inertia and stiffness) must have first a torsional natural frequency > 600 Hz when connected to the transmission under test. Additionally, in vehicle engine position is duplicated by the tilt and height adjustment of the support base.

Figure 15 pictures a 0.084 kg-m^2 inertia, 800 Nm peak torque, engine simulation dynamometer designated as Dynas TP260

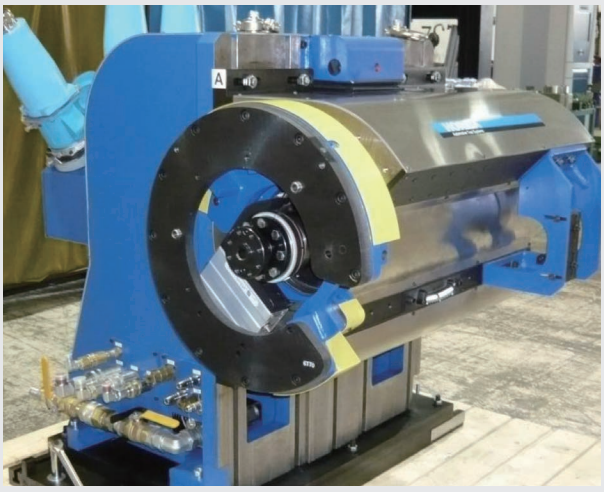

Figure 15

Battery simulation for HEV transmissions and drivetrains

HEV drivetrains require a battery or a battery simulator to test the electric motor. Horiba provides a battery simulator to provide the power to operate the HEV motor. The battery simulator consists of a power source to supply DC power and the software to simulate battery conditions and control the supply of voltage and current from the power source. Interface cabinets connect the power source to the customer specific HEV electric motor controller (PCU, TPIM, other).

Demand for power, current, voltage, or power + additional current can be used to simulate battery operating modes. The battery simulator simulates realistic battery output current, output voltage, power, state of charge (SOC[6]), pack temperature, cell/module temperature difference, power limit, pack resistance, and capacity. Battery pack life (new, 5 years old, 10 years old) is simulated by adjustments to capacity and slew rates.

A battery pack is configured based on cell chemistry and the number of cells placed in series and parallel. Any nominal voltage, power, or capacity can be configured. Figure 16 is a high level block diagram of the VB system.

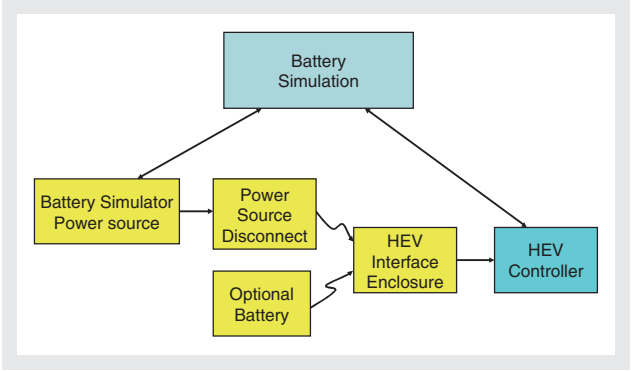

Figure 16

Different battery technologies simulation

A number of HEV battery pack models incorporating chemistries such as Li-Ion, $LiFePO_4$, NiMH, and Lead Acid AGM[7] are supported by the battery simulation software. In addition, interfaces to simulate RLC (resistor-inductor-capacitor) based custom, user defined, battery models are provided.

Horiba's real time model is based on a proposal from Min Chen in the IEEE Transactions on Energy Conversion, Vol. 21, NO2 June 2006 and is shown in Figure 17.

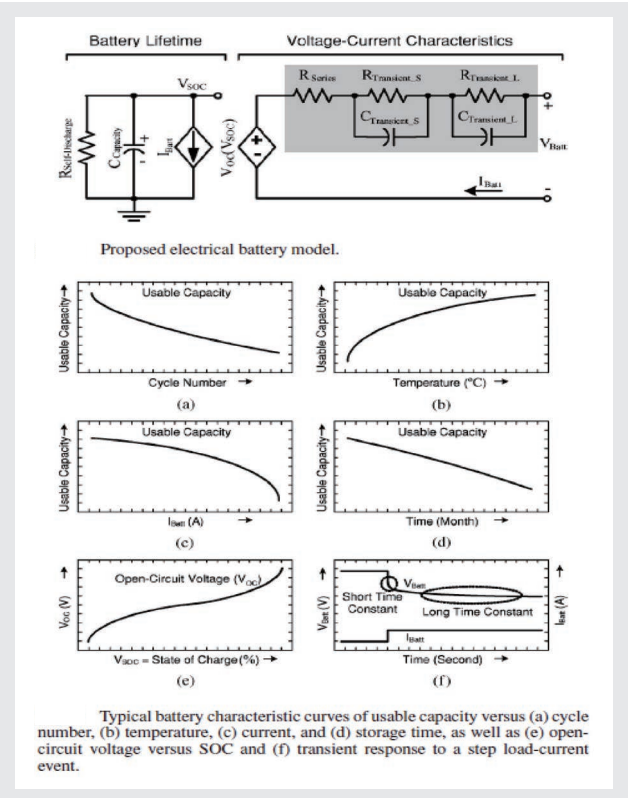

Typical battery characteristic curves of usable capacity versus (a) cycle number, (b) temperature, (c) current, and (d) storage time, as well as (e) open-circuit voltage versus SOC and (f) transient response to a step load-current event.

Figure 17

State of charge simulation

The battery simulation incorporates SOC (state of charge), DOD (Depth of Discharge), and power limits to simulate the HEV/EV/PHEV battery packs. Shown below is the state of charge of various battery packs over a 23 minute FTP simulation.

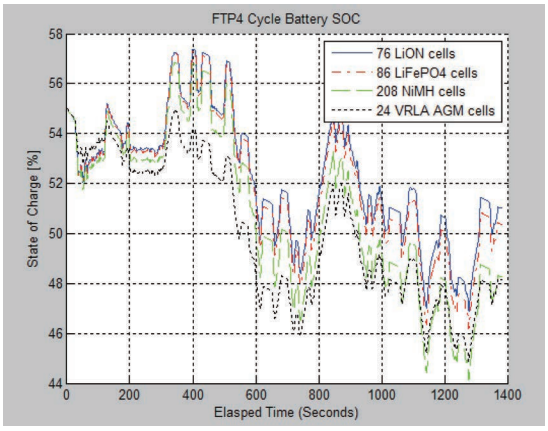

Figure 18

Temperature effects simulation

The battery simulation incorporates thermal simulation to show temperatures values in the battery pack. Shown below is a simulation of temperature for the various

battery technologies. Besides the heat produced by the battery pack, temperature affects every single parameter and condition of each battery cell. All of these parameters and variables must be updated as a function of temperature as well as energy use.

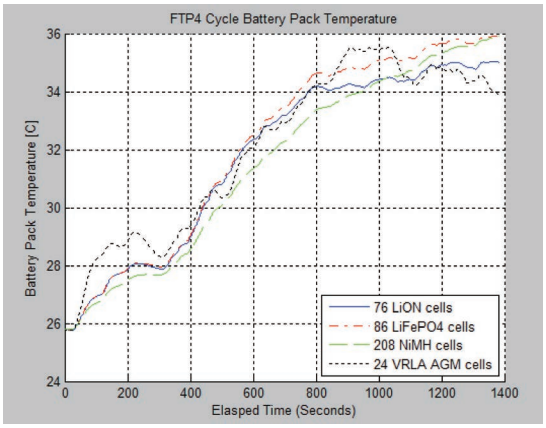

Figure 19

Residual bus simulation

A complete simulation of the battery pack requires CAN (or other vehicle bus) communication with the TCU or ECU. For instance, the TCU may require state of charge to determine if the HEV motor can provide power or the engine should provide power. The Horiba controller provides multiple CAN channels to support this communication. Approximately 200 variables are available to be sent or received over the CAN bus connection to/from the battery simulation.

Horiba products to support Battery simulation

Of crucial importance is that power must be safely distributed in the transmission test cell. Convenient plug-in style connectors provide safe connection to the HEV motor controller and power source. Two interface cabinets provide connection between the transmission HEV motor and power. The first cabinet (hybrid interface enclosure) connects the HEV motor controller to the power source. The power source may be the battery simulator or it may connect to an actual battery. The second cabinet, the wall mounted connecting box is the DC power disconnect. It provides connection between the battery simulator power source and the hybrid interface cabinet. The two enclosure system assures safe, convenient connection between power source and HEV motor.

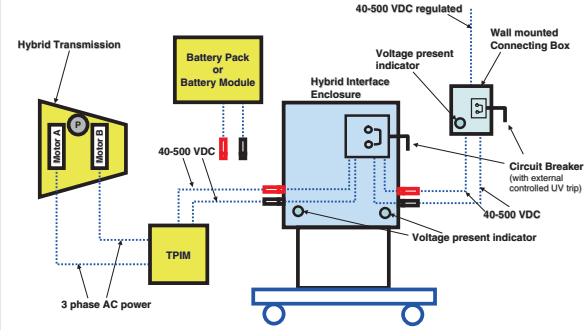

Figure 20

Shown below is the hybrid interface enclosure. The front view shows the disconnect and power on indicators. This enclosure provides loss of isolation detection and it is connected into the emergency stop chain to support power removal without damaging the HEV motor controller. It is rated up to 600 VDC. The enclosure rear view shows the convenient power connectors.

Enclosure front view Enclosure rear view

Figure 21

Comparison of Voltage, SOC, and Temperature to real battery packs

The amount of current going into and out of the battery pack over time defines the usage. The same current (amp) time history was a applied to our models of NiMH and LiFePO4 to validate real time accuracy for the critical variable of voltage, SOC, and temperature. These are critical to determine performance with the e-motor, and battery pack design.

Figure 22 shows voltage versus time between a simulated and real battery pack. The <1% RMS overall deviation is excellent for drivetrain development. Instantaneous deviations can be attributed to errors in understanding the components in the measured current since it will have battery pack current and generator current. Often times, in order to maintain catalytic converter optimum temperature for minimal emissions, the calibration of the ICE requires running the engine into a generator load that has power wasted into the air conditioning system.

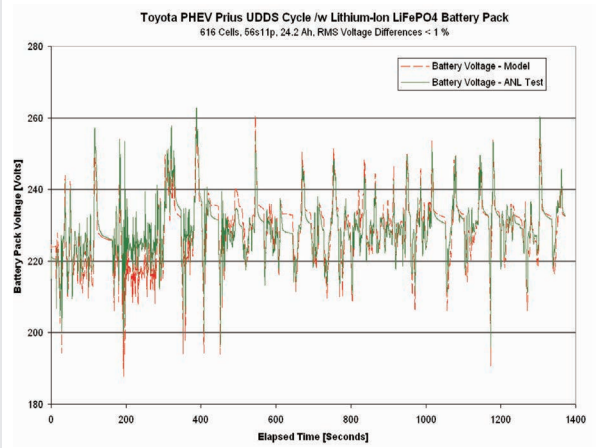

Figure 22

SOC is critical for vehicle performance calibration, battery pack sizing, and BMS validation. Figure 23 plots SOC state between the real and simulated battey.

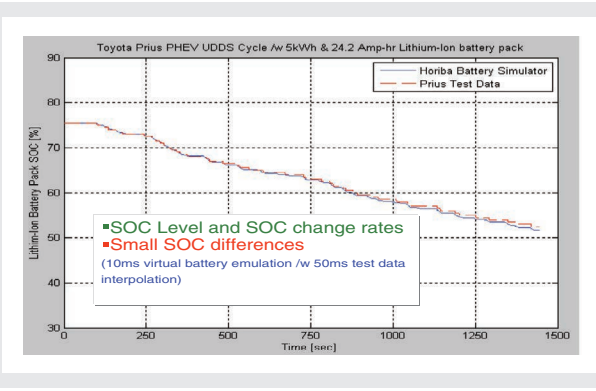

Figure 23

Verification of safe operation during any driving ambient temperature condition and vehicle power demand is a paramount concern when integrating large batteries into a vehicle. Adequate prediction of cell and pack temperature will influence pack cooling systems, packaging, and vehicle calibration. The next figure illustrate VB's temperature prediction.

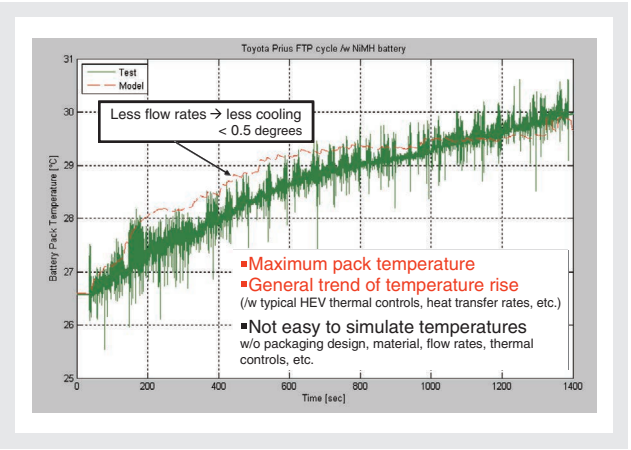

Figure 24

Conclusions

The accuracy and fidelity of VB and VE HIL simulations will allow OEMS to develop electrified powertrains as a parallel activity to engine and battery development. This reduces the time to market for HEV and allow a more precise requirements definition to those designing engine and battery packs.

VB and VE will become quintessential tools to vehicle builders as HEV's seek a 7% to 15%[8] penetration in new vehicle production and is an opportunity for Horiba to offer comprehensive testing solutions. The library of cell chemistries will expand to include Sodium batteries for the heavy duty vehicle and others that show promise in light duty vehicles.

References

[1] IDtechex,com "Hybrid and Pure Electric Cars 2010-2020" Research Report

[2] HIL commonly referred to as hardware in the loop where something physical is used to create power, or run programs, or create a response but inputs and outputs are simulated from a mathematical model of their real end use condition.

[3] ECU, Engine Control Unit; BMS / EMS , Battery Management System + Energy Management System; PCU/TPIM, Power Control Unit aka Traction Power Inverter Module aka Integrated Power Electronics....; TCU, Transmission Control Unit; ABS, Anti-lock Braking System,; ESC, Electronic Stability Control

[4] Integrated Starter and Generator (ISG) is an electric motor attached to the crankshaft of the ICE that acts as motor to start the engine and as a generator of electricity when the ICE is running. Since it is directly on the crankshaft, this becomes a parallel hybrid vehicle. Electric motors used vehicle propulsion are called E-MOTORS to distinguish their unique construction and power output.

[5] CYC = Number of cylinders, DISP = displacement (combustion volume), J_{tot} = Total inertia (engine + flywheel), J_{eng} = Inertia of crankshaft mechanism, Mmean= Rated / Published torque rating of engine, Peak = Largest torque produced as a pulse in combustion process

[6] SOC - State of Charge is a calculation of the BMS showing charge availability of the battery pack

[7] AGM - Absorbed glass mat and Gel Batteries are classifications for low maintenance valve regulated lead acid (VRLA) battery

[8] Various predictions from research institutes, auto analysts for HEV, PHEV, EV market volume by 2015 as part of total vehicle production in the USA.

Norm Newberger
Manager
Drivetrain Technology
Automotive Test Systems
HORIBA Instruments Inc.

Bryce Johnson
Principle Engineer
Automotive Test Systems
HORIBA Instruments Inc.

Feature Article

Development of a High Temperature Exhaust Flowmeter for Diesel Emission Measurements.

Masanobu Akita, Tim Nevius

Direct measurement of engine exhaust volume is often required in determining vehicle or engine mass emissions. The most accurate exhaust flowmeters use ultrasonic transducers to measure exhaust gas velocity with 1% accuracy. Available ultrasonic exhaust meters are limited to exhaust gas temperatures of less than 400 degrees centigrade. These exhaust meters are not suitable for use with diesel engines, because the exhaust gas temperatures can exceed 600 degrees centigrade under heavy loads, or when Diesel Particulate Filter (DPF) regeneration occurs. A new type of ceramic ultrasonic transducer that is rated for exhaust gas temperatures greater than 600 degrees C is being developed. An ultrasonic exhaust flowmeter with these high-temperature transducers can be applied to diesel engine and emission tests without limitations for engine size or load.

Introduction

Internal combustion engine mass emissions can be quantified by measuring the gas concentration and the total exhaust volume, where the mass is equal to the gas concentration multiplied by the exhaust volume and density. The exhaust volume is normalized to standard temperature and pressure, and reported as standard cubic meters per minute (SCMM). Accurate emission measurement requires an exhaust flow measurement with 1% accuracy. Current technology[1] uses ultrasonic flow meter components to directly measure the exhaust gas velocity through an exhaust pipe. A schematic of an ultrasonic exhaust meter (Figure 1) shows the gas velocity determined by measuring the transit time for an ultrasonic pulse to travel upstream (T_1) and downstream (T_2) across the exhaust pipe. When the gas velocity is zero, the transit times are equal, where T_1 is equal to T_2. At increasing gas velocity, the difference in transit times will increase proportionally. It is necessary to correct for speed-of-sound, gas density, gas temperature, ultrasonic transducer delay time[2], and smaller second-order effects to deliver an accurate gas velocity and volume.

Gasoline internal combustion engine vehicles generate exhaust gas temperatures in the range of 100-400 °C. Exhaust temperatures of diesel engine can exceed 600 °C. The piezo-electric crystal in an ultrasonic transducer is limited to a maximum temperature of 250 °C, which is the Curie temperature of the crystal. Heating the crystal beyond the Curie temperature depolarizes the device and destroys its performance as an ultrasonic transducer. The ultrasonic transducers are inserted directly into the exhaust gas stream, so maintaining the piezo crystal element below the 250 °C temperature limit is a challenge when the exhaust gas is at a temperature of 400 to 600 °C.

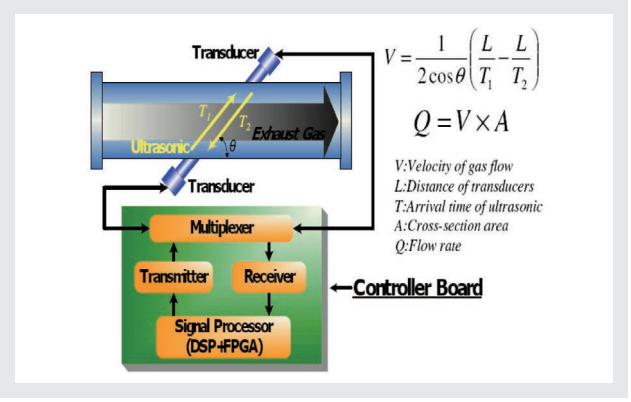

Figure 1 Outliine of an ultrasonic flowmeter

Description of the Present Exhaust Flow Meter

The HORIBA EXFM-1000 is an Exhaust Flow Meter that accurately measures exhaust flow-rate directly at the vehicle tailpipe. The EXFM-1000 is designed to be paired with a Bag Mini-Diluter. The EXFM and Bag Mini-Diluter is an alternative to Constant Volume Sampling (CVS) Techniques and provides the improvements necessary to address the testing of Partial Zero Emission Vehicle (PZEV) and Super Ultra-Low Emission Vehicle (SULEV) emissions.

Figure 2 shows the key components that make up an EXFM and BMD system. One of the critical factors for partial flow bag sampling is accurate measurement of the exhaust flow-rate. The exhaust flow meter is attached in series with the vehicle tailpipe, where it is directly exposed to the hot engine exhaust gases. Typical component temperatures in the flow meter are shown in Figure 3.

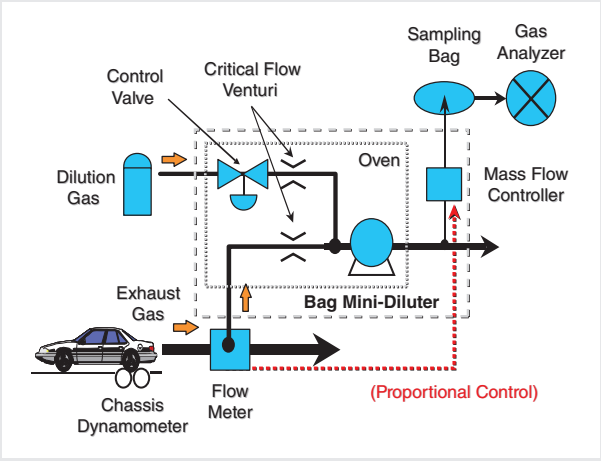

Figure 2 Exhaust flowmeter with Bag Mini-Diluter sampler.

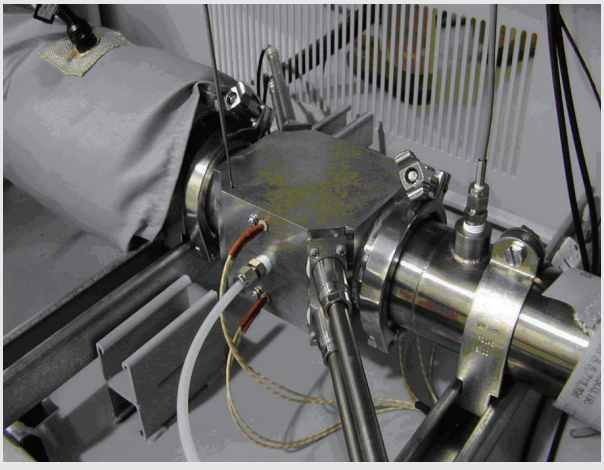

Figure 2b Exhaust Flow meter body, including 400 °C transducers, gas temperature and pressure probes.

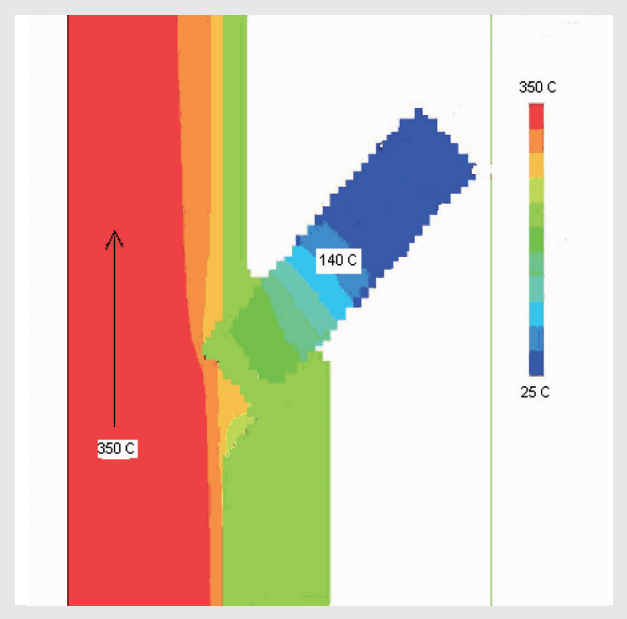

Figure 3 Exhaust Temperature profile for the 400 °C rated ultrasonic transducer. The internal transducer temperature is 141 °C, while the exhaust gas is at 350 °C.

The EXFM-1000 flowmeter is flow calibrated using a NIST traceable calibration system. The accuracy specifications for an Exhaust Flowmeter are <1% at flows greater than 15 scfm, <2% for 5-15 scfm, and <5% for flows less than 5 scfm. The EXFM-1000 has an average flow error of about 0.2% (Figure 4).

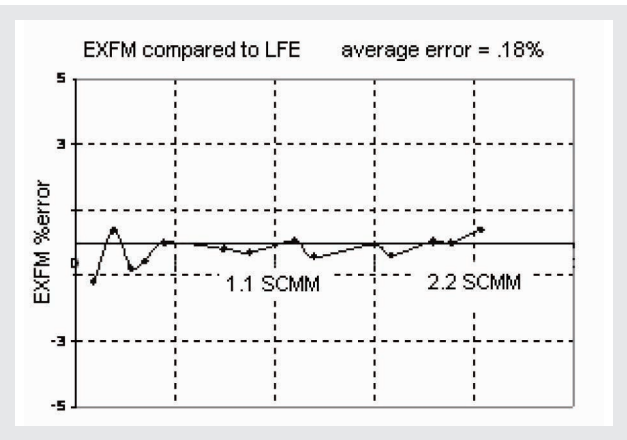

Figure 4 Percent Error plot for the Linear Flow Element (LFE) flow audit. Error limits are <5% error from .1-.15 scmm, <2% error from .15-.5 scmm, and <1% error at flows greater than .5 scmm.

A test vehicle (3.8L V6 gasoline engine) was used to evaluate the Exhaust Flow meter and BMD. The test procedure included an EPA Federal Test Protocol (FTP), followed by a Highway Fuel Economy (HWFE) test and a high-speed (US06) test. The FTP simulates low-speed urban driving. The Highway Fuel Economy test simulates highway driving, and the US06 test simulates aggressive driving and acceleration with speeds up to 85 mph.

Results were evaluated by comparing CO_2 mass emissions in grams per mile between the BMD and a reference CVS for each test. Because tailpipe CO_2 concentration is essentially constant during a test cycle, we can estimate that errors in mass are proportional to errors in total exhaust flow over a test. The EXFM-1000 matched the CVS within 0.5% to 1% for all CO_2 mass emission tests. The maximum exhaust gas temperature for these tests is about 180 °C for the FTP, 280 °C for the HWFE, and 400 °C for the US06 test. This demonstrates that the exhaust flowmeter accurately measures the exhaust volume for a gasoline engine at temperatures up to 400 °C.

Improvement of the Flow Meter

Description of the High Temperature Ultrasonic Transducer

When a heavy duty diesel (HDD) emission is tested, the emissions are measured from not the tail pipe of vehicle but engine directly.

Diesel engine emission tests often result in exhaust gas temperatures greater than the 400 °C possible with the EXFM-1000. The goal for a diesel exhaust flowmeter is to increase the temperature rating to 600 °C. The ultrasonic transducer has been the limiting component, so much of the development effort involves the design of high-temperature transducers.

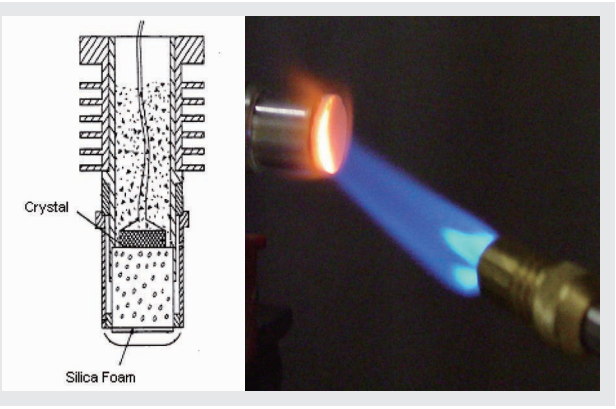

Figure 5 Ceramic high-temperature transducer. The drawing shows the silica foam buffer between the ultrasonic crystal element and the transducer tip. The adjacent picture shows a transducer exposed to gas temperatures of about 1000 °C. The crystal element remained below 250 °C during this test, and the transducer still functioned. However, the signal intensity was reduced even after cooling. Also, we realized the signal processing of the ultrasonic pulse waveform is more difficult than under current temperature range (<400 °C) because of the temperature characteristic of the piezo-electric crystal.

The high-temperature transducer[3, 4] has a silica-foam buffer (Figure 5) between the piezo crystal element and the face of the device. Exceptionally low thermal conductivity maintains the crystal temperature at less than 200 °C while the gas temperature at the face can exceed 600 °C.

This construction technique results in a transducer that maintains the piezo crystal below the Curie point. However, the buffer material also attenuates the ultrasonic signal strength by 20-40 decibels. This means we have an ultrasonic transducer that tolerates high temperatures, but the reduced signal level results in a low signal-to-noise ratio that yields noisy velocity measurements.

Description of the electronic controller for the high-temperature transducer

A high-performance electronic controller (Figure 6) is under development for optimal performance of the ceramic ultrasonic transducers. The controller requires high-speed analog and digital circuitry, including a dedicated digital signal processor. The signal processor is capable of performing 150 million floating point calculations per second, which allows the use of complex noise reduction algorithms. This controller compensates for the increased noise and reduced signal levels observed at high gas temperatures. The ceramic ultrasonic transducers, when combined with this controller results in an exhaust flowmeter that operates at higher temperatures than was previously possible.

Conclusion

An EXFM-1000 has been refitted with the DSP controller and high-temperature ultrasonic transducers. The previously described 3.6L V6 test vehicle validated the new hardware over the 100 °C to 400 °C exhaust temperature range. Preliminary results indicate that the high temperature ultrasonic transducers have extended the exhaust gas temperature rating to 500 °C, where the reduced ultrasonic signal levels limit the measurement accuracy.

Ceramic transducer showed us the possibility of the durability against more than 400 °C.

It is believed that the noisy signal can be significantly improved by applying the digital signal processor. It is expected that the development of improved signal

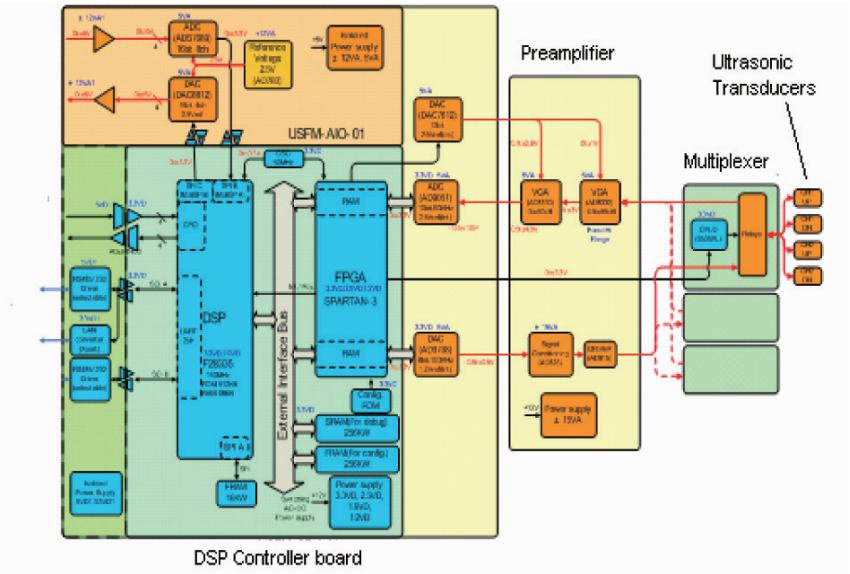

Figure 6 Ultrasonic Controller Diagram

processing algorithms is as necessary to a high temperature flowmeter as the development of the high temperature ultrasonic transducers.

After the upper temperature limit of the flowmeter exceeds 600 °C, it can be applied to diesel engine and emission tests without limitations for engine size or load.

Also, it has a possibility to measure not only vehicle emission but also gasoline engine exhaust directly.

References

[1] T. Nevius, et. al., Transient Vehicle Exhaust Flow Measurement Techniques, SAE paper 2006-01-1360
[2] US patent 7,124,621, Oct 2006, Ultrasonic Flowmeter Calibration, Horiba Instr. Inc.
[3] US patent 7,062,972, July 2003, Acoustic Transducer, Horiba Instr. Inc.
[4] US patent 7,021,145, July 2003, Acoustic Transducer, Horiba Instr. Inc.
[5] ERC Technical Report: The Bag Mini-Diluter Alternative to CVS Sampling, Environmental Research Consortium, May 1, 2000

Masanobu Akita
Application Development Center
Research & Development Division
HORIBA, Ltd.

Tim Nevius
HORIBA Instruments Inc.
Ph. D.

Feature Article

A Novel Instrument for Simultaneous In Situ NOx and O_2 Measurement Applied to Coal-fired Power Plant Applications

Peter A. DeBarber, Hiroshi Mizutani

HORIBA has developed the INM-700, a low cost, low-maintenance, in situ instrument for simultaneously monitoring NOx and O_2 concentrations aimed at industrial applications. The INM-700 is based on a novel use of a solid-state zirconium oxide sensor strategy. Using this new configuration, the instrument eliminates the drawbacks such as sample handling and conditioning and time lags associated with more conventional extractive sampling methods. In this paper, we review the development and testing of the HORIBA INM-700 in preparation for deployment on selective catalytic reduction (SCR) units on coal-fired power plants. We describe the sensor technology developments and modifications implemented to integrate the instrument to the SCR application. We show data to track NOx and O_2 concentrations at a typical power plant and compare that data to conventional extractive methods. The HORIBA INM-700 data tracks plant history data sets and demonstrates this innovative and affordable approach to industrial process monitoring.

INTRODUCTION

The combustion of coal provides more than 50% of the energy needed to generate electricity in the US. One of the unwanted byproducts of coal combustion is nitrogen oxides, NOx. To maintain compliance with Title IV of the Clean Air Act Amendments of 1990 criteria for NOx reduction, most US coal-fired power plants use combustion modification methods and/or SCR NOx reduction systems. For the various combustion modification techniques, the methods rely on NOx monitoring from the CEMS at the stack or in the duct leading to the stack. Such measurements are distant from the combustion process and are frequently a composite reading of multiple units feeding into a single stack. This situation points to a need for an inexpensive, reliable, and accurate in situ unit analyzer.

Such an analyzer would also benefit SCR operations. The SCR process controls emissions of nitrogen oxides through catalytic reduction of NOx by reaction with ammonia, NH_3, to produce nitrogen, N_2, and water, H_2O. In general, the SCR consists of a reactor chamber with a catalyst bed, and an ammonia handling and injection system. The ammonia is injected into the flue gas upstream of the catalyst. In commercial operations, SCR systems provide reductions in NOx emissions on the order of 90%. More efficient management and use of SCR systems may be enabled using in situ NOx monitors at the inlet and outlet to the catalytic beds. The real time NOx data may be used to better control the ammonia injection over the beds and also allow better catalyst health management. Most existing SCR systems on coal-fired units operating in the US make use of a limited number of NOx measurement points using extractive sampling probes mated to chemiluminescence analyzers. The limited number of sampling points often will not provide an accurate measurement of SCR inlet and outlet NOx levels since stratification or spatial variations of NOx within the SCR are not accounted for. The relatively lower cost of the INM-700 in situ analyzer makes deployment of multiple sampling points economical. This will lead to improvements in SCR operation by striking a tighter balance between minimizing NH_3 slip and reducing NOx emissions. At the same time, planned unit outages for catalyst maintenance activities may be better managed by monitoring in real time catalyst health.

In the remainder of this paper we discuss the development of the INM-700 in situ NOx and O_2 analyzer and its

application to SCRs. We first describe the theory behind the zirconium oxide sensor. Then we discuss field testing on an SCR at a major coal-fired plant in the US. Finally we present a few concluding remarks.

THEORY: ZIRCONIUM OXIDE NOx SENSOR

At the heart of the INM-700 is a sensor technology based on zirconium oxide, ZrO_2. This sensing strategy is an adaptation of an analogous measurement strategy used for automotive applications. In general, the ZrO_2 for sensor applications is typically processed as a zirconia-ceramic. The ceramic can have various transition metals added to enhance certain characteristics. One property that enables ceramic ZrO_2 to be used as a sensor is its porosity to oxygen ions and other molecules at temperatures above 650 °C. As we show shortly, an O_2 sensor takes advantage of this porosity. The sensor is basically an electrochemical cell and is constructed by applying a thin film of porous platinum, Pt, to two opposing surfaces of a ZrO_2 ceramic. This element divides the reference side of the cell from the sample side. The Pt films serve as the electrodes and the heated ZrO_2 serves as the electrolyte. Differences in

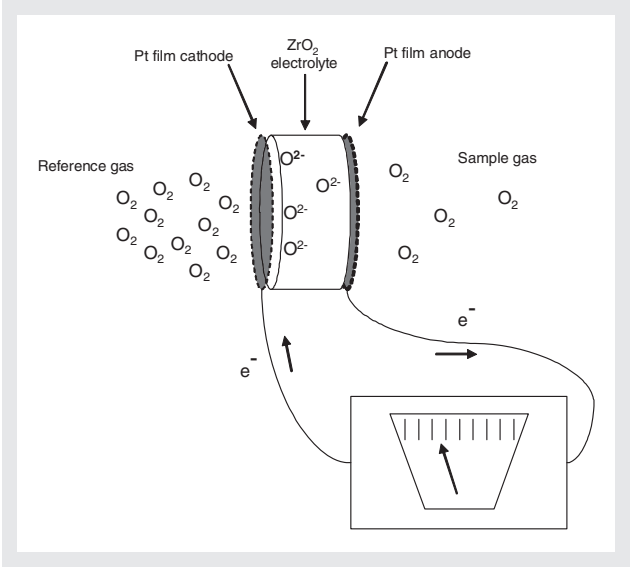

Figure 1 The zirconium oxide sensor operates as an electrochemical cell.

the partial pressure of O_2 from one side of the electrochemical cell to the other create an electromotive force. Oxygen ions, O^{2-} are able to migrate across the ZrO_2 electrolyte in a direction to restore the potential equilibrium. As long as there is a difference in the partial pressures between the reference and sample sides of the electrochemical cell, ions will migrate, and current will flow. This is illustrated in Figure 1. The electromotive force to restore the imbalance may be used to yield an accurate measurement of the partial pressure difference between the reference and sample. Knowledge of the partial pressure within the reference gas allows calculation of the partial pressure in the sample gas.

HORIBA scientists and engineers have taken this technology a step further by incorporating a novel zirconium oxide sensor into an analyzer that is capable of simultaneously measuring O_2 and NOx. This sensing approach was first developed by HORIBA's Engine Measurement Division for their MEXA-720NOx product. The MEXA-720NOx is a direct-installation gas analyzer for real-time, on-board vehicle emissions. It is used to measures NOx and air fuel ratios in engine exhausts. HORIBA has now adapted this sensor for industrial applications in the INM-700 product (Figure 2).

Figure 2 HORIBA's INM-700 for simultaneous NOx and O_2 industrial process applications.

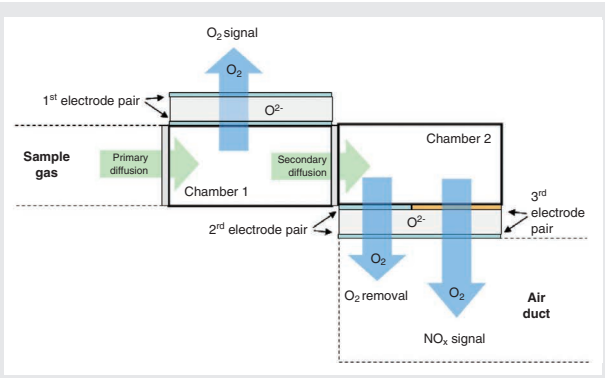

Figure 3 The two chambers of a zirconium oxide sensor may be configured for simultaneously measuring NOx and O_2.

The underlying idea behind the sensor used in the INM-700 is schematically shown in Figure 3. The sensor is comprised of an internal heater, and two internal chambers. The chambers house three pairs of electrodes: one electrode pair in the first chamber and two electrode pairs in the second chamber. Sample gas enters the first chamber through a primary diffusion element. Within the first chamber, a Pt electrode pair is used as an

electrochemical pump to reduce oxygen levels in the sampled gas to below 10 ppm and yield a measurement of the oxygen concentration in the sampled gas. The oxygen depleted sample gas then diffuses into the second chamber. Within the second chamber, oxygen levels are further lowered to less than 0.01 ppm by a second oxygen pumping Pt electrode pair. This also provides a feedback signal of the oxygen levels to the electrochemical pump in the first chamber to effect consistent pumping conditions with respect to the changing ambient and reference oxygen levels. The third electrode pair made of Rh is used to infer the NOx concentration from the oxygen signal. The oxygen signal is generated as a result of the electrochemical reduction of NO in the sampled gas.

TESTING ON SCRs

Tests were conducted on the inlets and outlets of SCRs on 200 MW coal-fired units. Stream temperatures approached 370 °C. These locations are ideal for the in situ NOx analyzer for controlling the rate and distribution of the injected ammonia over the catalyst bed. For initial testing only single probes were placed at the inlet and outlet to the SCR. Subsequent field testing (ongoing) uses four INM-700 analyzers installed on the inlet and four INM-700 analyzers on the outlet. Such multiple probe configurations ensure adequate spatial coverage for control purposes as well as catalyst health monitoring.

Figure 4 shows the mounting locations for two of the INM-700 probes. The analyzer control boxes were located approximately 10 meters away. In practice, the control units may be located up to 50 meters from the probes. The probes were mounted adjacent to the existing extractive sampling chemiluminescence analyzer (CLA) and paramagnetic (PM) oxygen analyzer ports. The INM-700 probes were separated from the CLA by approximately 2 meters. This separation caused some bias between observed INM-700 and CLA values and is a result of stratification within the flow stream. In the next section we show a typical data trace.

RESULTS AND DISCUSSION

The power plant data traces of Figure 5 show the plant output was operating at approximately 150 MW. The NOx measurements from the INM-700 and the plant's chemiluminescence analyzer are indicated as ppm, and

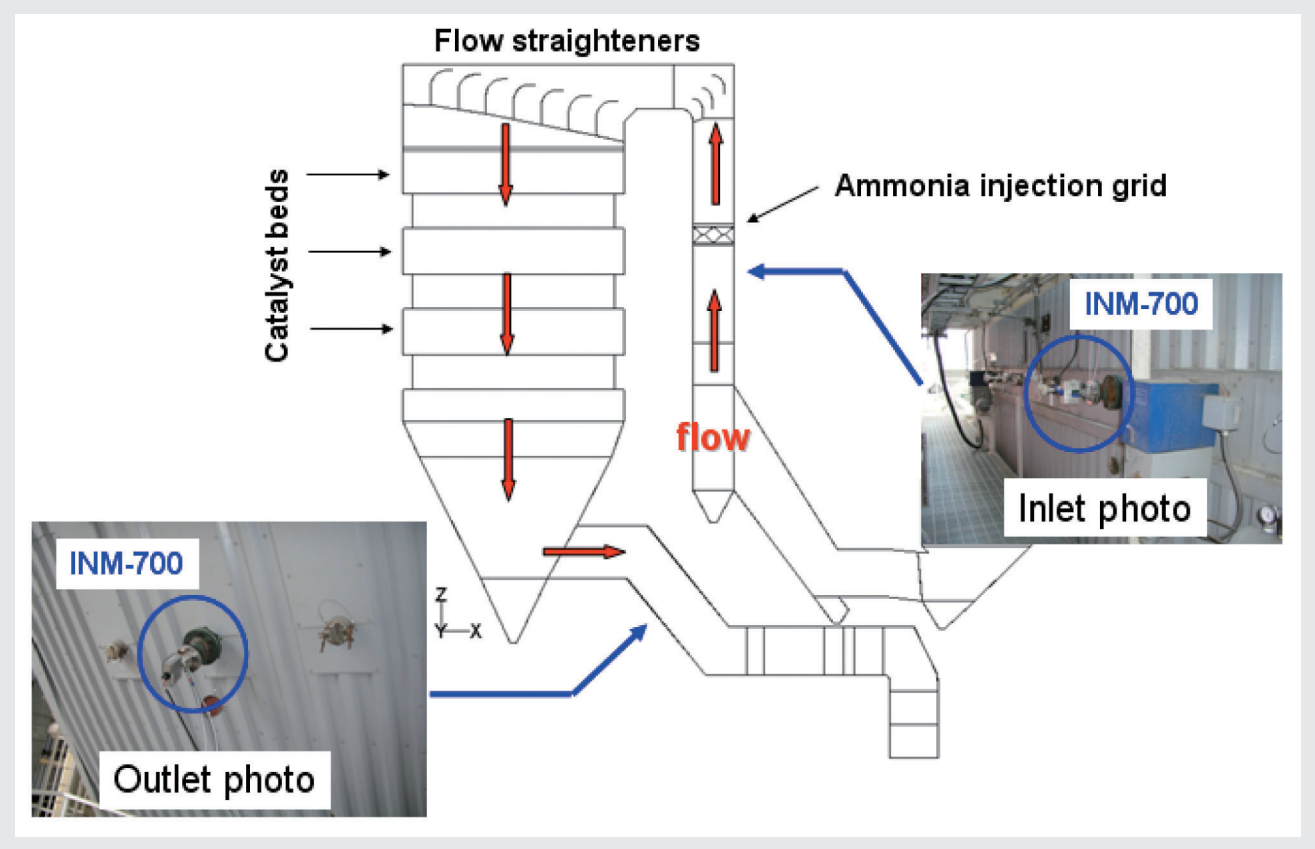

Figure 4 Simple installation and placement of the INM-700. The simplicity of the INM-700 contributes to low installation and maintenance costs.

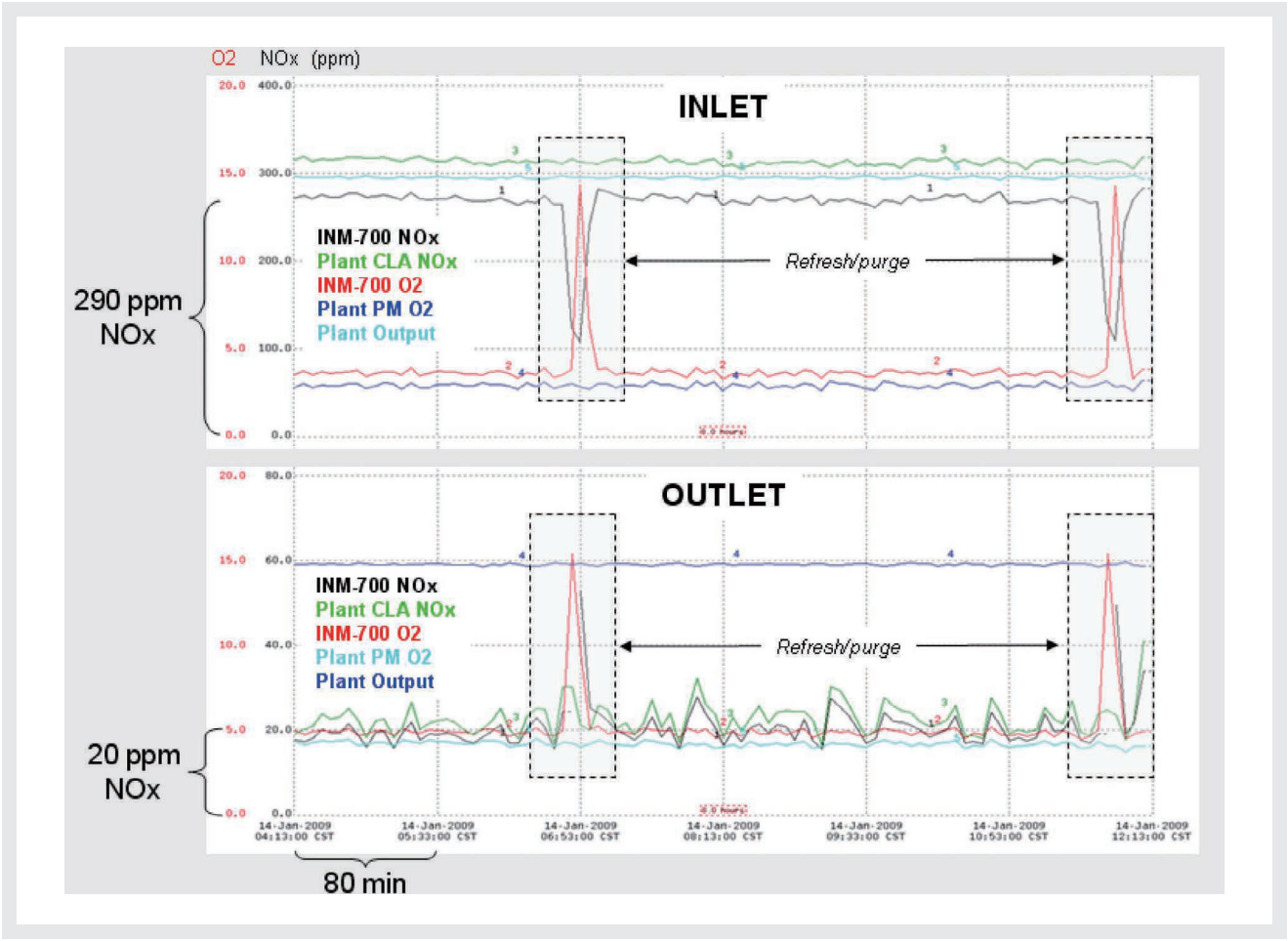

Figure 5 Data traces comparing inlet SCR measurements to outlet measurements.

the O_2 measurements from the INM-700 and the plants O_2 analyzer are labeled as percent. The data is presented as a function of time with 80 minutes between major divisions on the graph. The top half of the graph shows the data for the inlet measurements and the bottom half of the graph shows the data for the outlet. In both panels, the HORIBA INM-700 analyzers closely track the plant's NOx and O_2 analyzers. The slight offset bias observed between the INM-700 and the CLA is due to stratification within the flow. The NOx data for the inlet indicates that NOx levels were steady at 290 ppm. After SCR treatment, at the outlet, the data shows that NOx has been considerably reduced to 20 ppm. Such data show that this SCR was operating at 90% efficiency.

The regions of data outlined by the dashed boxes show INM-700 operation during sensor refresh/purge periods. The sensor refresh/purge mode is a feature that increases sensor stability and longevity. Periodically a high voltage is applied to the sensor element that aids desorption of any contaminants that may rest on the surface of the sensor. After the refresh voltage, the sensor is purged using instrument air. The purge air removes the desorbed contaminants. The frequency and period of the refresh/purge cycle is on the order of 5 hours for approximately 10 minutes. In practice, the frequency is increased as the sensor ages. For example, a new sensor may only need a refresh/purge cycle every 12 hours. An older sensor may require refresh/purge twice as often.

In addition to data recorded during SCR operation, we also used x-ray fluorescence to analyze the accumulated dust and fly ash both inside and outside the probe tip (see Figure 6). Our initial concerns were related to the formation of NH_4SO_4 ammonium bisulfate (ABS) on the sensor. Figure 6 shows the results of this analysis. The samples were mostly two types of particles: a lighter colored, 200 micron-sized (average) particle predominantly consisting of oxygen, aluminum, and silicon and a darker, 300 micron particle of mostly carbon. Both these particles are characteristic of normal fly ash and unburned coal particles. Based on the x-ray fluorescence spectra, there was no evidence of ABS formation on and within the probe. Regardless, a redesign of the probe tip has now eliminated the possibility of dust and ash accumulating inside the probe tip.

To access the relative health of a used zirconium oxide

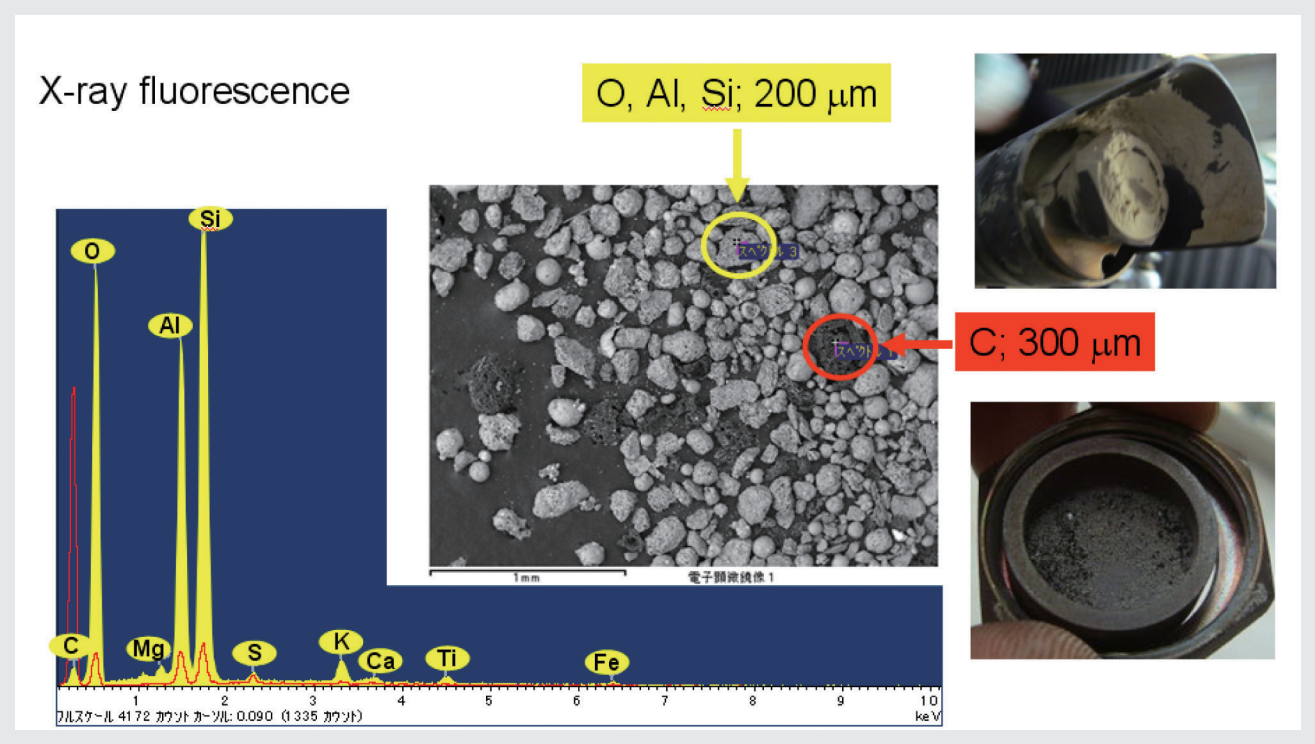

Figure 6 X-ray fluorescence analysis of dust and fly ash on and in the probe tip indicated no ammonium bisulfate formation.

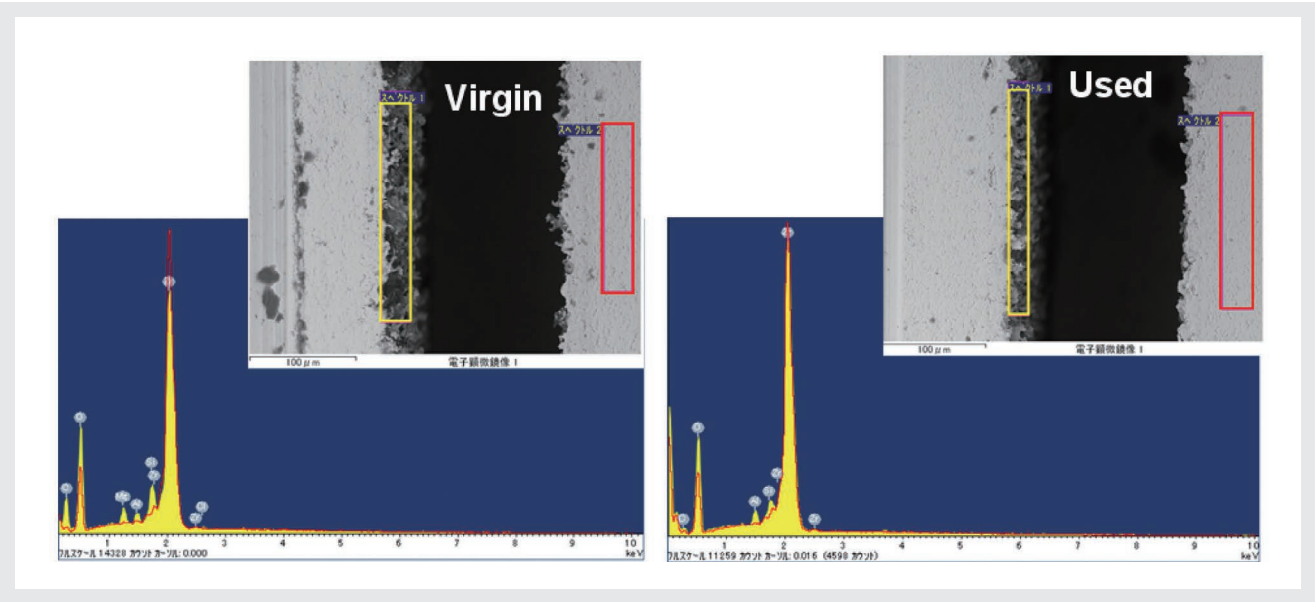

Figure 7 Comparison x-ray fluorescence analysis between a one year old sensor and a virgin, unused sensor. There was no significant contamination observed on the used sensor.

sensor, we also recorded x-ray fluorescence spectra of a sensor that had been in operation for one year and a fresh, unused (virgin) sensor. Figure 7 shows the results of this comparison analysis. The results indicated no significant contaminants on the used sensor.

CONCLUSIONS

This paper reviewed the general operating principles behind zirconia-ceramic based sensors and introduced a new approach for the in situ, simultaneous measurement of NOx and O_2. The benefits of this new approach are in the area of improved time response and lower life cycle

costs in comparison to existing extractive sampling methods. The zirconium oxide sensor technology is well-established and reliable. The refresh feature of the analyzer ensures steady and accurate data. Test results on a 200 MW coal-fired power plant on an operating SCR inlet and outlet were presented and demonstrate viability for this application. The real-time measurements verified that the SCR catalyst was performing to specification of 90% NOx reduction. Post test analysis on dust and fly ash indicated no problems with ABS or sensor contamination. Field tests continue on an ammonia injection grid controls project. Preliminary results look promising. For more up to date information, please contact the authors.

ACKNOWLEDGMENTS

The authors wish to thank many individuals including fellow Horibarians, Dick Bates, Shigeyuki Hokamura, Dave Horstman, and Satoshi Inoue.

References

[1] Institute of Clean Air Companies, White Paper Report "Selective Catalytic Reduction (SCR) Control of NOx Emissions from Fossil Fuel-fired Electric Poer Plants," May 2009.

[2] A. Kunimoto, Y. Yan; Yongtie, M. Hasei, H. Kurosawa, Y. Nakanouchi; Yukio, NOx Sensor, US Patent 6126902, October 2000.

Peter A. DeBarber
Business Development
Process & Environmental
HORIBA Instruments, Inc.
Ph.D.

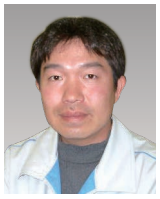

Hiroshi Mizutani
Quality Management Center
HORIBA, Ltd.

Feature Article

Building a Primary Mass Flow Standard, "PMFS"

Dan Mudd, Koji Imamura, Bill White, Alex Kramer

This paper recounts the evolution of a design for a primary mass flow standard (PMFS) targeted at measuring flows down to the 0.0012 grams per minute[*1] level of gas with a target accuracy of 0.1% of reading. It describes the basic concept of direct mass-flow measurement, identifies external factors that can corrupt the mass measurement and recounts system-design revisions intended to reduce the corrupting influences. A formal uncertainty analysis of the PMFS is not presented as the project is still evolving. However the core task of achieving the needed PMFS stability and noise levels at low-flow levels is discussed for a series of four evolving prototypes, each showing continuing performance improvements.

*1: 0.0012 Grams per minute is equals 1 standard cubic centimeter, 1 sccm, of N_2. A sccm is a mass flow term equal to one cubic centimeter per minute of a gas at 0 °C and 1 atm.

Introduction

Why Mass Flow Measurement?

Mass flow measurement is an enabling technology at the base of many industries from solar cell fabrication to process control in refineries. Critical industrial processes often involve chemical and physical reactions that require specific and repeatable amounts and/or ratios of different gas species to be present for proper reactions to occur.

HORIBA's Reno facility is the U.S. flow metrology center for measuring the mass flows of gases used in semiconductor fabrication. These mass-flow measurements are used to characterize and validate product designs and calibration practices of the Mass Flow Controller products of HORIBA's Semiconductor Division. The PMFS provides a primary standard for these mass flow measurements, augmenting Reno's existing transfer standards[*2]. The target mass-flow measurement range for this first PMFS is 1 standard cubic centimeter per minute, "1 sccm", to 3,000 sccm on N_2.

*2: The main transfer standard used is a rate of pressure rise system, dP/dt, based on the ideal gas law, modified for non-ideal gas behaviors. This system has been successfully running process gases for 15 years.

Basic Concept of the PMFS

The basic approach to direct mass-flow measurement is illustrated in Zone #1 of Figure 1 below. An electronic balance, "a scale", is used to measure the force of the pull of gravity on the mass of a cylinder containing a gas. As gas is removed from the cylinder, the force on the scale reduces. By recording the scale readings over time, one can directly measure the mass flow rate out of the cylinder.

Corrupting Forces

This direct mass flow rate measurement approach is simple theoretically; however, successful implementation of the simple theory requires isolating the changing weight signal of gas leaving the scale from other corrupting forces and complicating factors that can mask the flow-induced changing weight signal. Specific details on these factors are described below.

- Corrupting factor #1: Helium balloons are not the only things that try to float.

  The buoyancy force on an object roughly equals the weight of the air an object displaces. A closed 1 liter

cylinder has a nominal 1.2 grams buoyancy force. At the target 1 sccm N_2 flow, the PMFS will need a stability of 0.0000012 grams per minute. Buoyancy force fluctuations from natural atmospheric changes dwarf this need.

- Complicating factor #2: Scale Resolution.

Compared to the cylinders and tubing needed to contain a gas, 1 scc of gas does not weigh much. Scale resolution becomes increasingly coarser, as a percent of full scale, as the size of the scale increases to accommodate gas-containment hardware.

- Complicating factor #3: Gravity is not the same magnitude at all locations.

Scales measure force, not mass. The force measured by a scale is the product of the local gravity and the mass on the scale. The gravity is a function of location and elevation. Reno's elevation, the location of the PFMS, is at 1500 meter above sea level and gravity is roughly 0.03% less than most locations.

- Corrupting factor #4: Electrostatic forces.

Initially, a non-electrically conductive cover was used with a prototype PMFS system. If rubbed, a static charge would build up and exert forces on the items on the scale. Over time, this force diminished as the charge dissipated.

Off-Scale Volumes

In addition to addressing the complicating factors that can corrupt the weight measurement from the scale, one must also realize that some portion of the plumbing delivering the gas from the on-scale cylinder to a device being calibrated will be off of the scale. This "off-scale" volume can induce flow errors unless properly addressed.

The prototypes described in this paper use an on-scale cylinder to feed gas to the off-scale plumbing[*3] associated with a Device-Under-Test, "DUT" via a flexible 1/32" I.D. tube as shown in Figure 1. With this configuration, the scale directly senses the mass (M1) in the cylinder (Zone 1), partially senses the mass (M2) in the 1/32" ID tubing (Zone 2) and does not sense the mass (M3) in the off-scale volume (Zone 3). Accordingly, the scale can be used to directly measure the mass flow ($\dot{m}_1$) leaving the cylinder; however the mass flow through the DUT ($\dot{m}_3$) will be different than m_1 if the mass in volumes 2 and 3 change with time. The following describes the mechanisms that can cause the mass in these volumes to change and discusses countermeasures to minimize their effect on the accuracy of the DUT measurement.

*3: Fittings, pressure transducers, valving and the DUT's own internal volume.

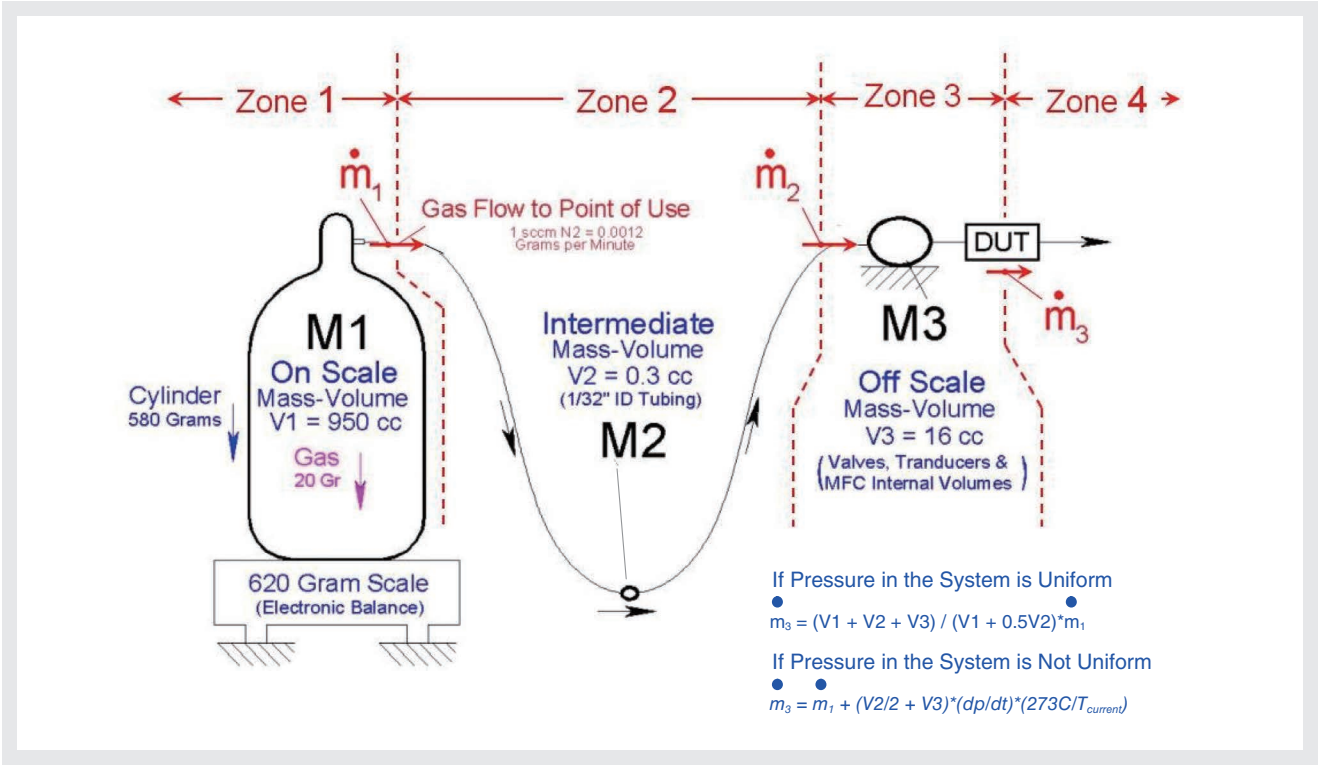

Figure 1 The Basic PMFS Concept and the Effect of Off-Scale Volumes

If one makes the simplifying assumption that pressure in the total system, V1, V2 and V3 from Figure 1 is uniform[*4], then the percentage of the total system mass that is in each volume is proportional to the volume of each V1, V2 and V3 and is independent of the system pressure. If so, the flow through the DUT ($\dot{m}_3$) will draw mass evenly from both the on-scale and off-scale volumes. Accordingly, the flow based solely on the readings from the scale ($\dot{m}_1$) will understate the flow through the DUT ($\dot{m}_3$) by the ratio of the on-scale volume to the total system volume. The relationship is roughly:

$\dot{m}_3 = (V1 + V2 + V3) / (V1 + 0.5V2)*\dot{m}_1$
For the Figure 1 Configuration, this represents a 1.7% understatement.

$\dot{m}_3 = (950 + 0.3 + 16) / (950 + 0.3/2)*\dot{m}_1 = 1.017\ \dot{m}_1$

*4: This assumption is practical for small flows. For larger flows, pressure drop through the tube becomes significant and the assumption becomes invalid.

Countermeasures and discussion

1. Minimize the off-scale volume by component selection and placement of the DUT.
   - This directly reduces the magnitude of the needed correction to the $\dot{m}_1$ flow.
2. Determine the on-scale and off-scale volumes and apply a fixed correction to $\dot{m}_1$ to determine $\dot{m}_3$ as shown above.
   - This fixed correction induces errors as the pressure drop in the tube becomes sufficient to affect the uniform pressure in the system assumption.
3. Measure the pressure in the off-scale volume and utilize the ideal gas law to calculate the mass being drawn from the off-scale volume and add it to the on scale flow, $\dot{m}_1$. An application of this correction is summarized below.

i.e.: $\dot{m}_3 = \dot{m}_1 + (V2/2+V3)* (dp/dt)* (273C/T_{current})$

The PMFS of this paper is instrumented to employ this correction. If the error of the correction is limited to 2% of reading[*5] when correcting the ~1.7% off-scale volume effect, the net induced total-system error would be 2.0%*1.7% = 0.034% roughly.

4. Install a regulator on the outlet of the on-scale cylinder to keep the pressure in the off-scale volume at a near constant pressure for steady state flows.

   - If the regulator performs ideally, and provided a constant outlet pressure, the off-scale volume effect would be totally eliminated. However, regulators are not perfect and the outlet pressure of regulators will creep up as the supply pressure to the regulator decreases as gas is removed from the on-scale cylinder source. This effect is illustrated in Figure 2. The addition of the regulator reduces the off-scale volume effect by a factor of 70. Figure 2A below illustrates the real world performance of the regulator on the prototype.
     - After flow begins, the outlet pressure from the regulator to the DUT creeps up 1 psi for every 70 PSI the cylinder pressure supplying the regulator drops.
     - When the cylinder pressure reaches the regulator outlet setting, the regulator can no longer control its outlet pressure and the pressure to the DUT drops rapidly with the cylinder pressure.

   - The improvement of adding a regulator can be combined with the correction method of item #3, to further reduce the magnitude of the effect. Figure 2B shows the scale flow, $\dot{m}_1$, and the DUT flow, $\dot{m}_3$ ($\dot{m}_1$ + ideal gas law correction) over the period when the on-scale cylinder pressure starts to drop to the regulator outlet pressure setting, time = 212 minutes, and the regulator looses it's capability to maintain a constant pressure in the off scale volumes. As can be seen the constant flow through the DUT is reflected by the m1 flow + the dP/dt correction.

*5: This 2%R error estimate is 4 times larger than our experience with our current rate of rise systems currently operate at the Reno facility.

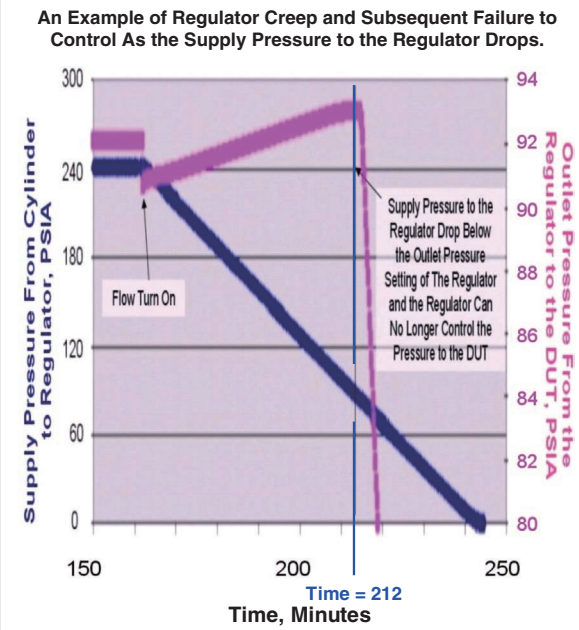

Figure 2 Regulator Creep, Its Effect On the Flow Calculation and a Correction Method

Prior Art

The authors are aware of three previous PMFS systems and two related mass measurement devices. The first was a Unit Instruments effort in the 90's. This system was a simple cylinder on scale system that addressed the corrupting force issues discussed above by taking the required time needed for the totalized gas mass that leaves the scale to grow sufficiently large, relative to the corrupting forces, to allow the system attain the desired accuracy. Unfortunately this approach requires long time periods to achieve accuracy for low flows. The Unit system reportedly required 6 months for a flow measurement at 1 sccm N_2.

In the late 90's a PMFS was built at the Oak Ridge National Laboratory, ORNL. It consisted of a ridged large chamber, suspended from a wire attached to a scale, while floating at slightly negative buoyancy in a large water bath. Gas from a DUT would flow into the chamber increasing the weight sensed by the scale. This "submarine" approach addressed the effects of changing air density and allowed a small scale with higher resolution to be used.

In the last 4 years the authors became aware of a PMFS commercially offered[*6] by DH Instruments. Like the previous Unit Instrument effort, it also consisted of a cylinder-on-scale configuration, but it utilized lighter components and took measurements to determine air density and numerically compensated for the sensed buoyancy effect. The speed of this system at lower flow was markedly faster than it predecessor. Customers indicate a 10 sccm flow reading can be taken in 10 hours.

During the early phase of this Horiba effort, the authors searched for the highest resolution electronic balance capable of a 1 kg payload. They found a class of scales called mass comparators. One version commercially offered[*7] by Mettler Corporation weighs an object placed in a vacuum chamber to negate the effect of changing buoyancy forces corrupting the weight measurement.

*6: The price for the DHI system plus associated instrumentation approaches $250,000.

*7: The price for the Mettler system plus associated instrumentation was $500,000.

The HORIBA Effort

Four prototypes were built during HORIBA's PMFS effort. Each subsequent prototype benefited from the performance lessons learned from its predecessors. Figure 3 illustrates the four prototypes along with their concept and performance results.

The authors' first prototype was chosen based on the perceived successes of the Oak Ridge PMFS. A prototype, built utilizing the "submarine" approach, consisted of a cylinder suspended in water by a wire hung from a scale. The intent of the prototype was take a preliminary look at the external forces influencing the

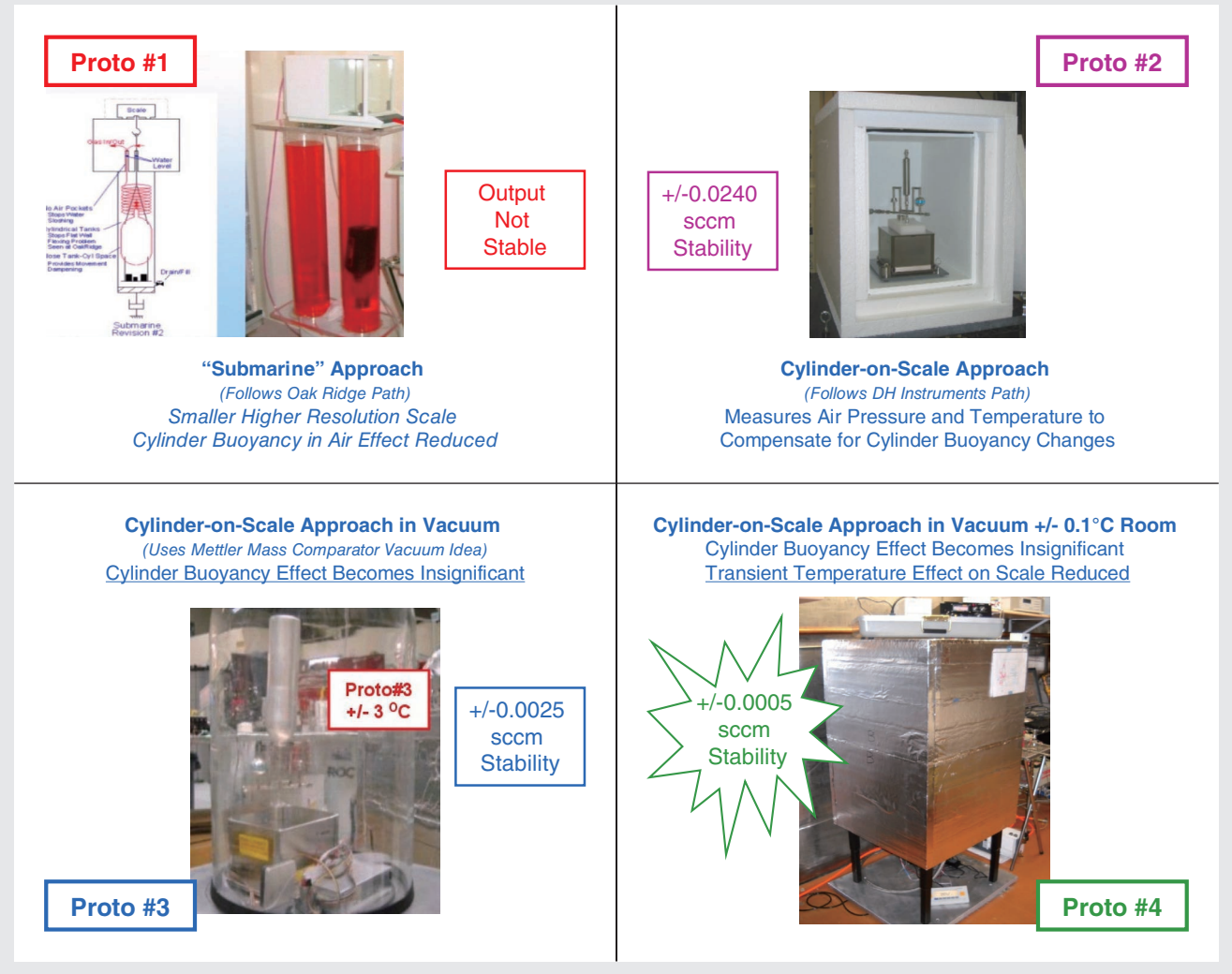

Figure 3

scales zero reading under a no-flow condition rather than to actual measure flow.

From prototype #1 the following was observed.

- Ambient temperature greatly influenced the zero of an unloaded scale.
- Placing the scale in a +/- 0.1 °C temperature-controlled room helped but did not reduce the noise to an acceptable level. It never achieved stability in a multi-day run.
- Corrosion products[*8] developed on the aluminum tank prototype, changing its effective volume and changing the buoyancy force.
- Antifreeze for aluminum engines was added to the water as a counter measure for the corrosion issue:
- The density of the fluid increased requiring additional ballast to be added to tare the increased buoyancy. As the water in the antifreeze mix evaporated, the density of the remaining fluid increased changing the buoyancy force.

These initial difficulties, combined with an aversion to the task of maintaining a wet system, pushed the authors into investigating the next approach before pushing further to refine the submarine approach.

The second HORIBA prototype followed the DH Instrument's cylinder-on-scale configuration. The PMFS operated with two different cylinder sizes, a 950 cc and a 50 cc cylinder.

*8: Or some other undefined phenomenon.

From prototype #2 the following was observed.

- The system with the 1 liter cylinder displayed a +/- 0.0240

sccm equivalent flow window over the 6 day test.
- The smaller 50[*9] cc cylinder displayed a +/- 0.0025 equivalent flow window over the same period. Unfortunately, using the smaller 50 cc cylinder reduced the higher flow capability more than the authors' desired.
- Numerical corrections for the external forces using pressure, temperature and relative humidity measurements removed roughly half the effect of the external forces.
- Numeric efforts which adding the time-based derivative of the temperature signal were more effective.

Prototype #2's early results, +/-0.0240 sccm N2 equivalent, while promising, were still markedly above the evolved target of 0.0005 effective sccm N_2 flow noise. The authors choose to abandon the DH Instrument's approach of sensing and numerically compensating for changing air density affecting the buoyancy force. Rather for Prototype #3, the authors followed the Mettler mass comparator's direct, brute force method of removing the atmosphere around the system to eliminate corrupting buoyancy effect.

Prototype #3 placed the hardware of prototype #2 in a bell jar equipped with a turbo-molecular pump to maintain a 1 Pa vacuum around the system. A metal skinned foam housing was added to provide insulation, electrical grounding and IR shielding to buffer the system from ambient temperature changes and prevent electrostatic charge build up.

*9: The better stability numbers for the smaller cylinder did suggest that buoyancy forces were still significant.

From prototype #3 the following was observed.

- The system with the 1 liter cylinder displayed a +/- 0.0025 sccm flow window over the 8 day test, a 10X improvement over the prototype #2 performance.
- The remaining flow variation correlated roughly with laboratory temperature.

The rough correlation between the flow variation and temperature can bee seen in Figure 4; however a numeric correction for a short data run did not seem practical. In addition, another 5X reduction in flow variation was needed to meet the initial target of 0.1% accuracy at 1 sccm N2 flow. To reduce the temperature induced effect, prototype #4 was placed in a used transoceanic shipping container modified to control temperature to +/- 0.1 degree C.

Prototype #4 was operated in two different configurations. In the first configuration, the PMFS has no cylinder installed and there was no mass flow, just a 10 gram weight. In the second case the 1 liter cylinder is installed and a flow rate of roughly 0.11 sccm is being consumed by a DUT.

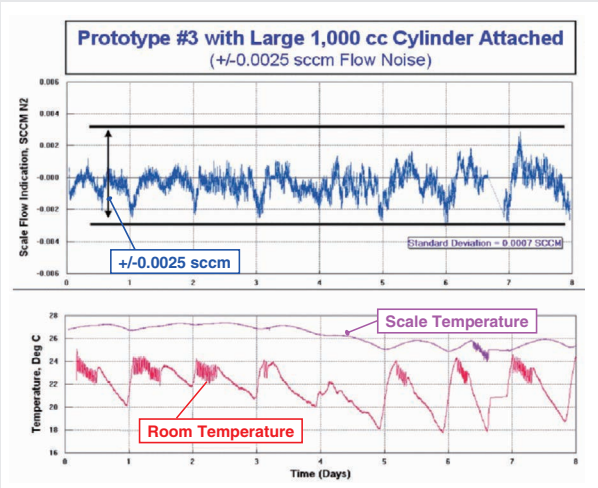

Figure 4

From prototype #4 the following was observed. See Figure 5.

- In both cases, (1) with a 1 liter tank and 0.11 sccm flow to a DUT and (2) without tank and no flow, the PMFS flow window was on the order of +/- 0.0005 sccm and no baseline trend was observed.
- In addition, the period of the flow indication's "wandering" in both cases appears similar.

The act of placing the PMFS in a vacuum and in a +/-0.1 C environment appears to have achieved the target 0.0005 sccm noise level[*10]. At this point the author's moved away from the task of reducing external noise and moved on to

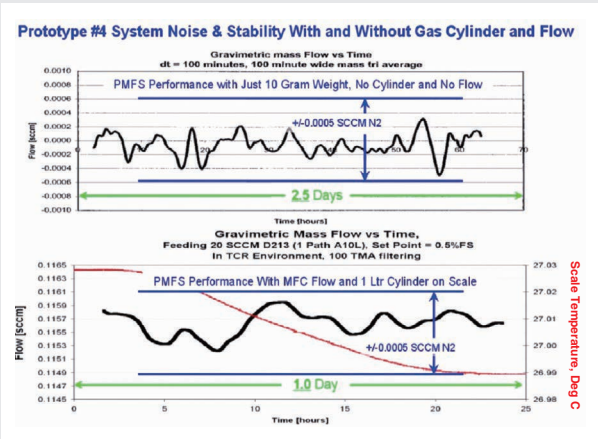

Figure 5

quantifying the off-scale volume's performance at higher flow rates and NIST traceability.

*10: Based on the similar operating results, noise magnitude and period of wandering, with and without a cylinder attached to the scale, the authors concluded that that the residual noise was not buoyancy related and ended the effort to further reduce this external force.

NIST Traceability

The primary path back to NIST for this PMFS is through a 0.5 gram OIML class E1 and a 10 gram OIML class E 2 weight. These weights are serialized and traceable back to NIST. A second set of weights are installed on small robot arms in the vacuum chamber of prototype #4. These "working" weights can be remotely hung on and removed from the gas cylinder to periodically check the scale's calibration. See Figure 6.

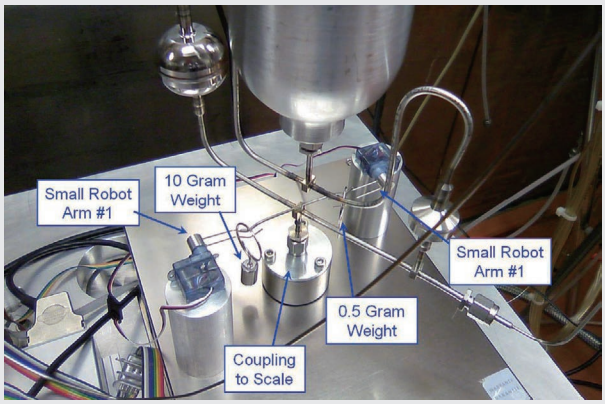

Figure 6

Information on the scale's span and zero stability can be inferred from repeatedly placing a weight on and off the cylinder attached to the scale. Figure 8 below illustrates the scale output for the load-unload cycles continuously performed over 18 hours during system cool down after initial evacuation pumping[*11].

Selecting the cool-down period after initial system pump was intentionally chosen to be illustrative of the effect of temperature on the scale's span and zero. It can be seen that the zero of the scale is affected by the temperature transient; however, the span of the scale is not so affected. During-steady state operation the scale's temperature gradients is on the order of 0.01 °C per hour within a fixed band of 0.1 degree C maintained in the shipping container. This steady-state operation temperature transient, 0.01 °C per hour, is 70 times more stable that seen in Figure 7 and is sufficient to maintain a stable scale zero.

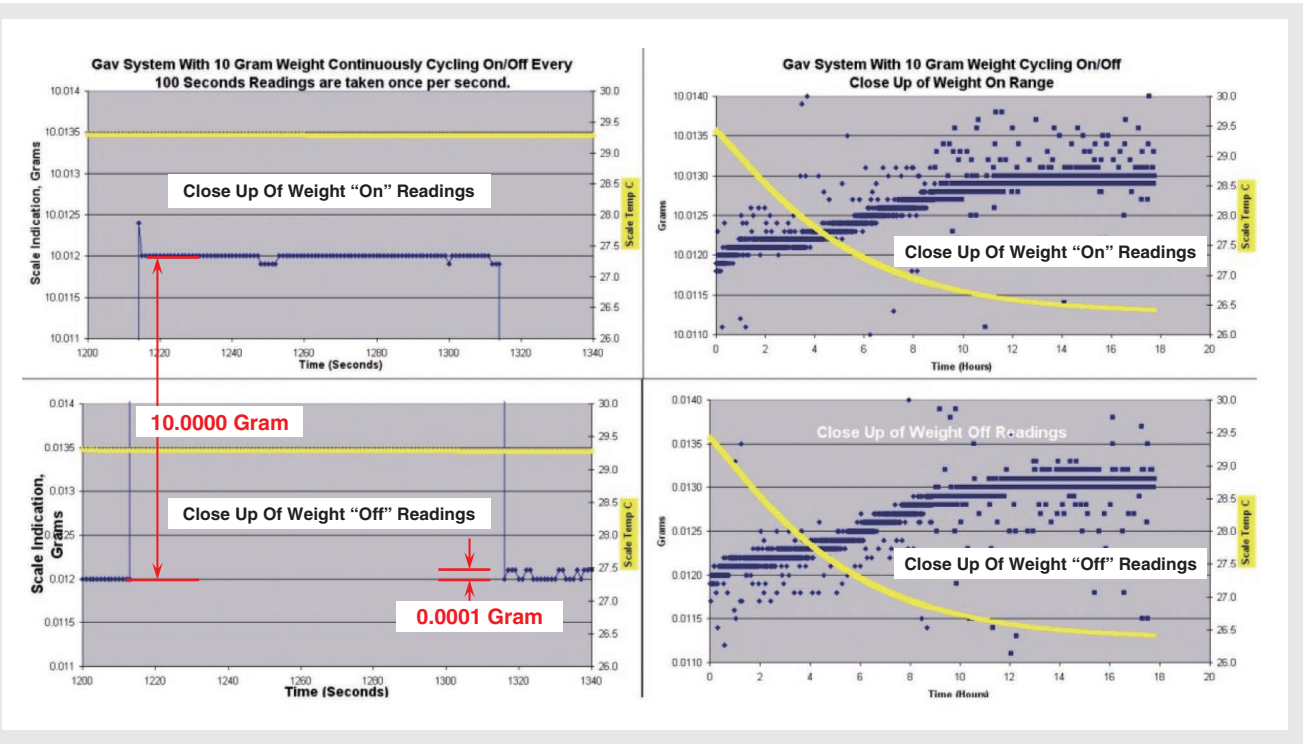

Figure 7

*11: During system evacuation a turbo-molecular pump mounted directly on the aluminum base plate of the system is powered adding heat to the system. After an acceptable vacuum is reached this pump is turned off and a remote pump is used to maintain the desired vacuum level. The system then cools to a lower steady-state temperature.

Conclusion

The final prototype Primary Mass-Flow Standard appear to be practical to measure flows near 1 sccm in a 100 minute data run. From our evolving series of PMFS prototypes, we found the insulated vacuum chamber placed in a temperature controlled shipping container allowed us to reduce external noise on the system to a window of +/- 0.0005 sccm. We believe this level is adequate to support the lowest flow levels currently used in the semiconductor and related industries.

After exploring and validating the system performance for the upper-flow limits[*12] of this PMFS, estimated to be roughly 3,000 sccm, the authors will begin a 2nd PMFS targeted at measuring flows up to 200,000 sccm. It is anticipated that developing countermeasures to address momentum and thrust issues from the higher flow rates will be the primary technical challenge in the next device.

*12: Clock timing validation will become more important and quantification efforts will be required on time measurement.

Dan Mudd
Vice President, Advanced Technology
HORIBA/STEC Inc.

Koji Imamura
R&D Dept. Fundamental Technology Team
HORIBA/STEC Inc.

Bill White
Director, Advanced Technology
HORIBA/STEC Inc.

Alex Kramer
Product R&D Engineer
HORIBA/STEC Inc.

Feature Article

Measurement Modalities of the HORIBA Medical ABX Pentra DX120 Hematology System

Jim Knowles, Terry K. Johnson

The HORIBA Medical ABX Pentra DX120 is a complete hematology platform featuring Complete Blood Count (CBC), Nucleated Red Blood Cell (NRBC) count, and Reticulocyte (Retic) count at an approximate throughput of 120 CBC samples per hour. Multiple measurement modalities are used by the system including cell counting by electronic impedance variation, hemoglobin measurement by absorbance spectrophotometry, White Blood Cell (WBC) population differential by optical light scatter and impedance measurements, and measurement of Reticulocytes and NRBC using thiazole orange stain and orthogonal fluorescence with an argon laser.

ELECTRONIC IMPEDANCE VARIATION

The Red Blood Cells (RBC), WBC, and Platelets are measured by electronic impedance.

Cells passing through an aperture create resistance (impedance) when they are suspended in an electrolytic diluent between two electrodes and a voltage potential.

The voltage change measured as a cell passes through the aperture is proportional to the size of the cell. Since the current is constant and remains unchanged, the larger the cell, the more resistance it creates.

The individual voltage pulses generated by cells passing through the aperture are amplified, channeled according to size and threshold, and then mathematically integrated to give final numeric values for the RBC, WBC, and Platelet concentrations in the diluted sample. (Figure 1)

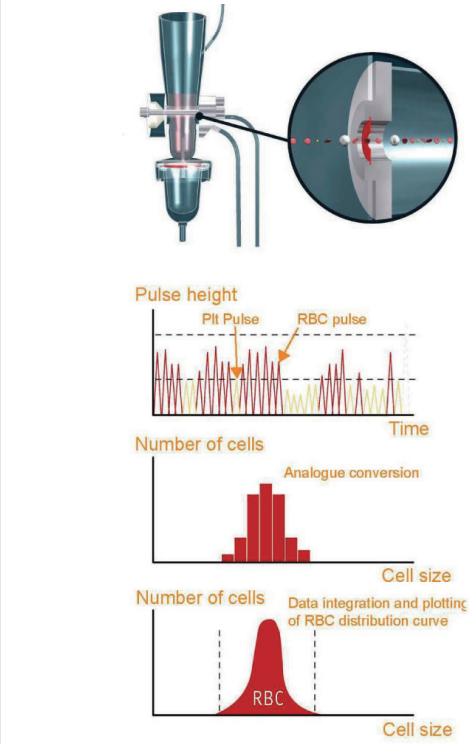

Figure 1

HEMOGLOBIN by ABSORBANCE SPECTROPHOTOMETRY

Traditional methods for measuring RBC hemoglobin used potassium cyanide (KCN) to form a cyanmethemoglobin compound. Absorbance was then measured by spectrophotometry at a wave length of 550 nm. The more ecology friendly Lysebio hemoglobin reagent formulation used on the HORIBA Medical ABX Pentra DX120 relies on an oxy-hemoglobin method eliminating the use of KCN. The absorbance value obtained is then multiplied by a coefficient in order to obtain the hemoglobin value.

WBC DIFFERENTIAL MEASUREMENT

In addition to impedance measurement, white blood cells in the sample are also evaluated by flow cytometry using a double hydrodynamic flow cytometer. Cell complexity is measured using cytochemical staining with chlorazol black and light absorbance from a polychromatic light source. Cell volume determination is made by measuring impedance changes. (Figure 2)

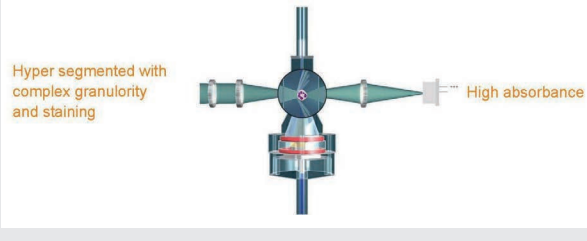

Figure 2

Identification and quantification of mature and immature WBC cell lines is accomplished by graphic representation in a double differential matrix. Lymphocytes, Monocytes, Neutrophils, and Eosinophils (LMNE) white cell types are distinguished by their size and complexity. Immature cell lines are further identified in an extended area of the matrix. (Figure 3)

RETICULOCYTE MEASURING PRINCIPLES

Reticulocytes are immature red blood cells characterized by remnant nuclear material within the cells. The Retic module of the HORIBA Medical ABX Pentra DX120 quantitates reticulocytes fluorimetrically with thiazole orange stain and an argon ion laser (488 nm). Thiazole orange is a fluorescent stain which is specific for nucleic acids.

A red cell passing through the Retic flowcell gives three

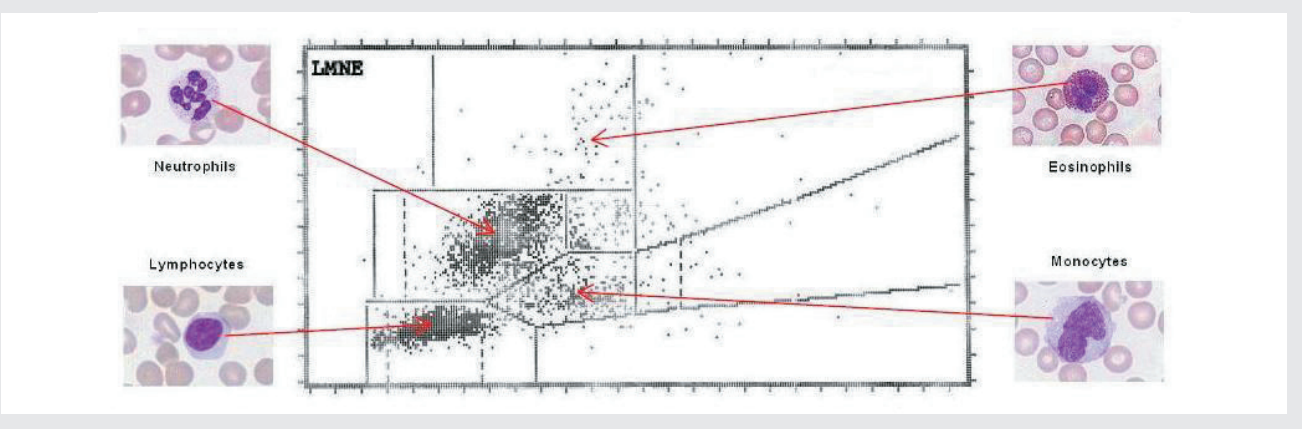

Figure 3

types of information: (1) The size of the cell is measured by resistivity (impedance); (2) Forward Scattered Light (FSL) is measured 200 microseconds after the aperture measurement; and (3) Orthogonal Fluorescence Light (OFL) is measured simultaneously with the FSL. (Figure 4)

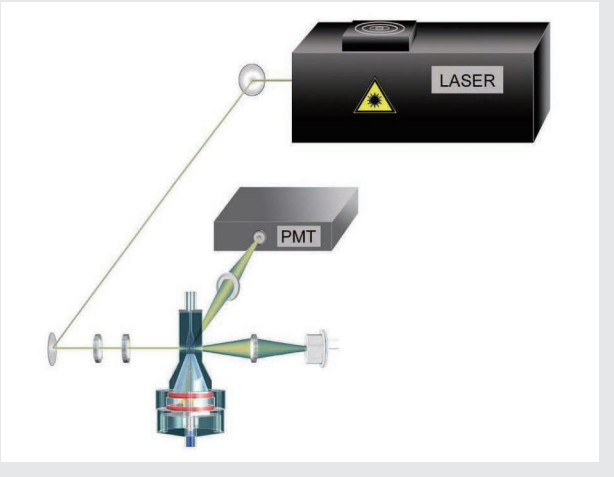

Figure 4

The fluorescence (OFL) is collected using a lens focused on the optical flowcell and located at 90° from the light beam. An interference filter specific to thiazole orange stain selects only fluorescent light (530 nm) which is then detected by a photomultiplier tube.

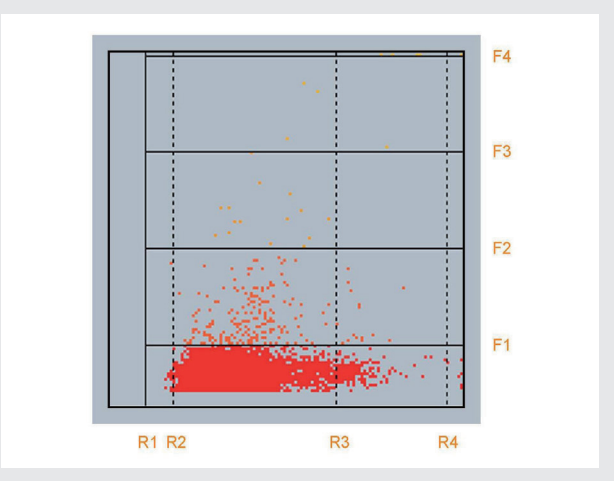

Figure 5

A reticulocyte matrix is then generated from two measurements: (1) Cell volume as determined by resistivity (impedance); and (2) Orthogonal Fluorescence. Mature red blood cells without nuclear material (RNA) show little or no fluorescent signal. They are located at the bottom of the matrix below F1 and horizontally distributed according to their mean corpuscular volume (MCV) and red cell distribution width (RDW). (Figure 5)

Reticulocytes are located in the upper portion of the matrix, and they are separated from the red blood cells by their fluorescence which is proportional to their RNA content and their maturity.

NRBC enumeration is accomplished in a manner similar to the enumeration of Reticulocytes.

CLINICAL USE of the HORIBA Medical ABX Pentra DX120

The CBC or Complete Blood Count is a routine panel of tests performed in many clinical laboratories. CBC test parameters include the enumeration of the Red Blood Cells, White Blood Cells with differential, Hemoglobin concentration, Platelet concentration and other test parameters.

The CBC is a valuable tool for the Physician to diagnose hematological disorders. A high White Cell count along with increased neutrophils in the WBC differential can indicate a bacterial infection somewhere in the body. Chronic bleeding and anemias can be diagnosed with decreased RBC counts and decreased hemoglobin concentrations. Oncology patients may have decreased platelets and other abnormalities in the CBC. Pediatric as well as adult and geriatric samples can be assayed on the HORIBA Medical ABX Pentra DX120.

In addition to CBC parameters, the HORIBA Medical ABX Pentra DX120 also can test for Reticulocytes and NRBC. These are immature forms of Red Cells which can be associated with blood loss or other disorders. Identifying an increase in the Reticulocyte percent can be a good sign indicating response by the body to blood loss with increased production of RBC. Manual enumeration of reticulocytes by hemocytometer is a tedious process requiring that the technologist count 1,000 red cells under a microscope. Automation of reticulocyte enumeration by the HORIBA Medical ABX Pentra DX120 is a valuable time saver for the clinical laboratory.

While valuable to the General Practitioner, the HORIBA Medical ABX Pentra DX120 is also valuable to specialty areas of medicine such as the Oncology practice. The extended differential of the HORIBA Medical ABX Pentra DX120 is valuable for identifying immature WBC

as found in certain types of leukemia patients.

BIBLIOGRAPHY

1. J.F.Koepke, MD, & J.A.Koepke, MD; Reticulocytes. *Clinical Lab. Haemat.* 1986, vol. 8:169-179.
2. B.H.Davis, N.C.Bigelow; Flow cytometric reticulocyte quantification using thazole orange provides clinically useful reticulocyte maturity index. *Arch. Pathol. Lab. Med.* 1989, pp113-184.
3. B.H.Davis, et al. Flow Cytometric Reticulocyte Analysis Multiinstitutional Interlaboratory Correlation Study. *Am.J.Clin.Pathol.* 1994, vol. 102:468-477.
4. J.X.Corberand, et al. Evaluation of the Pentra 120 Haematology Analyser in a university hospital setting. *Clin.Lab.Haem.* 1999, vol. 21:3-10.
5. G.Lippi, M.Nicoli, N.Modena, & G.Guidi; Clinical Performance of Leukocyte Differential on the ABX Pentra 120 Haematological Analyzer. *Eur.J.Clin.Chem. Clin.Biochem.* 1997, vol. 35(2):105-111.
6. R.Siekmeier, A.Bieflich, & W.Jaross. Determination of reticulocytes: Three methods compared. *Clin.Chem. Lab.Med.* 2000, vol. 38(3):245-249.

Jim Knowles
Product Manager
U. S. Hematology Marketing
HORIBA ABX Inc.

Terry K. Johnson
QC Laboratory Coordinator
HORIBA ABX Inc.

Feature Article

Spectral Imaging

Francis Ndi, Fran Adar, Salvatore H. Atzeni

Spectral Imaging encompasses a broad range of techniques for scientific image analysis, the end result of which is the production of both the image as well as the spectral composition of a scene of interest. A review of the typical implementations of spectral imaging is discussed in this article. Particular emphasis is placed on the manner of data acquisition, a distinction that frequently determines the suitability of one technique over another for a given application. Our new Simultaneous Hyperspectral Imaging camera is discussed. Its key feature is the ability to collect all spectral and image data in one shot. This feature makes our camera particularly suited to spectral imaging of dynamic scenes in the field as well as in laboratory and industrial environments.

Introduction

As the name suggests, spectral imaging refers to any imaging modality that has as its output a spatial description of a scene of interest as well as its spectral composition at discrete points (pixels) in the image. This output can be visualized as a four dimensional data set (or hypercube), with the first two dimensions (x,y) representing the spatial coordinates, the third dimension the intensity at that spatial point and the fourth dimension (Z) representing the spectral coordinate. Then, the projection of the intensities of any pixel in the (x,y) plane into the z-axis represents the spectrum at that point of the image (Figure 1). With this definition, spectral imaging can be thought of as a generalization of point spectroscopy.

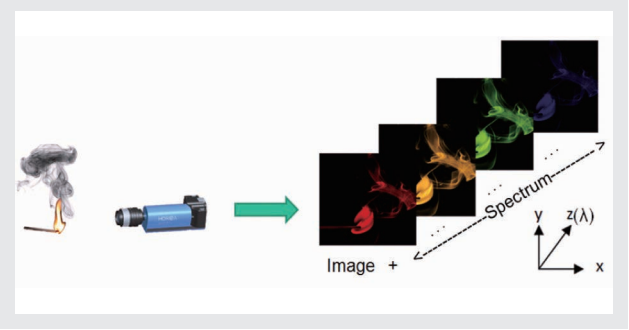

Figure 1 Spectral imaging generates an image of a scene as well as the spectral signatures of the different wavelength components of the scene.

Spectral imaging is recommended when the scene of interest is not homogenous and there is a need to characterize both the spatial as well as the various spectral signatures of the different components of the scene. The need for both spatial and spectral information is a very common requirement in many applications including geological and agricultural studies, color characterization in various media such as fabrics, paints and plasma monitors, as well as in many biological applications.

There are several classification schemes of the different spectral imaging methodologies. Perhaps the broadest of such schemes classifies all spectral imaging methods into one of two groups: *Multispectral* and *Hyperspectral* imaging.[1] In the former case there is a relatively small set of discrete wavelength bands while in the latter case the spectral axis includes a relatively large number of continuous wavelengths. According to this distinction, hyperspectral data sets would frequently contain more spectral detail than multispectral data sets.

A secondary classification scheme is based on the manner in which the spectral imaging data is collected and processed. This is frequently the basis for choosing one particular method over others for a given application. Spectral imaging data acquisition can be classified as either *sequential* or *simultaneous*.[2] Sequential spectral

imaging describes the case where the hypercube data is collected in a series of steps. In simultaneous spectral imaging the hypercube data is collected in one measurement step.

Sequential Spectral Imaging methods

The defining characteristic of the methods in this group is the collection of the hypercube data in a series of measurement steps. These may be further classified as scanning or filter-based methods.

Scanning Methods

Scanning methods include cases in which the hypercube is generated as a series of point spectra - each point being a discrete unit of space or pixel as shown in Figure 2a.[3] Another scanning technique is where the hypercube data is collected from a series of spatial bands or lines with each spatial band representing a discrete unit of space or a column of pixels. The technique is sometimes referred to as push-broom or line scan.[4] The spatial unit from which spectra are collected during each measurement is usually larger than the interrogated area in point methods (illustrated in Figure 2b) and contains multiple spectra, so that the hypercube is generated much faster than is typical with point methods.

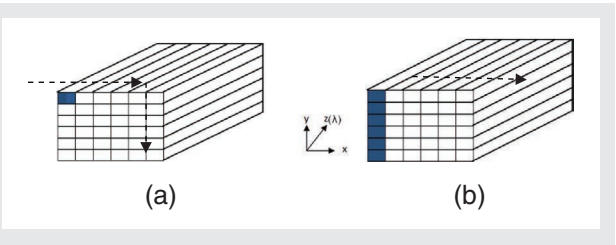

Figure 2 (a) The blue rectangle represents the spatial unit (pixel) from which a spectrum (z-axis) is collected during each measurement. The measurement is repeated over all pixel positions in order to generate the hypercube. The process is usually slow with the achievable spatial resolution limited by the collection optics. (b) Represents a push-broom technique with data collected over a spatial column and typically imaged on an array detector via a spectrometer. Push-broom techniques are typically faster than point methods.

The point scanning methods are frequently used when one is limited to using commonly available point spectroscopy methods — usually microscope-based (Raman, Fluorescence, etc) when it is necessary to generate an image of an inhomogeneous field of view. In these cases a raster-scan (x,y) of the field is performed and a composite spectral image generated from a series of point spectra (see Figure 2a). The line scanning method is usually employed when a segment or column of the field of view can be imaged via a spectrograph onto a 2-dimensional array detector thereby collecting all the spectral data for that column in the field of view. In this instance, one need only scan in one direction to obtain the complete hypercube as shown in Figure 2b.

In both cases (point and line), there is a need to physically move either the object of interest or the imaging spectrometer assembly in a sequential fashion in order to obtain the complete hypercube. The relative motion between the object of interest and detector assembly makes the scanning methods unsuitable for cases in which the phenomenon being monitored is changing on a time scale much shorter than the scan time of the detector assembly (except when the relative motion between object and detector is synchronized with the phenomenon being measured). Furthermore, the motion requirement makes scanning measurements particularly susceptible to errors from mechanical aberrations. Perhaps the most significant advantage of scanning methods is the flexibility to choose from a range of spectrographs offering low to very high spectral resolution and also the possibility of using well established point-spectroscopic techniques. Thus, these are the methods of choice when one is more concerned with more spectral information at a small number of spatial points.

Filter-based Methods

Filter-based methods include all spectral imaging techniques in which all the spatial information at a given wavelength (or narrow band of wavelengths) is captured in one measurement and the hypercube is generated by repeated acquisition of a set of narrow band images at sequential wavelengths as shown in Figure 3.

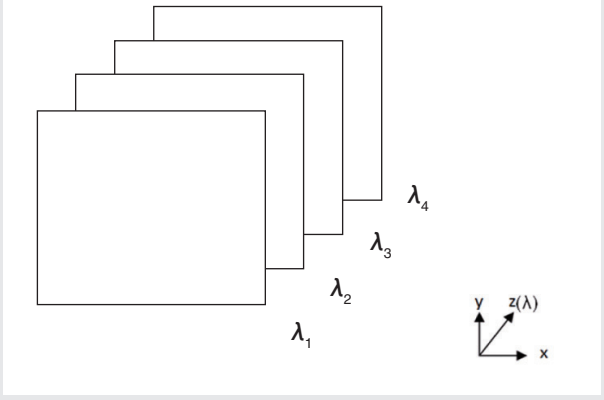

Figure 3 Filter based hypercube generation.

The filters used in filter-based spectral imaging can be passive filters selected apriori or dynamic (tunable) filters allowing selection of specific wavelengths of interest.[2] Common tunable filters used are based on acousto-optic (AO) or liquid crystal (LC) technology. In both cases voltages are used to change the refractive indices of the

filter material resulting in a voltage-dependent transmission bandpass. The ability to easily change the filter properties offers the added advantage of dynamically selecting the spectral bands of interest.

Similar to filter-based techniques but implemented differently are techniques that achieve the filtering function by the use of dispersive media such as prisms, so that the spectral images are dispersed in space and can be recorded by using different sensors or using one sensor that moves to different locations in space to record the spectral signature at those points.

Like the scanning methods, the filter-based spectral imaging modalities are limited by the tuning speed from one wavelength band to another, which can vary from several seconds in the case of passive filters on a wheel to a few microseconds in the case of the acousto-optic and liquid crystal technologies. In the case where the tuning function is achieved by the use of passive media such as prisms, the acquisition speed is limited by the time it takes to move the detector from one point to another, or to move the desired image in front of a static detector by rotating the prism. Also, the tuning efficiency of acousto-optic elements and liquid crystals is usually temperature dependent, adversely affecting performance when the ambient temperature is not well controlled. In general the filter based methods are usually faster than the scanning methods and offer very high spatial resolution since the entire sensor is used to register only one spectral slice of the hypercube during each measurement. Thus, these are the methods of choice when one is more concerned with more spatial information at a few wavelengths.

Simultaneous Spectral Imaging Methods

Simultaneous spectral imaging methods are superior to the sequential spectral imaging methods discussed above, at least with respect to acquisition speed. In such cases, the necessary data for generating the hypercube is captured in one measurement step on a time scale that is usually much shorter than any changes in the scene of interest.

Pseudo-Simultaneous Spectral Imaging Methods

For relatively static scenes, several techniques based on multiple filters, multiple sensors, or both, have been used to collect hypercube data. These methods attempt to maximize the number of color planes while minimizing the total acquisition time of the hypercube. In the multi-filter scenario, practical limitations generally dictate eight to sixteen colors using optical filters mounted on a spinning disc placed before the image sensor. The filter positions on the spinning disc are synchronized with the sensor's exposure circuitry, capturing one image of each color in a rapid sequential fashion. While relatively fast, these methods are limited to situations where temporal requirements are not extremely demanding.

HORIBA Scientific Simultaneous Hyperspectral Imaging Camera

While there are methods intended for rapid capture of hypercube data (as described in section 2.1 above), as of this writing there are no truly simultaneous hypercube acquisition instruments on the market. HORIBA Jobin Yvon Inc., in partnership with Snapshot Spectra Inc. of Pasadena, California has developed a new, patented Simultaneous Hyperspectral Imaging (SHI) camera system. This camera is capable of capturing all the data needed to generate a hypercube in one shot, in as little as 3 milliseconds. The acquisition speed is determined mainly by the type of sensor being used.

The technology relies on a two-dimensional transmission grating sandwiched between a pair of imaging lenses (see Figure 4b).[5] The first lens from the left serves to collimate the light coming from the scene of interest and the second lens re-images the diffracted light from the grating onto the sensor. The uniqueness of the system derives from the grating design which creates a two dimensional diffraction pattern at the sensor. The image projected on the sensor consists of an accurate representation of the field of view in the center of the image (undiffracted zeroth order) and higher diffracted orders around the center. Since the angle of diffraction is a function of the wavelength, with the angle increasing from short (blue) to long (red) wavelengths, the higher order diffracted images consist of a smearing of the wavelengths across the sensor containing all the spectral information in the scene (see Figure 5a). The hypercube

Figure 4 (a) Prototype of Hyperspectral Imaging Camera. (b) Functional components (within the blue casing in the prototype in Figure 4a).

Figure 5 (a) Raw image from Hyperspectral camera. The image consists of a zeroth order image that replicates the original scene surrounded by several higher diffraction orders in both directions. The diffracted orders contain all the spatial and spectral information in the scene. The bottom right insert is an image of the scene taken by a regular camera. (b) Illustration of hypercube generated by software reconstruction using the image in (a) as input.

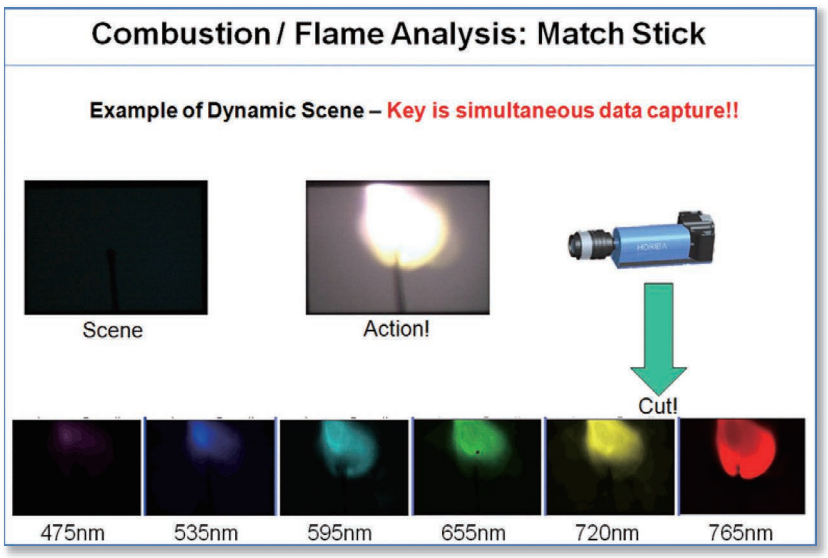

Figure 6 Example of a dynamic scene (flaring of a match stick). The bottom row shows a few slices of the hypercube in pseudo-color with the colors downshifted so that the highest wavelength is shown in red.

(illustrated in Figure 5b) is generated from a software reconstruction algorithm using the raw image data as input.

Figure 6 shows an example of a typical application for this technology. In this simple example of combustion analysis, the SHI camera captures both the image and the spectra from a flaring matchstick. A critical requirement for the spectral imaging system in this case is the ability to capture all the spatial and spectral data simultaneously as the scene is rapidly changing with time.

Conclusion

Spectral imaging is becoming increasing important as users seek to multiplex data collection in order to save time (as is the case in multiple fluorophore excitation in bio-imaging applications),[6] or in applications where neither spatial or spectral information alone is sufficient, such as multispectral mixing analysis. HORIBA Jobin Yvon Inc. will soon release a new simultaneous hyperspectral imaging camera which will offer both the rich data sets afforded by spectral imaging as well as the ability to collect all the necessary data in a truly simultaneous fashion. The design is very portable and does not have any moving parts, making the architecture fairly rugged. This combination of features makes the hyperspectral imaging camera described here an ideal system for applications involving spectral imaging of transient phenomena that cannot be measured using more conventional techniques such as in engine combustion diagnostics.

References

[1] http://en.wikipedia.org/wiki/Multi-spectral_image
[2] Takayuki et al., Optics Letters, Vol. 16, No. 16, August 1991
[3] F. Draux et al., Analyst, 2009, 134, 542-548
[4] R. G. Sellar et al., Opt. Eng. 44, 013602 (Dec. 17, 2004)
[5] M. R. Driscour et al., Optics Letters, Vol. 22, No. 16, Aug 1997
[6] H. R. Morris et al., Applied Spectroscopy, Vol. 48, Issue 7, pp. 857-866 (1994)

Francis Ndi

Applications Scientist
Optical Spectroscopy Division
HORIBA Jobin Yvon Inc.
Ph. D.

Fran Adar

Raman Principal Scientist
HORIBA Jobin Yvon Inc.
Ph. D.

Salvatore H. Atzeni

Vice President
Optical Spectroscopy and CTO
HORIBA Jobin Yvon Inc.
Ph. D.

Feature Article

The Role of Detectors in Spectroscopy

Salvatore H. Atzeni, Linda M. Casson

The role of the detector in optical spectroscopy has evolved over the years, as advances in technology, driven by application requirements, have made the detector much more than simply a transducer at the end of an optical arrangement. Earlier instruments generally consisted of a relatively high-cost spectrometer and a low-cost detector such as a photomultiplier tube (PMT). Thus, the detector was an accessory to the spectrometer. As detector technologies improved, the capability, complexity and expense of the detector increased, placing a lower emphasis on the capabilities of the spectrometer, whose design and capabilities remained relatively constant during the same time period. Today, many researchers accept the notion that the detector is the heart of a spectroscopic system, and the optical subsystem is more of an accessory to the detector. The evolving role of the detector, from an accessory to a key component, was driven by rapid advances in technology as well as cost reduction of complex technologies. In many cases, modern spectroscopic instruments are designed as an integrated system in which the detector is an integral part of the spectrometer or spectrograph, making it possible to optimize the spectroscopic system performance at even lower cost. In this Article, we discuss some common detector choices, their roles in the spectroscopic detection arena, and salient points related to selection, advantages and key performance metrics. Examples of HORIBA Jobin Yvon, Inc. detector products and technologies are provided to illustrate sample implementations that address common application requirements.

Introduction

Optical methods play an increasingly important role in the modern world. From the telecom industry to the food industry, light measurement instruments make a large contribution to the way we live. Optical spectroscopy allows measurement of various phenomena, often in a safe, nondestructive manner, with possibilities for remote sensing when a sample is located far from the instrument. Many techniques allow excellent quantitative analysis, with selectivity and sensitivity towards specific analytes. All optical spectroscopic measurement systems include a detector, but depending on the application, may also include a light source to stimulate the sample being measured, and a filter or dispersive element (commonly a diffraction grating or prism) which separates the light into its constituent colors before being measured by the detector subsystem.

Optical detectors used in spectroscopic instruments are often classified as either single-channel detectors (SCDs) or multichannel detectors (MCDs). Single-channel detectors have one active sensing element that acts as single transducer. Photons reaching the detector, within its operating wavelength range, are absorbed by the active material of the detector and encoded as an electrical signal. The output signals produced by the detector vary according to the detector specifications, but generally include analog (voltage or current) and digital (pulse-counting) domains. A spectrometer with its PMT is operated by moving the diffraction grating to present different wavelengths to a focal point at the exit slit, where the PMT will sequentially record the signal, one wavelength at a time. In contrast, multichannel detectors have multiple active sensing areas which collect many wavelengths simultaneously at the focal plane of a spectrograph. No exit slit is used in this arrangement. Each arrangement has advantages and disadvantages, and

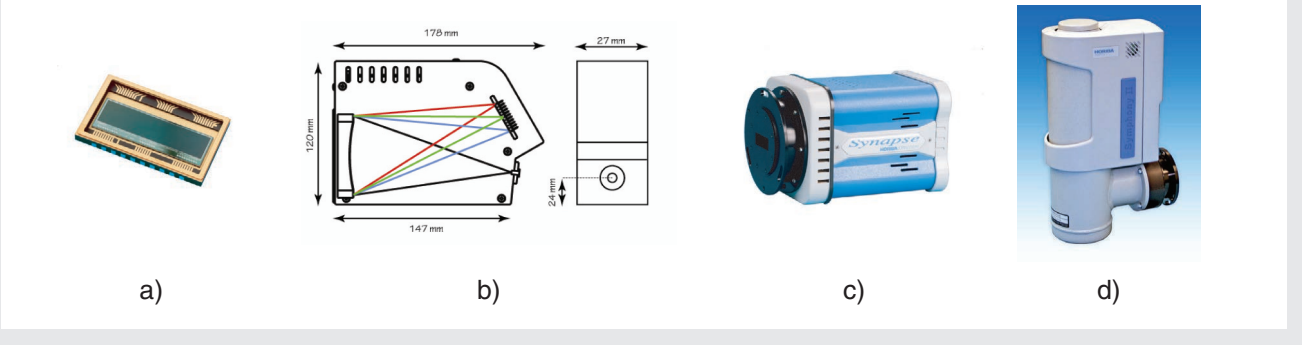

Figure 1 From left to right: a) A typical CCD sensor chip [e2v Technologies, Ltd. Model CCD30]; b) shown mounted in an integrated spectrograph [HORIBA Jobin Yvon, Inc model VS-140]; c) mounted in a thermoelectrically-cooled housing [HORIBA Jobin Yvon Inc. model SYNAPSE]; d) mounted in a cryogenically-cooled Dewar [HORIBA Jobin Yvon, Inc. model SYMPHONY-II].

it is the application requirement that defines which configuration is most suitable.

While they are excellent photon transducers, optical detectors exhibit some intrinsic background, even when no optical signal is present. Most detectors used for spectroscopy benefit from cooling to reduce this background signal. As the detector is cooled below room temperature, often to very low operating temperatures, the background signal and its associated noise component is reduced. Common cooling techniques involve thermoelectric as well as cryogenic cooling using liquid nitrogen. To eliminate condensation and the potential for corrosion, the sensors themselves are often mounted in a vacuum housing and sealed using hermetic methods, ensuring years of maintenance-free use.

In this Article, we offer an overview of many commonly used detectors for spectroscopic applications, from the UV (150 nm) to the mid-IR (20 microns). As many devices exist in the marketplace, we choose to limit the scope of this discussion to scientific-grade detectors, which differ considerably from consumer-grade products in terms of performance, complexity and cost.

Single-Channel Detectors (SCD)

Probably the best known detector is still the classic PMT, which offers good performance in detecting photons across a relatively wide wavelength range at modest cost. However, many types of single-channel detectors are available on the market today. They are classified according to the method of optical to electrical conversion. First, a photon is absorbed by the material creating an electron-hole pair. If the generated photoelectron is further emitted from the material, becoming available for collection or multiplication, the device is called a photoemissive device, or one based on the external photoelectric effect. PMTs are the most common example of this type of detector. If instead no emission takes place but the photogenerated electron-hole pair is available for the current circulation in an external circuit, we call this an internal photoelectric device. Solid state detectors fall in this category, but may be subdivided

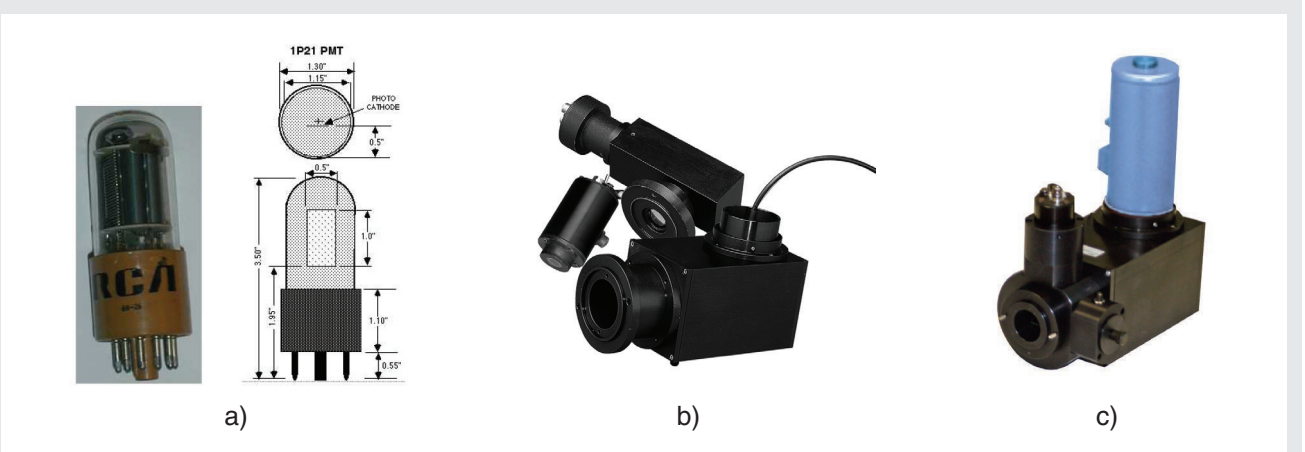

Figure 2 Examples of common SCDs. From left to right: a) a standard, side-on PMT; b) a thermoelectrically-cooled InGaAs detector and optical housing; c) a cryogenically-cooled InGaAs (HORIBA Jobin Yvon model DSS-IGA-020L with 1427C housing). The optical coupling from the exit slit to the small active area of the detector is accomplished using an elliptical mirror, compressing the slit height by 6:1.

into photovoltaic (photodiodes, for the visible-NIR range) and photoconductive (or photoresistive, for the MIR). Although photoemissive devices frequently have gain, providing higher sensitivity, they have the drawbacks of vacuum tube technology, requirement for high-bias voltage and limited spectral range of operation.

A third category of photodetectors is thermal detectors. These operate according to a two-step process: first, radiation is dissipated in an absorbing material; then the resulting small increase in temperature is measured by a change in the electrical properties (such as resistance) of the material. Although these detectors often cover a broad spectral range (visible - MIR), they have much lower sensitivity compared to the other categories of photodetectors and are not often used in spectroscopy except in limited cases in MIR systems. Table 1 summarizes typical characteristics of these devices.

Table 1 Categories of single-channel detectors

Category	Detector	Typical active area	Spectral Ranges
Photoemissive (external photoelectric) devices	Photomultiplier tube	Few mm up to 25 mm diameter	< 100 nm - 1650 nm
Internal photoelectric devices	Semiconductor photodiode Avalanche photodiode Photoconductive detector	1 - 3 mm diameter 20 - 80 µm diameter 1 - 2 mm diameter	200 nm - 20 µm
Thermal detector	Thermocouple (thermopile) Bolometer (or thermistor) Pyroelectric	10 - 20 mm diameter 1 - 2 mm diameter 1 - 2 mm diameter	300 nm - > 100 µm

Detectors are selected based on experimental requirements. The first selection criterion is the wavelength range to be measured. In many cases this will narrow the choice down to one or two detectors. For example, if the wavelength range is 7 - 15 µm, an HgCdTe detector will be the only option. However, if the wavelength range is 400 - 700 nm, there are several options with the choice of optimum detector depending on other experimental requirements. For steady-state measurements with high light levels and a sample that is not easily damaged by exposure to light, either an uncooled PMT; or uncooled or TE cooled silicon photodiode (especially if future research plans involve NIR measurements) would be a good choice. For extremely low light levels, a PMT with photon counting will be the best choice.

Table 2 shows the spectral response for the most commonly used solid state detectors. These detectors are most commonly used for steady-state measurements, but in certain cases, when coupled to a fast amplifier, may also be used for time-resolved measurements. When two detectors cover a similar wavelength range, such as InGaAs and Ge, the choice is based on gain, noise factors and response at a specific wavelength of interest. Ease of operation, based on not needing liquid nitrogen may also be a factor.

Table 2 Typical Wavelength Ranges for HORIBA Jobin Yvon Solid State Detectors

Solid State Detector	Wavelength Range	Photovoltaic (PV) or Photoconductive (PC)
Silicon	200 - 1100 nm	PV
InGaAs	800 - 1700 nm	PV
InGaAs (LN_2)	800 - 1550 nm	PV
InGaAs (2.2 µm, LN_2)	1.1 - 2.2 µm	PV
Ge	800 - 1800 nm	PV
Ge (LN_2)	800 - 1550 nm	PV
PbS	1 - 2.8 µm	PC
PbSe	1 - 4.5 µm	PC
InSb	2 - 5.5 µm	PC
HgCdTe (MCT) (others ranges available, depending on elemental composition)	2 - 14 µm 2 - 20 µm	PC

The next consideration is whether the measurements require temporal analysis. For example, fluorescence lifetime measurements provide a much more detailed observation of the molecular processes that occur in biology and biophysics, materials science, and chemistry than do steady-state measurements. The fluorescence lifetime τ of these materials generally ranges from a few picoseconds to hundreds of nanoseconds. Figure 3 shows an example of a fluorescence lifetime measurement on

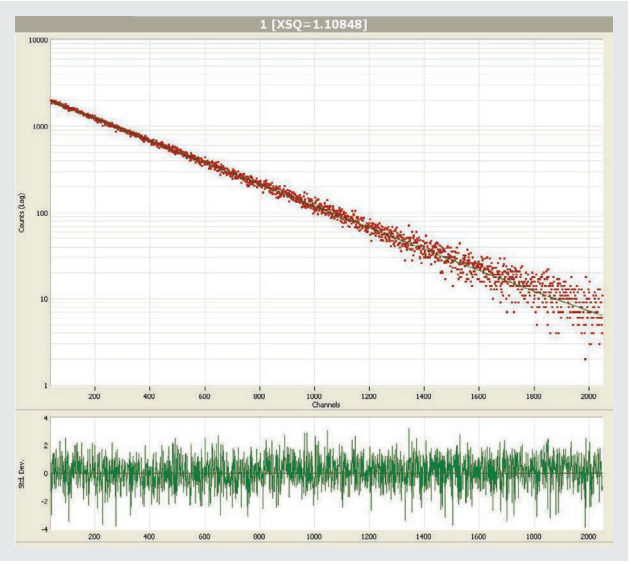

Figure 3 TCSPC measurement of KCl:Eu^{2+} exhibiting a lifetime of 1.19 microseconds.

$KCl:Eu^{2+}$, obtained using Time Correlated Single Photon Counting (TCSPC).

There are 2 basic techniques for measuring fluorescence lifetimes: frequency domain measurements (such as in our MF^2 instrument) and time-domain measurements (including TCSPC and transient decay methods). By careful design of the electronics, a relatively inexpensive PMT can be optimized to perform picosecond lifetime measurements. With a carefully tuned fast amplifier-discriminator circuit, these PMTs can be used for TCSPC measurements to obtain lifetimes of biological, nanomaterials and other samples. The most popular models use a multi-alkali photocathode and cover the spectral range 185 - 850 nm, with some optimized for a particular subsection of this range. Other PMTs with different photocathode composition are optimized to extend the spectral response up to 1 micron. Variants that extend beyond 1 micron are available, however, these are costly and require careful handling as they can be easily damaged by excess light, rendering them less effective in the red and possibly destroying the tube. Generally, due to cooling requirements imposed by the higher thermionic emission, these models extend the usable range to approximately 1.6 microns. Photoluminescence (PL) and Electroluminescence (EL) lifetimes may be measured using the same experimental methods.

Another single-channel detector used in spectroscopy is the avalanche photodiode (APD)[1]. This is a small device made of silicon or InGaAs, which may be operated in single photon-counting mode (Geiger Mode), sometimes abbreviated "SPAD", which has very high gain and can be used to measure very low light levels. The disadvantage of this device is that it has very high dark current and associated shot noise, even for a detector with a diameter 80 microns or less, and must be cooled. Another new type of single-channel detector with potential use in spectroscopy is the discrete amplification photon detector (DAPD), which uses a novel approach to reduce the excess noise factor inherent in Geiger-mode APDs from approximately 1.3 to less than 1.05 with gain of 10^5 with nanosecond risetimes. These devices may be produced from silicon or indium-gallium arsenide materials, offering a potential alternative to the PMT.

Multichannel Detectors

The most popular multichannel detectors for spectroscopy are silicon based charge-coupled devices (CCDs) with several thousand elements, or pixels, arranged in a rectangle. Inexpensive linear CCDs (and photodiode arrays) are available on the market, but in most scientific applications, 2D CCDs are used. Scientific-grade CCDs exhibit high responsivity from the near-ultraviolet to the near-infrared (NIR) region of the spectrum — 200 nanometers to 1.1 microns. At longer wavelengths, the photon energy is lower than the silicon bandgap and the silicon becomes transparent to the incident photons. However, III-V semiconductor materials such as indium gallium arsenide (InGaAs) have a lower energy bandgap and can absorb the NIR photons (see Figure 4). For this reason, InGaAs arrays are the array detector of choice between 0.9 and 1.7 μm, and are now available up to 2 μm. Other multichannel detectors such as HgCdTe and InSb MIR arrays are available, but are not used as frequently, mainly due to their high cost.

In spectroscopy mode, a CCD works by first summing the electrical charges of the selected pixels in a column at the bottom of that column of the array into a "super-pixel". This charge-shifting is called a parallel shift. The combined charge from each of these superpixels is transferred serially by the readout register to the output node amplifier. Here, these individual charges are read out and transferred to the ADC (analog-to-digital converter) and processed by the electronics. In a full frame (FF) CCD, the entire array is exposed to light. In a frame transfer (FT) CCD, the top half of the array is exposed to light and the bottom half is used to store the electrical charges before readout. This format allows faster spectral acquisition rate, and may sometimes be used for kinetics measurements. At the time of this publication, all CCDs supplied by the Optical Spectroscopy Division of HORIBA Jobin Yvon, Inc. are FF devices.

Silicon CCDs are available with various options to optimize performance. A basic, front-illuminated CCD may be coated with a phosphor to enhance its UV response. The phosphor absorbs the UV photons and re-emits green photons in the spectral range where the CCD is most sensitive. Modifications also can be made to the gate structure in order to improve the detection and raise the effective QE. This variation is called an "Open Electrode" (or "Open Poly") CCD. In such a device, approximately one third of the gate is removed in the center of the pixel, allowing more light to reach the silicon, which improves detection. In a back-thinned CCD, the entire device is thinned so that it can be illuminated from the rear of the CCD which eliminates the problem of absorption from the polysilicon gates on the front. Because of the reduced silicon thickness, however, constructive and destructive interference may occur, resulting in an etalon effect that produces a pattern on the signal sensitivity, which can be difficult to correct

mathematically.

In another modification, CCD devices are made from special high resistivity material, creating deeper depletion layers in the silicon, resulting in a thicker active layer in which long-wavelength photons are more likely to be absorbed, enhancing the QE in the red region of the spectrum[2,3].

Because CCDs are used for many applications, new types are appearing all the time. Pixel sizes are decreasing, which can improve spectral resolution, but at the same time decrease apparent sensitivity and dynamic range, since the charge capacity of each pixel decreases with size. Higher pixel densities also require longer readout times after exposure. Manufacturers of analytical spectroscopic instruments are constantly making tradeoffs in order to supply high sensitivity and speed while maintaining affordability.

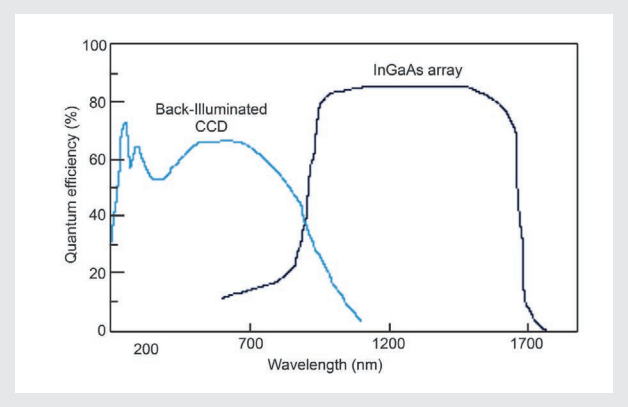

Figure 4 The spectral response of typical silicon and indium gallium arsenide (InGaAs) detectors shows the usefulness of InGaAs for near-infrared measurements.[4]

Other types of CCD detectors are available that augment the capabilities of standard detectors by adding gain and temporal resolution/gating. These include the Electron Multiplying CCD (EMCCD) and the Intensified CCD (ICCD) detectors.

Electron-multiplier charge-coupled devices (EMCCDs)

An EMCCD may be thought of as a standard CCD with optional gain. They are often used for low-light applications with fragile samples, including biological applications and single-molecule work, where the option of integrating the signal for longer periods of time does not exist due to the transient nature of the sample. EMCCDs are often used for imaging applications, and are commonly available in square formats intended to be used in microscopy, but are also available in other aspect ratios, making them more useful for spectroscopy. EMCCDs have on-chip gain, which is derived from a cascade register arranged between the serial register and a second output node. As the charge from each pixel is clocked out, the magnitude of this charge is increased as it steps through the gain register. Typically, the gain can be adjusted over a range of values, reaching as high as 103. While useful, there are some caveats in using this gain mode for quantitative work, and to alleviate this concern, many EMCCD sensors have both a 'standard' as well as a 'multiplier' output, giving the researcher the option of using the most appropriate mode for their particular experiment.

Intensified charge-coupled devices (ICCDs)

ICCDs also provide for amplification of the optical signal, here by passing it through an image intensifier tube (IIT). The IIT uses a standard photocathode material to convert incident photons to photoelectrons, much as a PMT does. These photoelectrons are then accelerated towards one or more microchannel plates (MCPs) which perform amplification in a manner analogous to the dynodes of a conventional PMT. The gain can be controlled by adjusting the bias voltage(s). The photoelectrons, now increased by several orders of magnitude, then strike a phosphor plate, which emits luminescence in the blue to green region of the spectrum. This light (often seen in videos as night-vision images) illuminates a CCD sensor which is operated in the integrating mode and read out in the normal manner. An ICCD has an image intensifier coupled to the CCD either by relay lenses, or more commonly, directly coupled using a fiber optic faceplate[5]. An additional capability of the ICCD is its potential for time-resolved spectroscopy, as the IIT may be gated from DC (steady-state) to the nano- to picosecond time scale. This characteristic is useful for monitoring chemical kinetics or other time-resolved measurements including fluorescence and Raman. In the case of Raman time-resolved measurements, the ICCD is gated in a manner to pass the prompt Raman signal, but then block the longer lived fluorescence emission that may also be present in the sample. A common spectral imaging application involving a spectrometer coupled to an ICCD would be the temporal characterization of plasma emission.

Additional technologies

Other silicon-based multichannel detectors are now on the market. Most of these are read out by each individual pixel (rather than by shifting charge to the readout register as with a CCD), and the spectrum is reconstructed by the host software during post-processing. Some CMOS array detectors may be read nondestructively, so it becomes possible to use various integration times for each pixel without having to read out the entire sensor. This may be exploited to increase the dynamic range of a measurement. The scientific CMOS detector (sCMOS), a relatively new technology, is used for imaging — including machine vision such as inspection of defects in semiconductors, and is beginning to be used in microscopy. Infrared multichannel detectors, often called "focal plane arrays" are available in InGaAs, InSb and HgCdTe materials.

One interesting application using a 2D multichannel detector is called multi-track spectroscopy. In this type of measurement, a linear bundle of fibers is presented at the spectrometer entrance, with each of the fibers collecting light from a different analyte or part of an extended sample. The multichannel detector is divided into a number of horizontal strips, corresponding to the output from each fiber. In this manner, multiple spectra can be measured simultaneously.

Readout Electronics

In addition to the detector sensors themselves, the readout electronics associated with a detector, in particular with a multichannel detector, contribute to performance of the detector and spectroscopy system as a whole. HORIBA Jobin Yvon is well known in the industry for its superior readout electronics, especially for the Synapse CCD and InGaAs detectors. The use of correlated double sampling and other techniques produce detection systems with extremely low noise and high data fidelity allowing better overall performance of HORIBA Jobin Yvon spectroscopy systems compared to systems from other manufacturers using similar sensors.

Choosing a Detector

A multitude of detector options have been presented in this article. Here is a general set of questions to serve as guidelines to help the user narrow down the range of choices and select the most appropriate detector for the application.

1. What is the wavelength range of the measurement?
2. What spectral resolution is required for the measurement?
3. Can the application be addressed with a lower cost single channel detector or is a multichannel detector required?
4. Is the measurement steady-state (DC/continuous) or a time-resolved/kinetics measurement?
5. What is the expected light level or photon flux to be measured?
6. Are measurements being made on a fragile sample: one which is short-lived or susceptible to damage from exposure to light or other environmental factors?
7. What is the size/form factor of the light focused on the spectrometer entrance slit to be analyzed (such as spot or vertical line)?
8. Will the choice of this detector allow the user to upgrade the system to add detectors for future projects if desired?
9. Who will be using the system? (e.g. technicians, students, multiple research teams/projects, single research group)
10. What is the budget?

The first seven questions require clear definition and analysis of the application. Specification of the wavelength range is fairly straightforward. In certain cases when multiple samples may be studied, the user may need to initially accept a lower spectral range, with the intention of extending the range in the future.

Definition of the required spectral resolution is fairly straightforward, but may determine whether or not it is possible to use a CCD or multichannel detector. For applications with relatively low spectral resolution requirements, greater than several angstroms, in the spectral range below 2 microns, a multichannel detector will probably be a good option. But, for higher resolution, careful calculations must be performed to ascertain whether pixel size will limit the spectral resolution. It is not always possible to achieve the required resolution of a MCD system by increasing the dispersion (by increasing the grating groove density, increasing the focal length of the spectrometer, or both), especially when considering the required spectral range. Thus, effective slit widths that are smaller than typical pixel sizes are required. In cases where additional dispersion can not compensate for the size of the pixels, a SCD behind a narrow slit will often yield the required resolution.

As for SCDs versus MCDs, as a general rule, when multiple wavelengths bands need to measured, MCDs offer faster data acquisition or superior signal to noise compared with SCDs due to the Felgett multichannel advantage - namely that instead of measuring one

wavelength band at a time, you can measure multiple bands for the same amount of time. Their tradeoff is cost and complexity. For single or a small number of wavelength bands, SCDs can offer optimum performance at a lower cost. Also, for certain temporal requirements, such as sub 100s of picoseconds, an SCD is the only option. Similarly, the choice of array detectors for wavelengths greater than 2 microns is very restricted and includes few, if any, practical options.

The answer to the fourth question should also be straightforward: if the application involves time-resolved measurements certain detector choices may be eliminated, although the specific technique must still be defined.

The fifth and sixth questions can often be answered by doing preliminary literature investigation of the sample to be studied. Low light level measurements require a detector with high sensitivity and gain, and the capability for long exposure times. The background signal level in the entire spectroscopy system must also be considered. A fragile sample cannot be studied using a detector requiring a long exposure time, so either some type of CCD or PMT with photon counting may be a good choice.

The seventh question requires a good deal of thought. Since the image of the light at the entrance of the spectrometer is projected onto the monochromator exit, the size and shape are important to consider. If a 6 mm tall linear fiber bundle (6 fibers) is mounted at the entrance slit, the detector at the exit should be tall enough to capture all of the photons. An avalanche photodiode with 50 micron diameter mounted directly at the exit slit will not work well, although a PMT with an 8 mm diameter photocathode will be fine. A 2 mm diameter photodiode mounted in a housing containing an elliptical mirror (6x de-magnification) will work well. If the application requires the capture of 6 spectra (one from each fiber) simultaneously, a 2D CCD is required.

The remaining questions require the user to consider the robustness of the detector, whether the housing and mounting hardware will allow additional detectors to be added or substituted, and the amount of daily upkeep and care that is required.

Conclusion

The detector is an integral part of any spectroscopy system. It is not merely an accessory, yet nor does the detector alone determine the performance of the total system. Choosing the best possible detector maximizes the potential of the system as a whole to achieve optimal sensitivity, dynamic range and signal to noise ratio for the application. This principle applies whether using a spectrometer with a single channel detector or a spectrograph with a multichannel detector. As new materials and technologies are developed, new types of detectors will continue to become available. The team at Horiba Jobin Yvon is prepared to test and integrate new types of detectors to keep up with ever more demanding requirements of emerging applications and more challenging measurements using optical spectroscopy.

References

[1] Donati, S., Photodetectors: Devices, Circuits and Applications, Prentice Hall PTR, Upper Saddle River, NJ, 2000.
[2] Janesick, J.R., Scientific Charge-Coupled Devices, SPIE Press, Bellingham, Washington, 2001.
[3] Janesick, J.R., Photon Transfer, SPIE Press, Bellingham, Washington, 2007.
[4] Adar, F., Atzeni, S., Gilchrist, J., Goldstone, L., Noonan, J., Laser Focus World, Vol 38, Number 4. 7.
[5] ASTM Standard E2642-08, Standard Terminology for Scientific Charge-Coupled Devices (CCD) Detectors, ASTM International, West Conshohocken, PA, 2008.

Salvatore H. Atzeni
Vice President
Optical Spectroscopy and CTO
HORIBA Jobin Yvon Inc.
Ph. D.

Linda M. Casson
Senior Application Scientist
HORIBA Jobin Yvon Inc.
Ph. D.

Feature Article

A Cross-Discipline Article on Photovoltaic Measurements
— HORIBA Scientific instrumentation for the photovoltaic market —

Emmanuel Leroy

HORIBA Scientific manufactures several pieces of equipment that perfectly fit into the area of material research applied to photovoltaic technologies, with capabilities that extend from the lab into the fab, to serve the needs of the research community and industry alike. A review of the status of different solar cell technologies is presented here, as well as an overview of our Scientific division technologies of interest to provides background information about applicable techniques. Several typical current applications are then presented, and future potential areas of interest are identified.

Introduction

The photovoltaic industry has grown steadily in the past decade to become a noticeable source of energy, and a promising source of renewable energy. However popular the technology is today, performances are still far from the theoretical limits of solar-energy conversion, which is why solar energy brings great hopes of becoming a cost-effective alternative to fossil fuels. First-generation cells are now mass-produced by the hundreds or thousands of megawatts to reduce cost, while much research efforts are put into improving second-generation and developing third-generation cells.

Solar-cell technologies and materials

The primary material used in the solar industry, especially in first generation cells, is the well-known silicon (Si), easily extracted and purified from sand, and therefore theoretically available in quasi-unlimited quantities. Crystalline silicon (c-Si) yields the best performances, yet it is more expensive to produce, and multi-crystalline Si, amorphous, poly-crystalline, and mixtures of those, tend to be more cost-effective; these therefore have dominated the market in terms of volume produced, despite the larger surface area needed per watt. Surface area is typically not the limiting factor for large commercial projects or solar farms. On the other end of the spectrum, solar-concentrator cells pack very high efficiency into small cells typically made of III-V semiconductor materials such as gallium arsenide (GaAs), indium gallium arsenide (InGaAs) and/or indium gallium phosphide (InGaP). In these smaller cells optical elements (concentrators) are used to focus light from a larger area onto the small cell. Those types of cells usually require solar-tracking systems. Comparatively the cost of materials becomes negligible; it is in reducing the cost of optics and mechanical parts that savings can occur, as well as in improved efficiency.

In between, we find a variety of technologies, all of which offer different trade-offs: thin-film silicon cells became extremely popular in the past few years as the cost of silicon increased, and reducing cost of materials became a main priority. Depositing thin films on top of a glass substrate was more cost-effective than plain silicon wafers, while it also offered new possibilities for much larger cells, and even flexible substrates. Unfortunately the thin-film silicon revolution was short-lived as prices of bulk silicon dropped, thanks to the push of the major producers to increase production and lower costs.

The thin-film effort, however, was not in vain, for many of the latest technologies involve thin-film coatings.

Cadmium telluride (CdTe) has become one of the most popular materials thanks to the ability of FirstSolar to mass-produce this type of thin-film cells at a lower cost per watt than that of silicon based cells. This results, however, at the expense of toxicity, cadmium being a

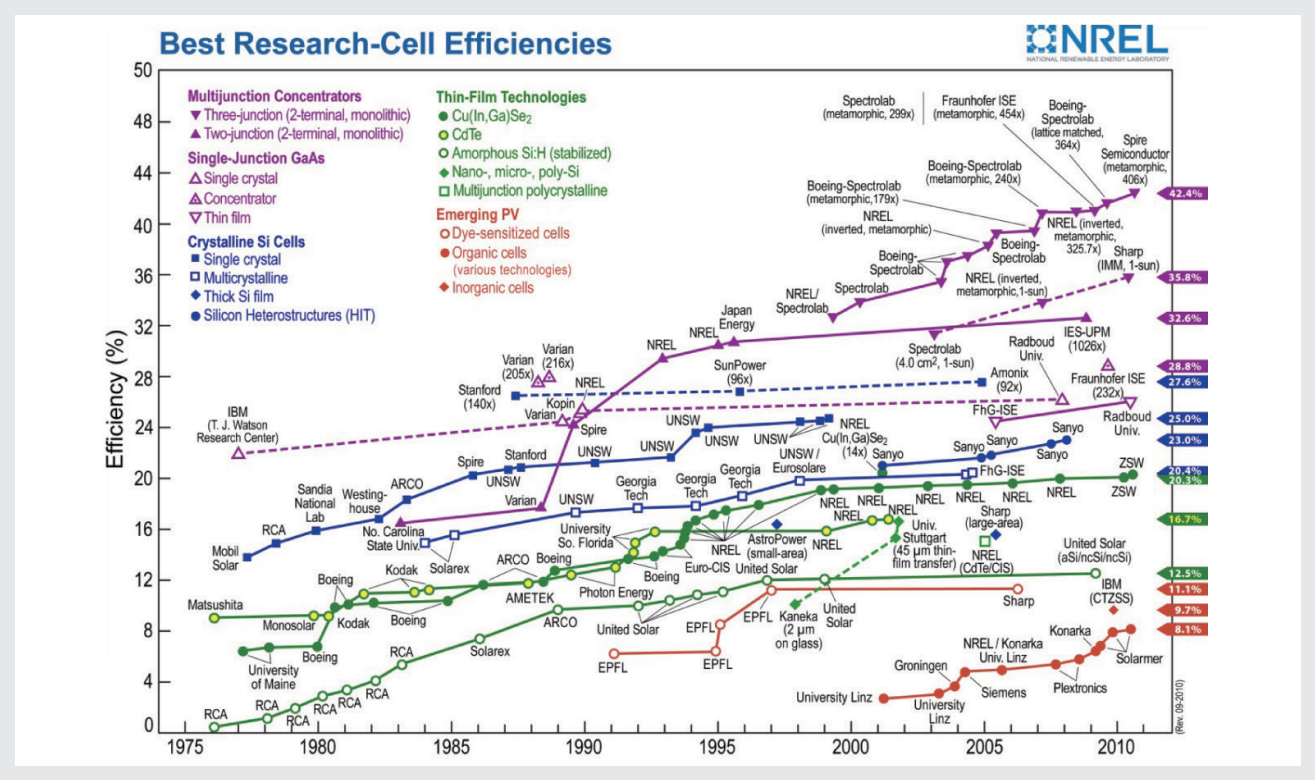

Figure 1 Include a caption for the figure, in the following format: Figure 1. Growth of cell efficiency with time. Refer to Figure 1 in the text. I am not sure where you actually discuss this graph directly in the text, however. If you don't, please add a sentence or two in the text itself with a reference to this graph.

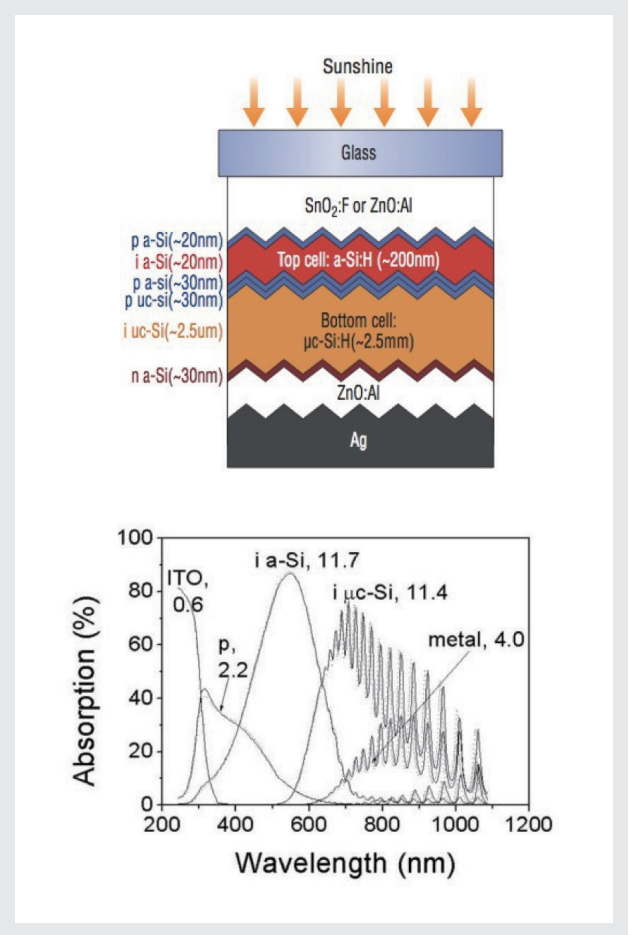

Figure 2 Up: Structure of a multi-junction cell. Down: Absorption of a multi-junction cell vs. wavelength.

well-known health hazard, which implies producing with recycling in mind.

Copper indium gallium di-selenide ($CuInGaSe_2$ or CIGS) seems to have now proven as efficient, if not more efficient, than multi-crystalline silicon, and enormous efforts are made by large photovoltaic manufacturers to bring this technology to mass-production.

Some other exotic materials are also in use, but most research efforts are directed at improving efficiency of the current materials named above, to build cells that are capable of taking advantage of a broader spectral range. This is the reason for multi-junction cells. Also called tandem junction, or tandem cells, they are mostly produced using thin-film deposition methods to make the second- and third-generation photovoltaic cells—by stacking multiple cells that absorb light in overlapping spectral ranges—The final cell absorption spectrum is increased, therefore improving energy-conversion efficiency.

Finally, efforts based on organic materials are still in the research stage, with few commercial products available. These cells are typically of very low efficiency, and lifetime is a problem. However when they can be formulated for stability, this type of cell could bring the lowest manufacturing cost of all technologies, along with

very low installation costs (such as with adhesive rolls that could be applied to any surface).

Instrumentation from HORIBA Scientific in use in photovoltaic research and process control.

HORIBA Scientific offers a wide variety of instruments for material characterization, from elemental analysis to molecular analysis, to thin-film thickness, composition and interface characterization, as well as defect, purity and stress measurement. The basics of each technique are described below:

Ellipsometry

Ellipsometry is probably the most commonly used piece of instrumentation of all in the field of photovoltaic research and development. Ellipsometry is a light-based technique based on observing the change in polarization of a light beam as it is reflected at interfaces or refracted through a stack of films. The technique typically monitors phase and amplitude of the reflected beam, which translates into the parameters n, index of refraction, and k, dielectric constant. These parameters in turn, after fitting a model of the film stack, can provide information about the thickness of each film in the stack.

Spectroscopic ellipsometry uses a broad-band excitation source, as opposed to a single wavelength, so that more information can be extracted from the measured data, such as variation in composition, surface roughness or stress.

HORIBA Scientific's Spectroscopic Ellipsometers (SE) use a unique design (see Figure 3) based on an electro-optical element called a photoelastic modulator (PEM), which allows ultra fast data-acquisition rates with no moving parts, resulting in averaging of many more data points, low noise and the best detection limit on the market.

Ellipsometry is best suited for thin films ranging from a few Angstroms to a few microns thick.

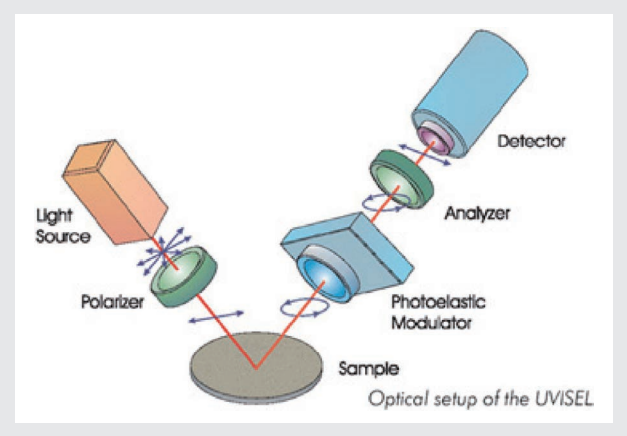

Figure 3 Schematic of a HORIBA Scientific spectroscopic ellipsometer.

Glow Discharge

Glow Discharge is a plasma-based elemental analysis technique consisting in sputtering a piece of material to eject one atomic layer at a time, which, when ejected, gets excited in the plasma to emit photons at wavelengths specific to each atom. The emitted light is collected and sent to a polychromator, which disperses the different wavelength towards discrete high-speed photomultiplier (PMT) detectors.This technique is destructive, for the atoms are extracted from the sample; however, it only requires local vacuum and no special sample-preparation, which is much more convenient than similar techniques like Secondary Ion Mass Spectroscopy (SIMS) and comes at a much lower cost.

The Glow Discharge GD Profiler is especially useful for rapid depth-profile analysis of multi-layer multi-element films of variable thicknesses from nanometers to several dozen microns. The very high speed and high dynamic range of the PMT detectors allow measurement of relative composition from 100% down to the parts-per-million (ppm) level.

Energy Dispersive X-Ray Fluorescence (ED-XRF)

X-Ray Fluorescence is a non-destructive elemental-analysis technique using a parallel x-ray beam as a source projected onto the material to be analyzed (Figure 4). The x-ray bombardment causes electrons to be ejected from the atoms in the materials, which are quickly replaced by electrons from higher electronic shells, emitting photons in the x-ray spectral region as they

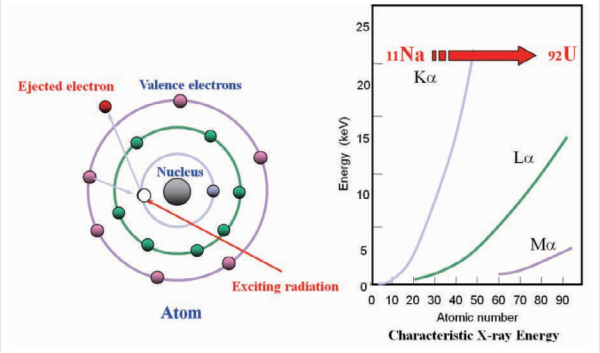

Figure 4 How ED-XRF works. Left: Exciting radiation ejects a K-shell (inner) electron. Right: Shift of inner-shell ejected-electron energies with atomic number.

decay.

A silicon-based energy dispersive detector (EDS) collects the emitted x-ray wavelength.

An EDS detector contains a crystal that absorbs the energy of incoming x-rays by ionization, yielding free electrons in the crystal that become conductive and produce an electrical charge bias. The x-ray absorption thus converts the energy of individual x-rays into electrical voltages of proportional size; the electrical pulses correspond to the characteristic x-rays of the element.

Only local vacuum around the detector is required for most elements, so the technique is very fast and convenient, requiring no sample preparation.

HORIBA's guide-tube technology used in the XGT system series provides a unique way to concentrate high-energy x-rays into a small spot for high spatial resolution, while keeping a parallel beam, which eliminates the need to focus the beam precisely.

EMGA Oxygen/Nitrogen analyzer

EMGA is used to determine very low concentrations of oxygen or nitrogen in materials. The sample is placed in a graphite crucible, and the crucible is supported between the upper and the lower electrode of the impulse furnace. A very high current is passed through the crucible to bring the sample to very high temperature. (See Figure 5.)

In the sample, the oxide that reacts with the graphite crucible is extracted as carbon monoxide (CO), and flows through a dust filter to the analyzer with a carrier gas. The oxygen concentration is determined by CO analysis

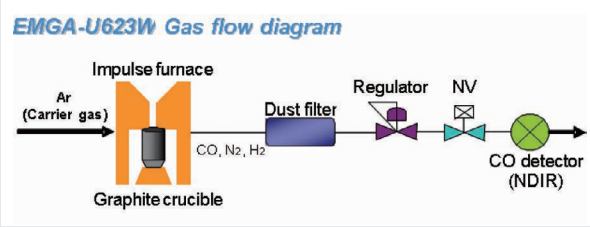

Figure 5 Schematic of an EMGA analyzer. Argon, the carrier gas, carries gaseous analytes frp, the crucible through filtration to a CO detector.

with a non-dispersive infrared analyser (NDIR).

Raman Spectroscopy

Raman spectroscopy is a vibrational spectroscopy technique that provides information on molecular bonds and their local environment, which helps determine chemical composition and properties. It typically consists of using a continuous-wave single-wavelength laser to excite the chemical bonds within a sample. Starting from a ground state, a bond can be brought to a virtual vibrational state, and either return to the ground state or be excited up to a higher real vibrational state. When returning to the ground state, there is no energy change, and the scattered light is the same wavelength as the laser. This is called Rayleigh scattering, and is the most common phenomenon. However, if the bond drops down to a different vibrational state, it will have absorbed some energy from the excitation laser beam, and scatter light at a different wavelength, offset from the laser by a value specific to the molecular bond. This effect is called Raman scattering. (See Figure 6.)

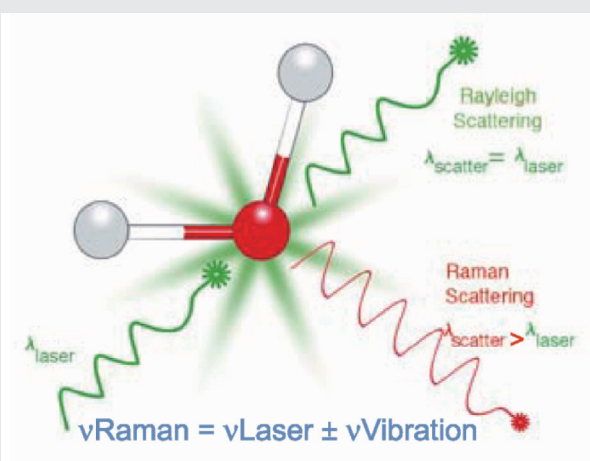

Figure 6 How Raman spectroscopy works. The source wavelength (green) excites a molecule, causing Rayleigh and Raman scattering (see text for details).

Because each possible molecular-bond vibration (also called mode) has a specific energy shift, Raman scattering provides a "fingerprint" of the bonds present in the

molecule, and allows identification of complex molecules as well as differentiation of closely-related polymorphs, of phases of the same material, or stress and defects in ordered structures.

Because it is a light-based technique, it is non-contact, non-destructive, and is the ideal technique for process control or quality control.

Photoluminescence spectroscopy

Photoluminescence is a type of fluorescence (which is a process in which a substance absorbs photons and then re-radiates photons). This can be described as an excitation to a higher energy state and then a return to a lower energy state accompanied by the emission of a photon. The period between absorption and emission is typically extremely short, in the order of 10 nanoseconds. Under special circumstances, however, this period can be extended into minutes or hours. Ultimately, available energy states and allowed transitions between states (and therefore wavelengths of light preferentially absorbed and emitted) are determined by the rules of quantum mechanics. Photoluminescence is usually observed using a single wavelength for excitation, so it is very similar to the Raman hardware configuration, which makes it possible to do with the same equipment.

Photoluminescence provides information on possible electronic transitions, which is directly related to the ability to convert energy from electron to photons, and back.

Applications

In order to improve cell efficiency, the photovoltaic research community needs tools to analyze characteristics of the materials developed, and understand the mechanisms involved in producing a successful prototype. For the industry, the challenge is to find ways to mass-produce cells with characteristics as close to the prototype as possible, using cheap manufacturing techniques. Since producing a cell requires many steps, from substrate to absorbing layer to contacts layer and protective layers, and it is critical to minimize costs, unsatisfactory products need to be rejected as early as possible. Process monitoring and quality-control tools are important to insure high yields.

Some common applications of HORIBA Scientific instruments are presented below, which are not only popular but more and more critical to successful development and manufacturing of efficient cells.

Thin film thickness-measurement and depth-profiling (SE, GD-OES)

Layer-thickness measurement is one of the most common applications in the thin-film type of cells (Figure 7), because of specific cell-stack requirements for efficiency, or more often for material cost-savings.

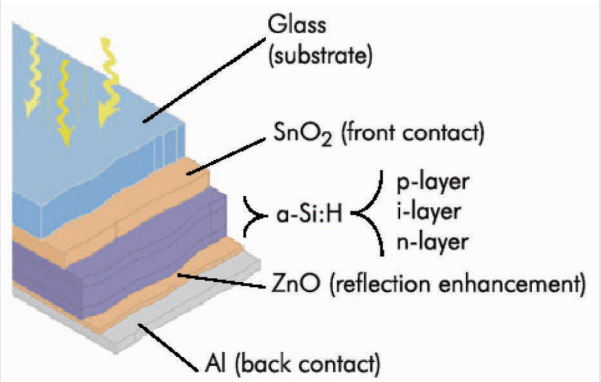

Figure 7 Multiple layers in a thin-film cell, all of which need to be characterized.

Spectroscopic Ellipsometry (SE) is particularly effective on very thin layers, and is the only technique for monitoring layers in the Angstrom-to-nanometer thickness range, as well as for monitoring complex stacks in one measurement. Because it is a non-contact and non-destructive method, it is well suited for quality control, either inline or at-line, or even in-situ within a process chamber, for real-time monitoring of layer deposition.

This monitoring method applies to silicon thin films, as well as CdTe, CIS and CIGS materials, which are all thin-film technologies, although they require different detection ranges. It also applies to the other layers such as TCO (transparent conductive oxides) used as electrodes, and polymer-based thin films.

Sometimes, however, layers are too thick to be easily analyzed by ellipsometry, which can then only characterize the top of the stack. Other techniques are required to generate a profile of the whole stack.

Glow Discharge Optical Emission Spectroscopy (GD-OES) has proven an efficient technique much cheaper and

faster than SIMS or other methods, to probe a full stack of films, obtain layer thickness down to a few nanometers, as well as provide elemental composition of each layer, with an accurate representation of the depth location of each element in the stack, which also provides information about how certain layers may diffuse into others as the materials are deposited.

Unfortunately, GD-OES is a destructive technique and only allows monitoring on sample test-cells, or on a test pad on the cell, which becomes inactive after measurement; yet it is still a very important technique with no equal on the market.

CIGS Bulk Composition measurement (XRF, GD-OES)

While ideally one would want to know thickness, composition, and phase of each layer in a film stack, it was explained above that this is not possible with a single technique. Spectroscopic ellipsometry provides thickness measurements down to a certain depth, but requires a model that assumes composition is known. GD-OES profiling provides elemental composition across the depth of the whole film stack, but is a destructive method not well-suited for online monitoring. GD-OES can also be used as a bulk analysis tool to provide very accurate elemental analysis, most useful for development and process development, but again not well-suited for process control.

X-ray fluorescence is another elemental-analysis technique which, as opposed to GD-OES, is non-contact and non-destructive, and does not require any sample preparation. X-ray fluorescence can provide bulk elemental analysis, which gives a good indication of the layers' composition, an important parameter to track.

Bulk-composition monitoring with XRF provides qualitative information as well as the relative composition of the film stack. Looking at the film of interest, relative elemental concentration can give an idea of the phase as well, although it cannot confirm this information, and values may be the result of the observation of different phases, which average out to the observed value over the probed area. In the case of CIGS films (copper indium gallium di-selenide), the phase of selenide is critical to the efficiency of the cell. Raman spectroscopy is a better way to observe and confirm phase.

Crystallinity, phase and surface-composition measurement (Raman)

As stated above, it is critical to control the phase of the diselenide in CIGS thin-film solar cells. Raman spectroscopy is the ideal tool for this application, with one main drawback: the shallow penetration-depth of most laser wavelengths into the CIGS material. Nevertheless, Raman spectroscopy is often used for process development as well as process monitoring in CIGS solar fabs but limited to surface-composition measurement.

By monitoring the position of the A1 peak of $CuInSe_2$, it is possible to get the stoichiometry ratio of Ga/GaIn, while any change in the spectrum shape and relative peak-intensity is an indication of the change of phase of indium or selenide. (See Figure 8.)

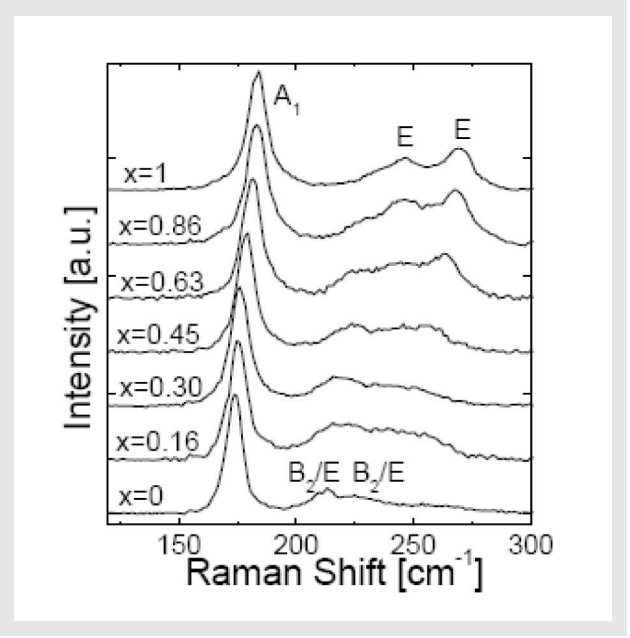

Figure 8 Example of Raman-peak shift with depth of analyte in a thin-film Cell.

Tracking the peak position requires fairly high resolution, which is one of the strong products of HORIBA Scientific instruments.

Raman spectroscopy is also a useful technique for silicon-based thin-film solar cells. Silicon is one of the most studied materials via Raman spectroscopy, and there is a tremendous amount of literature about silicon's different forms. Raman spectroscopy can easily determine crystalline phase as well as determine the stoichiometry of mixtures, as is the case in silicon thin films that typically incorporate crystalline silicon, micro-crystalline silicon, poly-crystalline silicon, and/or amorphous silicon (Figure 9).

Raman spectroscopy can probe up to a few microns deep, which is generally enough for most thin-film stacks that are more likely to be on the order of a few hundred nanometers thick.

Bandgap and defects (SE, PL)

One other important parameter that solar-cell researchers and manufacturers alike want to monitor is the bandgap, which gives a good indication of the material's ability to convert photon energy into electrons. Photoluminescence is the most common way to measure bandgap, and it is a very simple measurement, only made more difficult due to the fact that the emission is typically in the lower IR range (950-1600 nm) which requires an IR detector as opposed to a CCD detector.

The measurement is, however, feasible on the same platform used for Raman.

Photoluminescence is also an excellent tool to examine defects across a wafer, because defects reduce recombination, causing a sharp drop in the photoluminescence signal intensity. Wafer photoluminescence-mapping provides both the bandgap and defect information.

Bandgap can also be derived from the fitted model when using spectroscopic ellipsometry, for it is closely linked to the n and k coefficients, and can be determined by scanning across a large range of wavelengths.

Future materials, future applications, and conclusion

The advancement of tandem structures and multi-junction cells, as well as new techniques such as surface texturing, bring new challenges for metrology, but HORIBA Scientific instruments , of course, are applicable to those new challenges.

Tandem/multi-junction cells

Tandem or multi-junction cells consist of different materials, or different forms of the same materials (in the case of Si) in order to promote absorption of photons from a large wavelength range, so as to cover a larger portion of the visible spectrum. That implies more layers and thicker cells, which make modeling more complex for spectroscopic ellipsometry, yet this is where the best detection limit on the market becomes indispensable.

Absorption enhancement surface coatings

Texturing has been researched and integrated into the regular silicon solar-cell processes in order to enhance absorption. This type of coating brings thin-film technology to the standard bulk silicon wafer manufacturers, and is a new opportunity for thin-film metrology tools.

Organic materials and particle-embedded polymers

Finally, much has to be developed in order to produce cost-effective polymer-based photovoltaic cells. New research involving nanoparticle doping also brings new challenges, and may require technologies such as Raman spectroscopy to further investigate the possibilities these materials can offer.

In conclusion, the number of photovoltaic research facilities and the number of researchers getting involved in this field is constantly growing, while the need for quality control and process-monitoring equipment increases with the requirement to produce efficient cells and consistent quality, so that there are still many opportunities to come for HORIBA Scientific products in this field.

One of the keys to success, though, consists of the ability to support customers as the technology and the associated metrology requirements move from the lab to the fab.

Emmanuel Leroy

Raman Development Manager
Scientific Molecular and Micro-Analysis Division
HORIBA Jobin Yvon Inc.

Feature Article

Water Quality Measurements with HORIBA Jobin Yvon Fluorescence Instrumentation

Adam M. Gilmore

Water quality is one of the most significant global environmental concerns, making it one of the most important areas of research for HORIBA's fluorescence instruments. This article describes how our Fluorolog and FluoroMax spectrofluorometers and FluorEssence analysis software facilitate sensitive identification and quantification of natural and man-made sources of colored dissolved organic matter (CDOM) components important to water quality. The article focuses on the method of excitation-emission mapping (EEM) which simultaneously measures the excitation (absorbance) and emission spectra for all fluorescent components in a water sample. The article emphasizes the most important aspect of the EEM method, which is the accurate correction of both the instrument's spectral response and the influence of the light-absorbance properties of the sample as required for component identification and quantification. The future of water-quality fluorescence analysis is discussed in light of recognized potential applications and recent efforts to institute international standards for EEM methodology.

Introduction

Due to the increasing shortages of fresh, unpolluted drinking and irrigation water resources and pollution of the oceans globally, the analysis of colored dissolved organic matter (CDOM) is a key research area of international significance. Analysis of the often dilute and complex mixtures of CDOM components in water is made much easier using fluorescence technology, because it can yield parts-per-billion (ppb) sensitivity for many organic compounds and it is relatively inexpensive, simple to use, and nondestructive in nature compared to other techniques currently employed.

Fluorescent CDOM can comprise both natural and man-made components[1]. The natural components primarily consist of decomposition products of plant and animal materials, including humic and fulvic acids, proteins, and aromatic amino-acid constituents. Man-made fluorescent components can include petroleum products, fertilizers, pesticides, herbicides, sewage, pharmaceuticals, and—of increasing concern—toxic nanomaterials. CDOM influences natural bodies of water in several ways. Two of the primary effects are on the absorbance and light penetration-depth and on the oxygen demand (both biological and chemical), both of which are vital to sustaining life in water. CDOM is directly related to the oxygen demand, and hence viability, of natural water bodies because it consumes oxygen upon photodegradation, especially under the influence of UV light exposure.

The most common CDOM fluorescence-measurement technique is known as the excitation-emission map or EEM.[1, 2] An EEM is acquired by scanning the excitation (absorbance) spectrum of the sample while simultaneously acquiring the fluorescence emission spectrum at each excitation wavelength coordinate. The EEM is important for CDOM analysis because, in contrast to a typical two-dimensional absorbance scan of a water sample, the EEM exhibits a third dimension to provide both the absorbance and emission spectra of all fluorescent components. Thus an EEM strongly increases selectivity and potentially facilitates not only qualitative but quantitative analysis of all the samples' components.

One challenge in using fluorescence to analyze these samples is that, in most CDOM samples, the fluorescence

spectral components can exhibit significant overlapping features. Current methodologies to separate, identify and quantify the components have focused on conventional non-linear least-squares spectral deconvolution as well as a variety of multivariate techniques.[1-6] The latter multivariate methods include, among others, Partial Least Squares (PLS), Principal Component Analysis (PCA), and the recently popularized Parallel Factor Analysis or PARAFAC method, which we focus on in this review.

The key issues surrounding analysis of the EEMs with PARAFAC are the importance of reproducible and accurate spectral and instrumental correction of the data.[1, 2, 6, 7, 9] A major required spectral-correction method discussed below involves the coordinated evaluation of the absorbance spectrum of the sample in order to correct for the optical processes known as "inner-filter effects" (IFEs).[10-13] IFEs manifest in concentrated CDOM samples as both absorbance of the excitation beam (primary inner filter effect), and also sample fluoresence signals (secondary inner-filter effect), where the absorbance spectra and emission spectral regions of components overlap. IFE correction is significant in light of its role in referencing spectral libraries.

In most CDOM analyses, component identification is based on a public or privately-generated spectral library. Obviously, both intra- and interlaboratory comparisons must rely on traceable and reproducible spectral-correction procedures for the identifications to be validated.[8] This is of great concern given the diversity of instruments and conditions under which EEMs are reported in the literature for CDOM. Hence the final section of this article outlines our view of the future of fluorescent CDOM measurement for both research and analytical applications with regard to several prominent international efforts to standardize the EEM methodology.

A Focus on HORIBA's Fluorescence Instrumentation for Water Quality: The Fluorolog-3 and FluoroMax-4

The Fluorolog-3 spectrofluorometer line is modular by design, and is popular for water-quality CDOM analysis primarily because it can be configured to exhibit the highest sensitivity (signal-to-noise ratios >10 000:1) and fastest EEM data-collection available, up to 100 times faster than a conventional off-the-shelf spectrofluorometer. The modular Fluorolog-3 and bench-top FluoroMax-4 employ all-reflective optics to eliminate chromatic aberrations associated with lens-based optics, which improves spectral accuracy. The Fluorolog-3 is, in fact, recognized as an industry standard for spectral accuracy, having been used by the National Institute of Standards to generate their current generation of solid-state fluorescence-standard reference materials for spectral correction.[7, 9]

The Fluorolog-3 as illustrated in Figure 1 is optimally configured for CDOM analysis using a UV-enhanced light source to excite many UV-absorbing CDOM components of interest. The configuration shown also makes measurements of turbid and solid samples easier by virtue of both the double-grating excitation monochromator, to remove stray light, and the sample compartment's switchable front-face viewing optics, for when the sample is too concentrated or turbid to use the

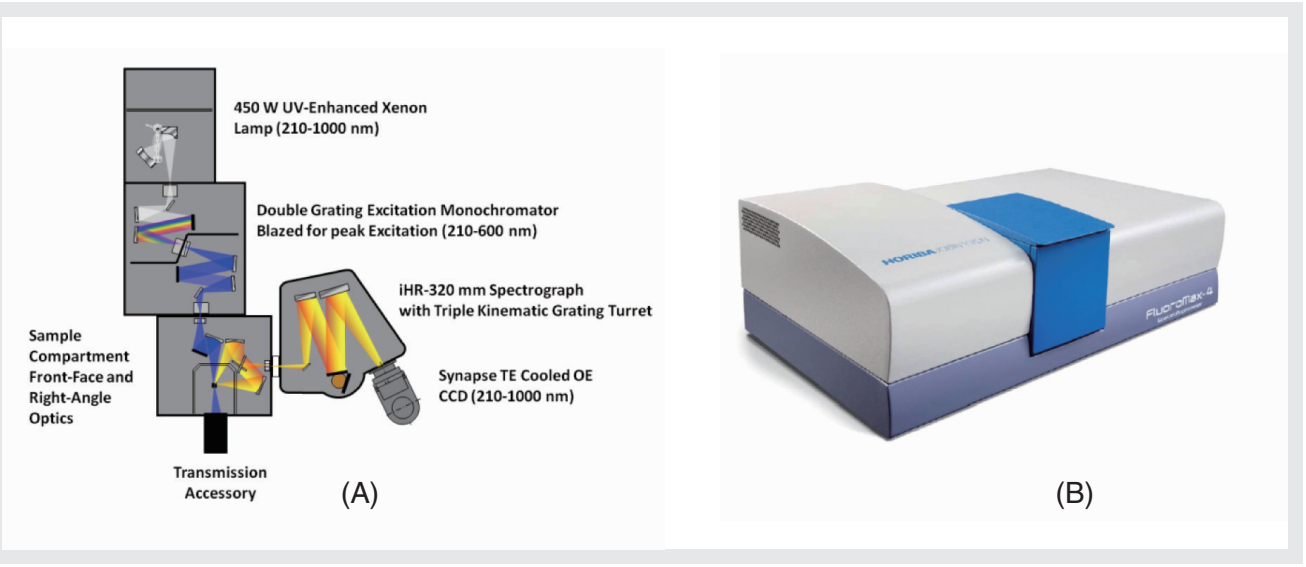

Figure 1 (A) The optical layout for a modular Fluorolog-3 configured for rapidly measuring excitation-emission maps of colored dissolved organic matter. (B) The bench-top, unitized Fluoromax-4 as an option for water quality labs requiring lower cost, less space and portability.

conventional 90-degree optical layout. Most important for the CDOM application, however, is the fact the Fluorolog-3 can be configured with a high-resolution 320 mm focal-length spectrograph (iHR 320) with a thermoelectrically-cooled CCD (Synapse-OE) detector, which enables EEM collection at rates faster than one per minute. Speed is important because many CDOM studies involve hundreds of EEM samples. The CCD provides an unrivaled multichannel signal-to-noise advantage compared to scanning monochromator single-channel-detector-based systems. A transmission detector can be added to the Fluorolog-3's sample compartment to record the sample's transmission/absorbance spectrum under the same spectral-bandpass and -resolution conditions as the fluorescence EEM data, which is required for accurate IFE corrections. Also critical, the Fluorolog-3 is equipped with a reference detector (R) to monitor and ratiometrically correct both the excitation source's spectrum for the emission detector and the absorbance detector's signals.

Whereas the Fluorolog-3 configured as above provides the fastest EEMs available, in some cases laboratory budgets and portability considerations preclude its use. In such cases the FluoroMax- 4 (Figure 1B) is a suitable choice for many CDOM laboratories because it exhibits the world's highest water-sensitivity rating for a benchtop fluorometer; it employs single-photon counting for ultimate sensitivity, is portable (often operated directly on ship), is fully corrected for the excitation source and instrument response, and also can come equipped with the transmission accessory needed for IFE correction.

An Overview of the Method of Excitation-Emission Mapping with Absorbance (IFE) Analysis of CDOM

As shown in Figure 2A a typical EEM for a CDOM sample involves scanning the excitation wavelength from 240-500 nm and acquiring the emission spectra from 250-600 nm. The spectral-bandpass and -resolution conditions are now generally accepted to be 5 nm by the research community.[8] Because the excitation axis is scanned and the excitation source exhibits wavelength-dependent intensity features, the emission detector signal must be divided by the respective excitation-source intensity monitored using the reference (R) detector at each excitation coordinate. Additionally both the R detector and emission (S) detector signals require correction for

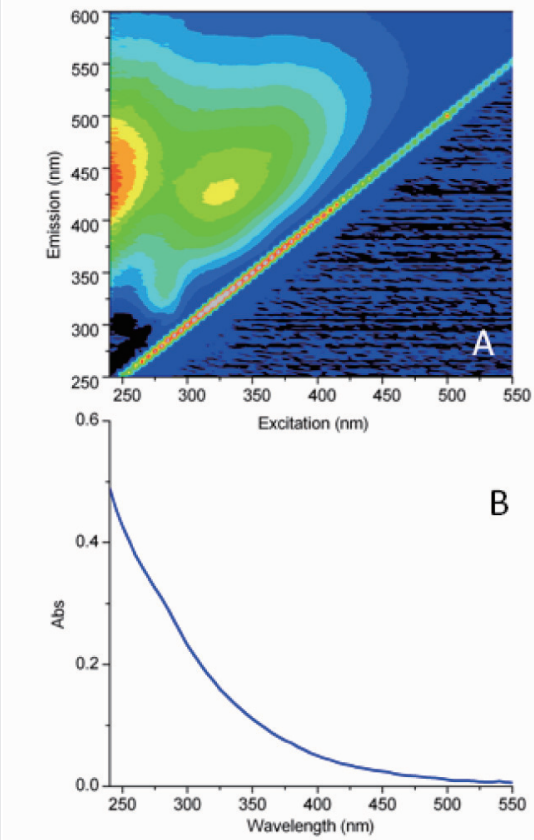

Figure 2 An excitation-emission map of the Pony Lake Fulvic Acid standard sample from the International Humic Substance Society (A). This map, and all maps shown below, were collected using 5 nm optical bandpass at 0.1 second integration time per emission spectrum. Panel B shows the absorbance spectrum of the sample shown in (A) measured under the same bandpass and integration time conditions.

the instrument's spectral responsivity, which conventionally includes subtracting the dark-current signal from each detector in addition to multiplying the R and S signals by their respective excitation (Xcorrect) and emission (Mcorrect) spectral correction factors. Hence, the final EEM signal is recorded in our FluorEssenc software using the general formula S_c/R_c where S_c = (S-dark) × Mcorrect and R_c=(R-dark) × Xcorrect. In conjunction to the EEM fluorescence signal, the sample's absorbance spectral data (Figure 2B) can be collected in parallel by measuring the transmission (A) detector signal formula $I = A_c/R_c$, where A_c= (A-dark) and R_c= (R-dark) × Xcorrect. To measure the absorbance spectrum of the sample, one must also measure the I_o= (A_c/R_c) of a blank or reference sample to calculate Abs = log (I_o/I) as a function of wavelength. The conventional reference or blank sample is usually highly purified water (≥18.2 MΩ, <2 ppb total organic carbon). Note that the blank sample can serve several additional purposes as described below

relative to correcting and processing the EEM data for qualitative and quantitative spectral analysis.

EEM Data Processing: Instrumental, Spectral and IFE Correction with FluorEssence Software

Figure 3A shows for a blank sample of ultra-pure water that the current practice for EEMs involves measuring the excitation and emission scan ranges, which includes their overlap regions. These overlap regions manifest in intense signals from the monochromated excitation source in the emission detector's response; these lines are caused by both the first- (and second-) order Rayleigh-scattering features consistent with the well-known grating equation. Figure 3A also shows another spectral feature, associated with the ultra-pure water sample, known as the water Raman scattering line. The Raman scattering line is related to the Rayleigh scattering line by a constant energy shift of 3382 cm^{-1}. Most CDOM component libraries contain spectra for which the artifactual Rayleigh and water Raman spectral features have been removed;, and hence EEM data must be processed to remove these features systematically. Figure 3B shows the raw EEM for a CDOM sample, namely an aliquot of a standard sample known as the Pony Lake Fulvic Acid (PLFA) sample provided by the International Humic Substance Society (IHSS). Here the main contours of the CDOM components are observed, along with the Rayleigh and Raman line scattering features. The FluorEssence software package can remove both artifacts. Figure 3C shows the result of subtracting the blank EEM data in Figure 3A from the CDOM sample data in Figure 3B, which effectively removes the Raman scatter line. Figure 3D shows the results of applying the Rayleigh-masking algorithm, which nullifies the signal intensities for both the first- and second-order Rayleigh lines. As mentioned above, the water Raman signal of ultra-pure water is often used to normalize the signal intensities of the CDOM sample EEMs; similarly many researchers choose to normalize the CDOM EEMs based on a unit of fluorescence from quinine sulfate (QSU).[1, 6, 12] Importantly, the FluorEssence EEM-processing software performs both the water Raman and QSU normalization.

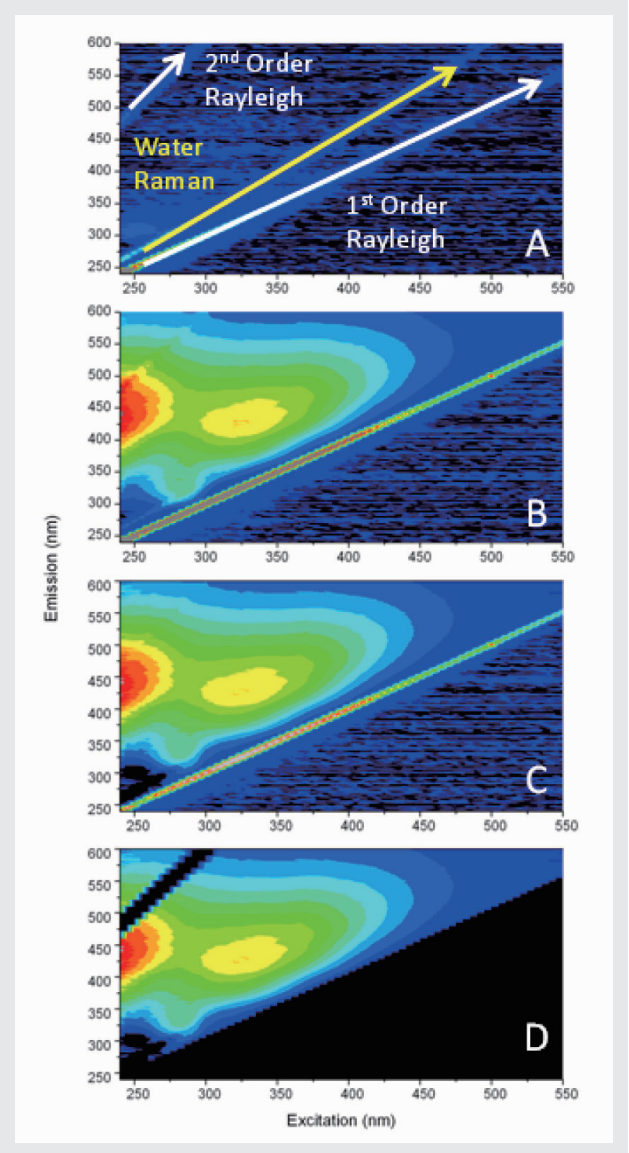

Figure 3 The fundamental instrument correction operations for processing an excitation emission map including blank subtraction and Rayleigh line nullification. (A) The excitation emission map of an ultra-pure water sample serving as the blank or reference sample showing the characteristic 1st and 2nd order Rayleigh scattering lines (white) and water Raman scattering line in yellow. (B) An uncorrected excitation-emission map of the Pony Lake Fulvic Acid standard sample. Panel C shows the result of subtracting the excitation-emission map data from the blank sample (A) from the sample in (B). Panel D shows the results of the algorithm that nullifies the 1st and 2nd order Rayleigh lines from the map shown in C.

In addition to the fundamental water Raman and Rayleigh correction procedures, it is common practice to correct the EEM data for IFE using the parallel absorbance measurements from the sample and blank as described above for Figure 2. The IFE algorithms used in FluorEssence require measuring the absorbance spectrum of the sample covering the overlapping range of both the excitation and emission spectra to correct for both the primary and secondary IFE. The most common IFE algorithm used for conventional 1 × 1 cm path-length cuvettes employs the following simple equation applied to each excitation-emission wavelength coordinate of the EEM[11]: $F_{ideal} = F_{obs}(10\text{^}(Abs_{Ex} + Abs_{Em})$, where F_{ideal} is the ideal fluorescence-signal spectrum expected in the absence of IFE, F_{obs} is the observed fluorescence signal, and Abs_{Ex} and Abs_{Em} are the measured absorbance values at the respective excitation and emission wavelength-coordinates of the EEM. A number of advanced

algorithms described in the literature can also account for variations of the optical geometrical parameters of the cuvette path-length, beam- or slit-width, and positioning/shifting of the cuvette relative to the excitation and emission beam paths.[10-13]

Figures 4A and B show a comparison of EEMs collected using both a concentrated ($Abs_{254\ nm} \approx 0.8$) PLFA sample to one diluted with ultra-pure water ($Abs_{254\ nm} \approx 0.2$) in Figures 4C and D. The absorbance value at 254 nm is an industry standard for evaluating the total CDOM concentration[8]. The EEMs on the left show the uncorrected (F_{obs}) while the EEMs on the right show the IFE corrected (F_{ideal}) for the corresponding samples. It is clear that for the uncorrected, higher-absorbing sample in Figure 4A that the spectral contours >300 nm on the excitation axis are stronger compared to the contours below 300 nm. This is because the IFE effects are strongest in the UV regions (below 300 nm) where the overlap of component excitation and emission spectra is largest. The IFE correction (Figure 4B) clearly reconstitutes the same contours seen with the dilute sample (Figure 4C) and the IFE correction had little effect on the dilute sample EEM in Figure 4D.

Likewise, Figure 5 shows in more detail the influence of the IFE corrections by comparing the absorbance spectra and the integrated excitation spectra of the PLFA EEM-data samples from a dilution series. Figure 5A shows the absorbance spectra for the PLFA dilution series which are particularly featureless with a quasi-exponential decrease from the UV to visible regions. Figure 5B shows the plot of the absorbance values at 254 nm from Figure 5A versus the dilution factor used in the experiment. The data in Figure 5B exhibit a highly significant linear trend up to the peak absorbance near Abs ≈ 0.8. Figure 5C shows that the F_{obs} for the integrated excitation spectra indicates there is a strong reduction in the intensity below

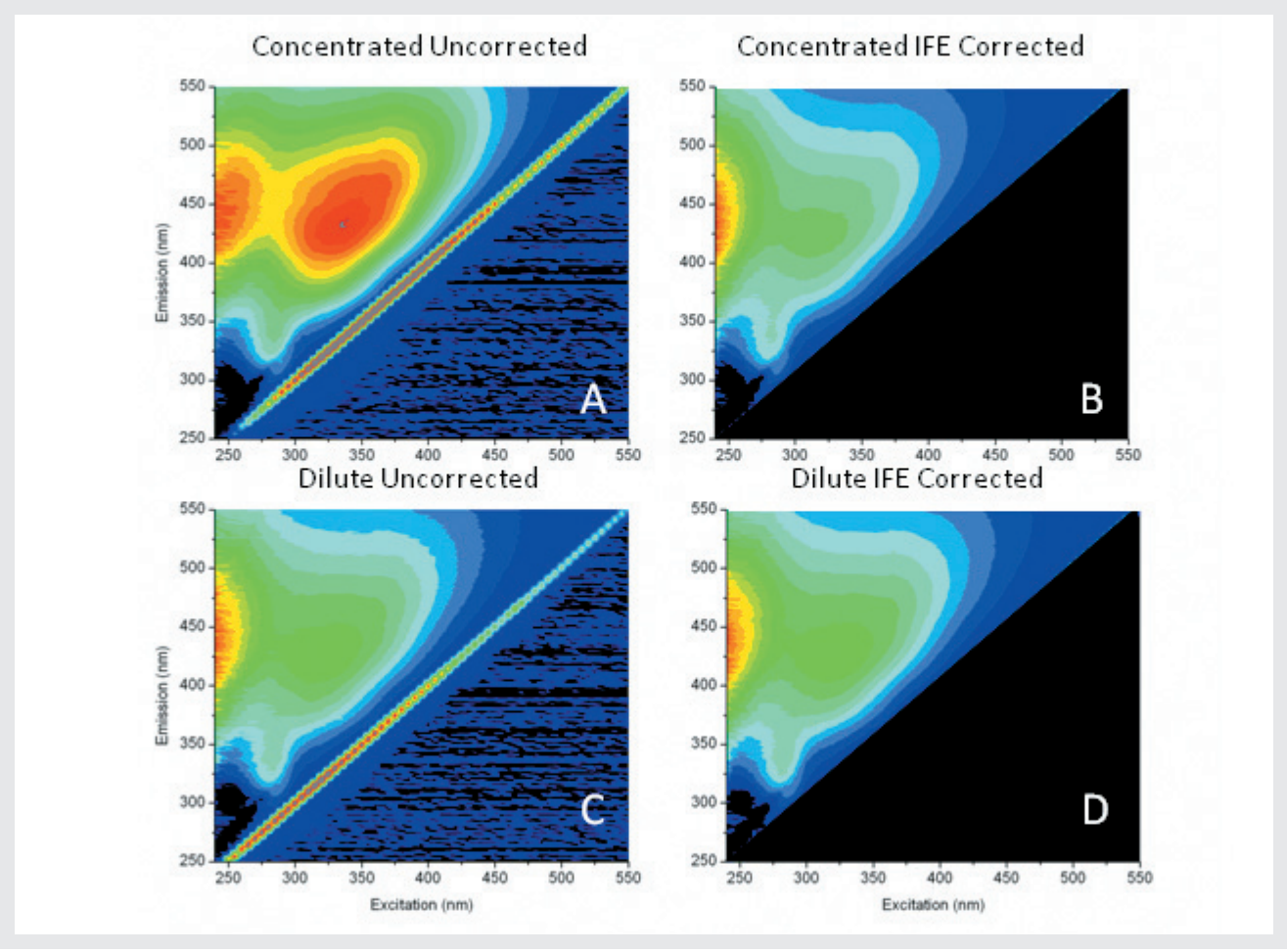

Figure 4 A comparison of the influence of the inner-filter correction algorithm on excitation-emission maps of concentrated (top row) and dilute (bottom row) samples of the Pony Lake Fulvic Acid standard sample. The uncorrected excitation emission-maps are shown in panels A and C the corrected maps are shown in B and D, respectively.

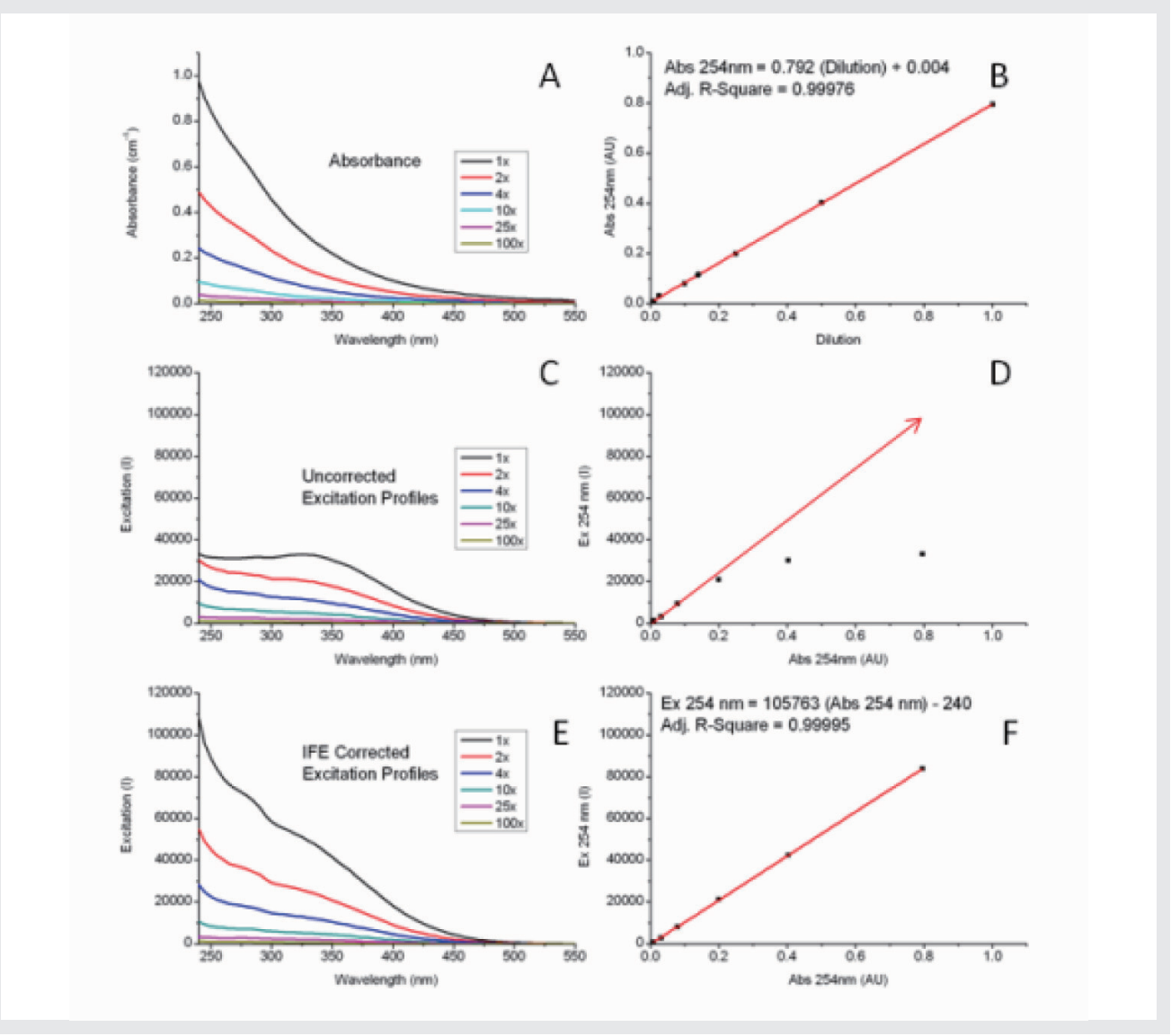

Figure 5 A comparison of the concentration dependence of the absorbance spectra (A and B) and the excitation spectra of the Pony Lake Fulvic Acid sample before (C and D) and after (E and F) inner-filter effect. The samples were diluted from full strength to 100 fold as indicated in the legends. Plots of the absorbance as a function of wavelength are in panel A and panel B show the linear relationship of the absorbance value at 254 nm and the dilution factor. Plots of the excitation spectra representing the integral of the excitation axis are shown in panel C as a function of wavelength. Panel D shows plots of the absorbance value at 254 nm against the excitation intensity value at 254 nm; the red arrow illustrates the nonlinear region above absorbance values >0.2. Panel E shows plots of the excitation spectra from (C) after inner-filter correction while (D) shows the plot of the linear relationship between the excitation intensity at 254 nm and the absorbance at 254 nm.

400 nm. Figure 5D presents no correlation between the absorbance values at 254 nm (x-axis) and the excitation intensity values at 254 nm (y-axis) beyond Abs ≈ 0.2 due to the increasing IFE. However, as shown in Figure 5E, when the IFE is corrected as described above, excitation spectral intensity is recovered, closely paralleling the absorbance spectra (Figure 5A) for all sample. The highly significant linear relationship between the excitation intensity at 254 nm and the absorbance at 254 nm shown in Figure 5F confirms the validity of the IFE correction and its value for concentrated CDOM analysis, allowing comparison to dilute sample spectra.

Spectral Analysis and Component Identification: Conventional Nonlinear Least-Squares and Multivariate Approaches

As required by the CDOM research community, the concerted application of the instrumental spectral corrections, Rayleigh-line masking, water-Raman subtraction, Raman or QSU normalization and IFE correction are readily enabled by the EEM-processing tools in our FluorEssence software. As mentioned above, the purpose of the spectral corrections and EEM-processing is to make the identification and quantification of the CDOM components that are usually based on a

reference component library. Here we focus attention on a popular and promising library-based multivariate technique for CDOM analysis, namely, PARAFAC, which has been documented extensively by researchers including many using HORIBA's fluorescence instruments.[1, 3-5] Importantly the FluorEssence software offers direct access to a MatLab console for purposes of processing data using the PARAFAC tools in N-way Toolbox, a public-domain package especially developed for CDOM analysis.[4] The modeling advantages of PARAFAC center on its ability to simultaneously evaluate the EEM data as a matrix and to envelop multiple (often hundreds) of EEMs simultaneously for increased statistical significance.[3-5] PARAFAC has been successful at identifying a wide range of CDOM components including humic and fulvic acids, tryptophan- and tyrosine-like substances, quinones, several polycyclic aromatic hydrocarbons, and distinguishing microbial, marine and terrestrial CDOM sources. More importantly, PARAFAC has been used to diagnose trends in CDOM components as a function of several key chemical and physical parameters, including water-recycling-plant treatment stages, sewage dispersion, stream flow, and ocean and estuarial currents, among many others.[6] Indeed, as discussed below, the application of PARAFAC has been proposed as a standard modeling technique for a variety of water-quality applications.[1, 14]

Conclusion: The Future of Water-Quality Analysis Applications and Standardization by the International CDOM Community

Several key publications and international standards documents have recently been published regarding fluorescence-instrument calibration and correction, including EEM data, as well as those focusing on interlaboratory comparisons of CDOM EEM applications. Three recent publications from NIST researchers have particular significance for EEM correction, including a reference to the recently released ASTM standard guide (E2719) for fluorescence calibration and correction,[9] a reference to CDOM EEMs and all aspects of instrument and IFE correction,[2] and a reference to the validation of the Fluorolog as the true accurate fluorometer for its use in generating and validating a series of Standard Reference Materials.[7] Furthermore, a recent paper has been accepted outlining the results of a major international interlaboratory comparison for CDOM IHSS standard samples; this study was headed by researchers and the United States Geological Survey (USGS), and was the focused outcome of a recent 2008 Chapman conference sponsored by the American Geophysical Union.[8] In terms of potential applications of CDOM analysis two reviews of the literature exist of note, including one paper explaining the potential of CDOM for monitoring all stages of water recycling,[14] and another focusing on analysis of natural and wastewater sources.[1]

It is clear that fluorescence analysis of CDOM and the use of EEMs will play a central role in water-quality analysis in academic and government research, as well as for various municipal and industrial monitoring applications. HORIBA presently enjoys the recognition of the industry as the leader in both hardware and software for this application. It is our goal to continue to design instrumentation and software and to promote standardization and regulations that will increase the potential for fluorescence as a water-quality analysis tool, and thus help researchers trying to understand, prevent, and treat the consequences of CDOM contamination of our water—one of our most critical resources.

References

[1] Hudson, *et al*. (2007) Fluorescence analysis of dissolved organic matter in natural, waste and polluted waters-A Review. *River. Res. Applic*. **23**:631-649.

[2] Holbrook, *et al*. (2006) Excitation-emission matrix fluorescence spectroscopy for natural organic matter characterization: A quantitative evaluation of calibration and spectral correction procedures. *Appl. Spectroscopy* **60** (7), 791.

[3] Stedmon, C. A., S. Markager, and R. Bro. (2003) Tracing dissolved organic matter in aquatic environments using a new approach to fluorescence spectroscopy. *Mar. Chem*. **82**:239-254.

[4] Stedmon, C. A., S. Markager, and R. Bro. (2008) Characterizing dissolved organic matter fluorescence with parallel factor analysis: a tutorial. *Limnol. Oceanogr.: Methods* **6**:572-579.

[5] Cory, R. M., and D. M. McKnight (2005) Fluorescence spectroscopy reveals ubiquitous presence of oxidized and reduced quinones in dissolved organic matter. *Environ. Sci.Technol*. **39**:8142-8149.

[6] Cory, *et al*. (2010) Effect of instrument-specific response on the analysis of fulvic acid fluorescence spectra. *Limnol. Oceanogr.: Methods* **8**, 67-78.

[7] DeRose, *et al*. (2007) Qualification of a fluorescence spectrometer for measuring true fluorescence spectra. *Rev. Sci. Instr*. **78**, 033107.

[8] Murphy, *et al*. (2010) The measurement of dissolved organic matter fluorescence in aquatic environments: An interlaboratory comparison. *Environ. Sci. Technol*. (in press)

[9] Paul C. DeRose and Ute Resch-Genger (2010) Recommendations for Fluorescence Instrument Qualification: The New ASTM Standard Guide. *Anal. Chem*., **82**, 2129-2133.

[10] Qun Gu and Jonathan E. Kenny (2009) Improvement of Inner Filter Effect Correction Based on Determination of Effective Geometric Parameters Using a Conventional Fluorimeter. *Anal. Chem*. **81**, 420-426.

[11] Lakowicz, J. R. (2006) *Principles of Fluorescence Spectroscopy*, 3rd ed.; Springer Science and Business Media, LLC: New York.

[12] Tobias Larsson, Margareta Wedborg, and David Turner (2007) Correction of inner-filter effect in fluorescence excitation-emission matrix spectrometry using Raman scatter. *Anal. Chim. Acta* **583**, 357-363.

[13] B. C. MacDonald, S. J. Lvin, and H. Patterson (1997) Correction of fluorescence inner filter effects and the partitioning of pyrene to dissolved organic carbon. *Anal. Chim. Acta* **338**, 155.

[14] Henderson, et al. (2010) Fluorescence as a potential monitoring tool for recycled water systems: A review. *Water Research* **43**, 863.

Adam M. Gilmore

HORIBA Jobin Yvon Inc.
Ph. D.

Feature Article

Particle Characterization of Volcanic Ash by Dynamic Digital Image Analysis

Michael C. Pohl

Digital Image Analysis is one of the fastest growing methods for determining particle size and shape. The Dynamic version of this technique as seen in the HORIBA Camsizer-L is gaining in popularity very rapidly. This instrument has been applied to many fields including glass beads, fertilizer, expanded polymers and soils and sediments. The capability to determine size and shape in one measurement in five minutes or less is very attractive. A logical extension of the work on soils and sediments is to migrate to samples originating from volcanic eruptions. This article will explore the proper measurement of these samples and how the data can be used to construct plume dispersal models.

INTRODUCTION

When researchers use the term particle characterization, they are talking about all aspects of a particle or ensemble of particles. This would include size, shape, morphology, texture, transparency and many other characteristics. For several hundred years this type of data could only be derived from looking at microscopic images of the particles. Due to the slow, tedious nature of this measurement, other less direct measurement methods were developed. These include laser light scattering, sedimentation measurements, electrical sensing zone determinations, light obscuration and many other "indirect" methods. These methods produced data considerably faster but the typical result was expressed as an "Equivalent Spherical Diameter" as a single parameter.

The speed, and in some cases the availability Particle Size Distribution, made these newer methods more attractive, but a great deal of information got lost in these measurements. Due to this major limitation, the Optical Microscopy Method remained the "gold standard" to which all other methods were compared. During the last 50 or so years the existing methods were optimized and new ones developed to improve the correlation to the microscopic results. This drove these techniques to new levels of accuracy, repeatability and reproducibility. While this benefited a wide variety of industries, it did not overcome the fundamental problem which is the limited amount of information which the techniques produce.

The 1980's saw the advent of powerful computers which were able to automate the collection and analysis of raw images directly from the microscope. This greatly accelerated the capture of the data and its analysis while also greatly reducing the tedium of visually examining each and every particle. While this did accelerate the process, it was still requiring many minutes per analysis. This challenge originates from the need to scan around the microscope slide to different fields to look for individual particles. Even when this is done by a computer, it requires a long time. Eventually in the late 1990's this static image analysis approach began to be displaced by a dynamic image analysis approach which greatly accelerated this process. This approach presented a large number of particles to the camera simultaneously to greatly enhance the data collection capability.

THEORY: USEAGE OF PARTICLE CHARACTERIZATION DATA

The new approach is embodied in the Camsizer design shown in Figure 1. In this instrument the particles are

CAMSIZER is a compact laboratory instrument developed by RetschTechnology (http://retsch-technology.com). It uses two high resolution CCD camerasfor the simultaneous measurement of particle size distribution and particle shape of incoherent materials in the range of 30 µm to 30 mm. CAMSIZER bases on dynamic digital image processingand permits to obtain measurements of shape parameters on a highnumber of particles.

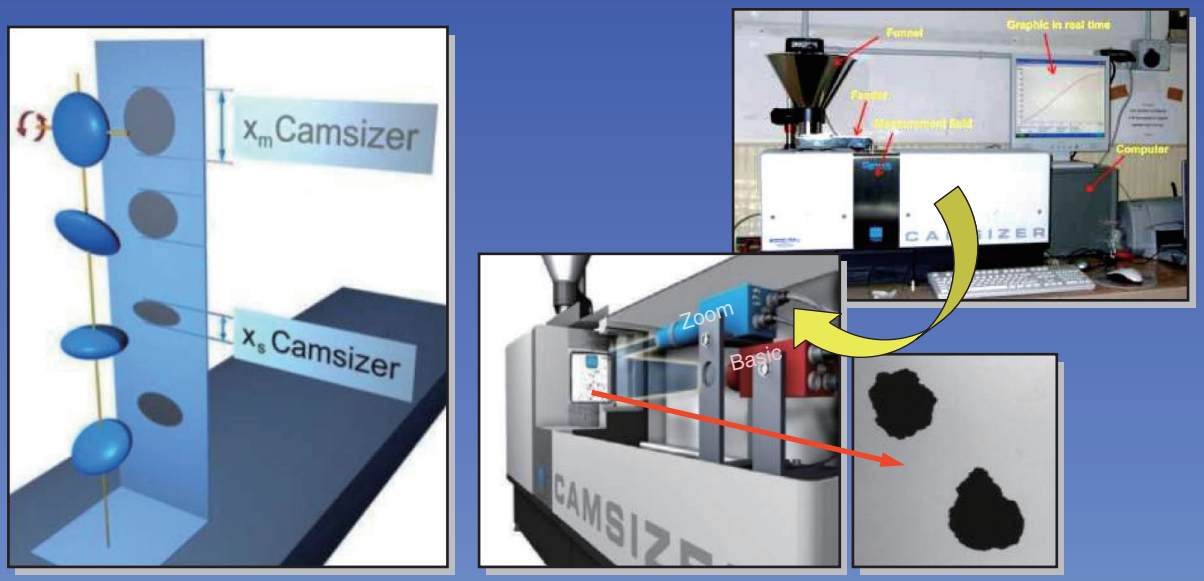

Figure 1 METHODOLOGY

fed at a controlled rate from a hopper to a vibrating chute. The chute vibrates the particles causing them to fall in front of the two cameras at a constant amount of obscuration. The two cameras simultaneously measure the size and shape of the particles as they fall. This patented two-camera system allows particles between 30 µm - 30 mm to be measured quickly and accurately. The instrument features a Basic Camera to measure larger particles and a Zoom Camera to measure the smaller ones. This product features very high counting statistics which produce stable, accurate results. Shape and size data is now readily available in what typically amounts to a 5 minute analysis.

Particle Characterization is a physical test which has some unique features as compared to other analytical methods. The actual raw data is interesting in its own right, but it must be correlated to another physical test in order to have any physical significance. A good example of this would be the determination of the hiding power of paint pigments. This is a very time consuming manual test performed by painting a panel with a pre-existing color, painting on a second color and optically determining the amount of color visible from the first coat of paint showing through the second. This hiding power is determined by the pigment particle size used to prepare the paint formulation. If the pigment size is determined and the correlation to the hiding power properly established, a several-day test is reduced to five minutes. This is an example of how Particle Sizing would be implemented in an industrial setting in order to predict final product performance.

An early application of the Camsizer was the determination of the size and shape of glass beads. One of the large uses for these beads is as a coating for the paint stripes on roads. In this application the beads are added to the paint striping to permit drivers to see the stripes at night, especially during rainy conditions. This property relating to light from car headlights striking the beads and being reflected back to the driver's eye is called retroreflectivity. There is an actual instrument which makes this measurement as a test vehicle moves along the striping and produces a retroreflectivity number. This is difficult and time-consuming to do on real roads especially in remote areas and so a physical test (particle size and shape) has been developed to replace it.

The new test consists of measuring the size and shape of a representative sample of the glass beads prior to their being introduced into the paint which is being sprayed onto the road. The key parameters determined are the

median bead size and the particle sphericity. These tests can be done for all types of commercial glass beads typically in five minutes or less. The correlation is that large, very round beads will have the highest possible retroreflectivity, which is the desired property. Thus, a laboratory based test of a lot of beads can accurately predict the behavior of the beads before it is shipped out to the state Departments of Transportations (DOT's) for the striping of the roads. All glass bead manufacturers and most state DOT's use this technology to specify the beads that will be accepted. The Camsizer has now become the de facto standard for this industry. An American Society for Testing and Metrials (ASTM) Method is expected to issue any day.

In the case of soil and sediment samples the size and shape of the particles is critical to determine where these materials will deposit in a lake, stream or ocean. These sedimentation issues are important as they relate to the dredging of harbors, the deposition of stream sediments in the ocean and the characteristics of materials at the bottom of lake beds. For many years sedimentation size measurements were the method of choice because the technique mimics the actual physical process. The limited applicability of this method to only silt and clay particles made alternative methods quite attractive. For many years the Camsizer has been used for making these measurements on the larger particles to predict the depositional patterns for the sediments.

MEASUREMENTS ON VOLCANIC ASH

It does not represent a huge technological stretch to apply this same approach to particles that are in the dry state in nature. In the case of soil and sediment measurements it is quite a bit more complicated due to the requirement to first dry and prepare the samples for analysis. The extension of the sample type has happened when soils and sediments were replaced by volcanic ash samples. A good example of this new application is illustrated in Figure 2 below. As is readily apparent these particles consist of a wide variety of sizes, shapes and colors of particles. This sort of a complex mixture is perfect to show the power of dynamic, digital image analysis. While the measurement is easy, some additional analytical techniques are required to properly use this information. These new adaptations are the basis for this article.

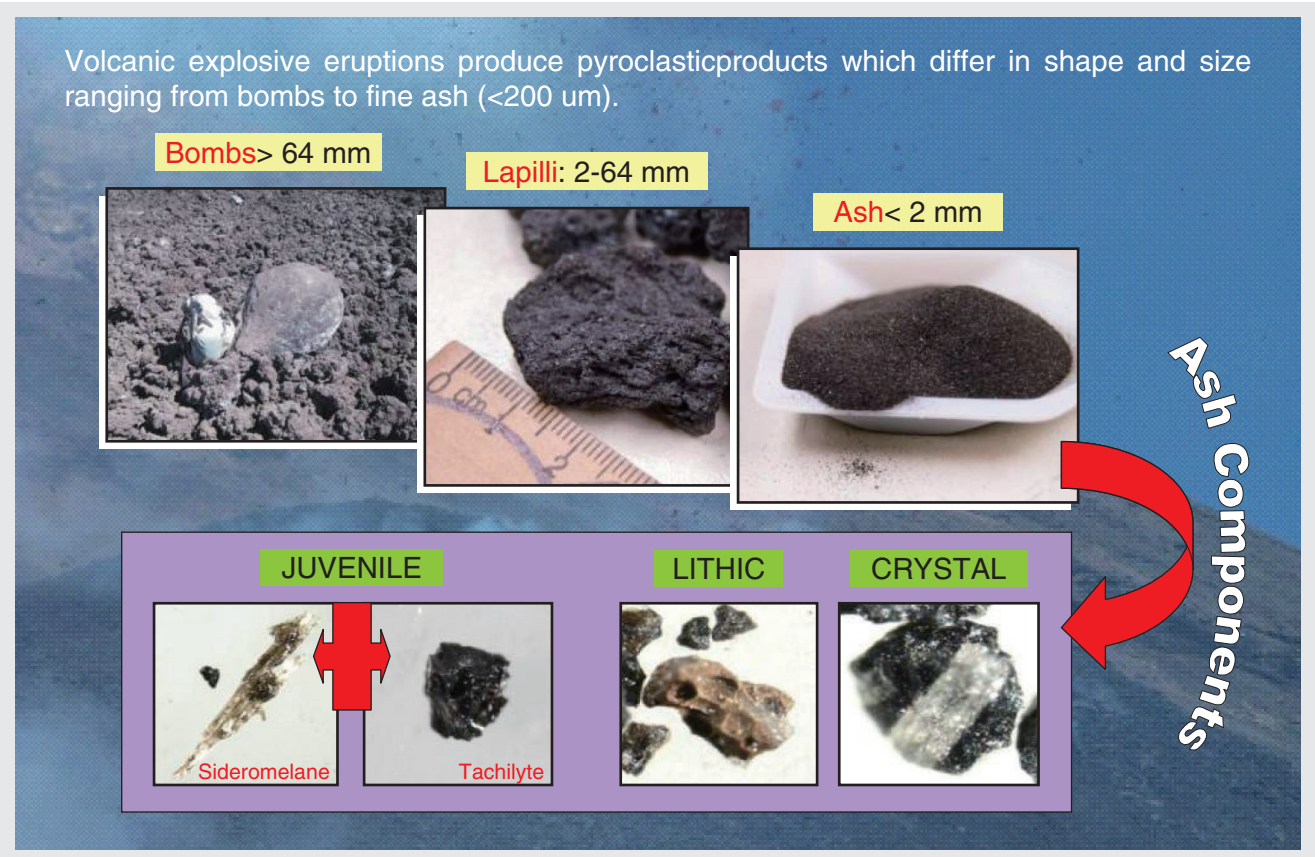

Figure 2 Volcanic particles: typologies and characteristics

The importance of this type of measurement is illustrated in Figure 3. The actual size and shape of the particles are determined by a number of characteristics of the volcano itself. Examples of these processes are shown on the left hand side of the figure. The study of these characteristics is outside the scope of this article. The effect that these particles have on the deposition of the plume is illustrated on the right side of the figure. In order to correctly predict this dispersal, the particles have to be correctly characterized and the results correlated to the settling rate. As indicated, the assumption that it is a collection of spherical particles that will behave according to Stokes' Law has no chance of succeeding. Thus, the challenge for the Camsizer is to produce results that will allow the models to correctly predict the plume dispersal.

RESULTS AND DISCUSSION

As Figure 2 illustrates, these Volcanic samples are composed of a wide variety of particle type, sizes, colors and shapes. When such a broad spectrum of types exists, the data generated has to be handled in a unique fashion. For this particular study it was decided to attempt to do a cluster analysis to identify some clusters of similar particles in the data in order to use them for the correlation properties. If a small number of clusters can be identified, then the characteristics of the cluster can replace the millions of individual particles. If everything works, the sum of all of the cluster properties should correlate to the physical property of interest. The methodology behind this analysis is shown in Figure 4. It is a well established procedure for complex mixtures of samples, but had to be analyzed with programs external to the Camsizer software. These additional programs are identified by name in Figure 4 above.

In this methodology the raw data from the Camsizer was put through programs to produce the Features Extraction. This approach correlates certain parameters, in this case particle shape parameters to cause the data to cluster in distinct regions. This serves to identify the proper shape features to evaluate. With these shape parameters identified, a cluster analysis is performed to find groupings of shapes that all appeared in the same quadrant of the graph. This permitts a few shape characteristics to replace a very large number of real particles that were studied. Since this was the first time to attempt this for volcanic types of particles, it was decided to first test it for known, well characterized geometrical shapes. This data simulation was first attempted with a mixture of cubes, spheres and cylinders.

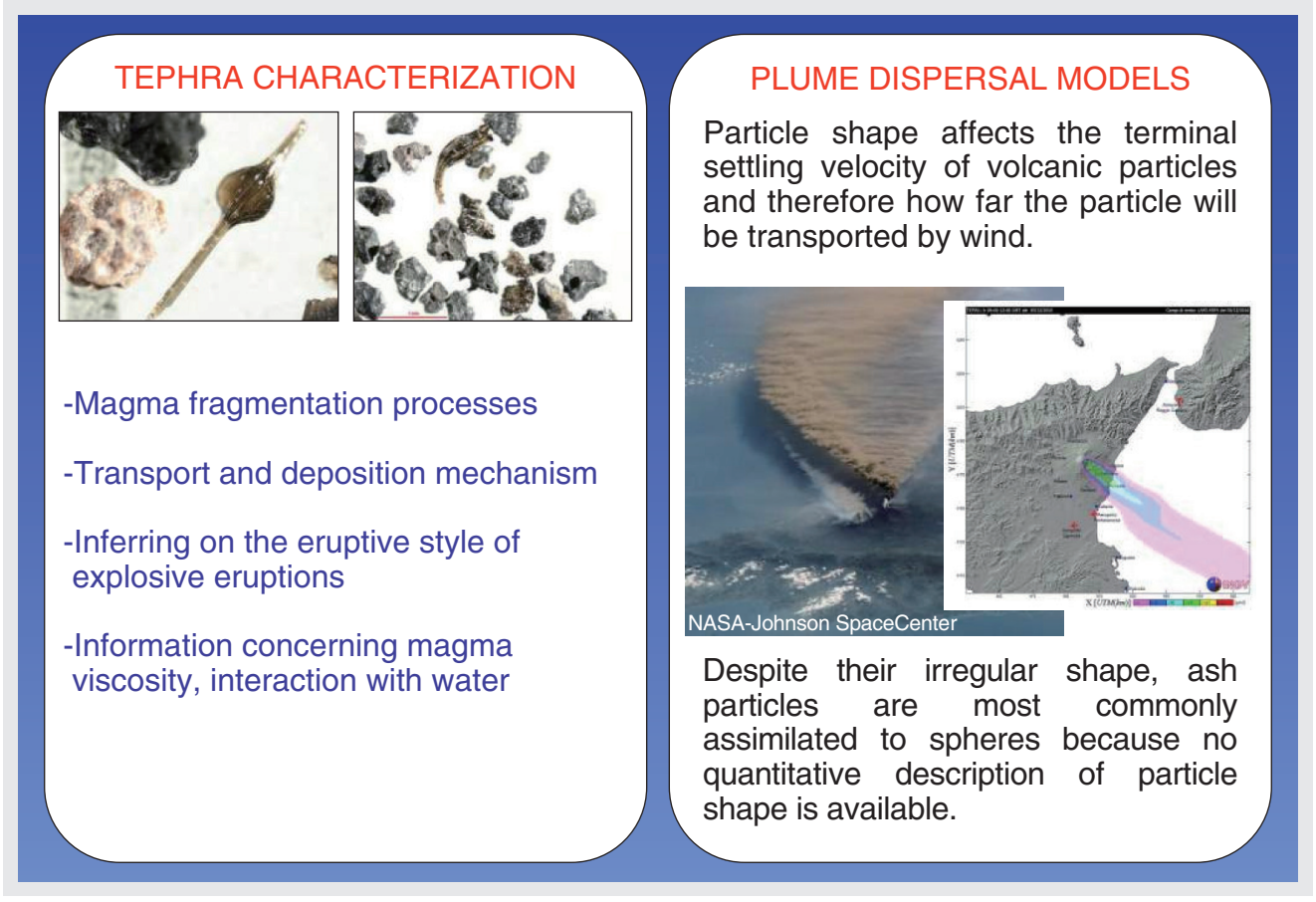

Figure 3 Importance of particle shape in volcanology

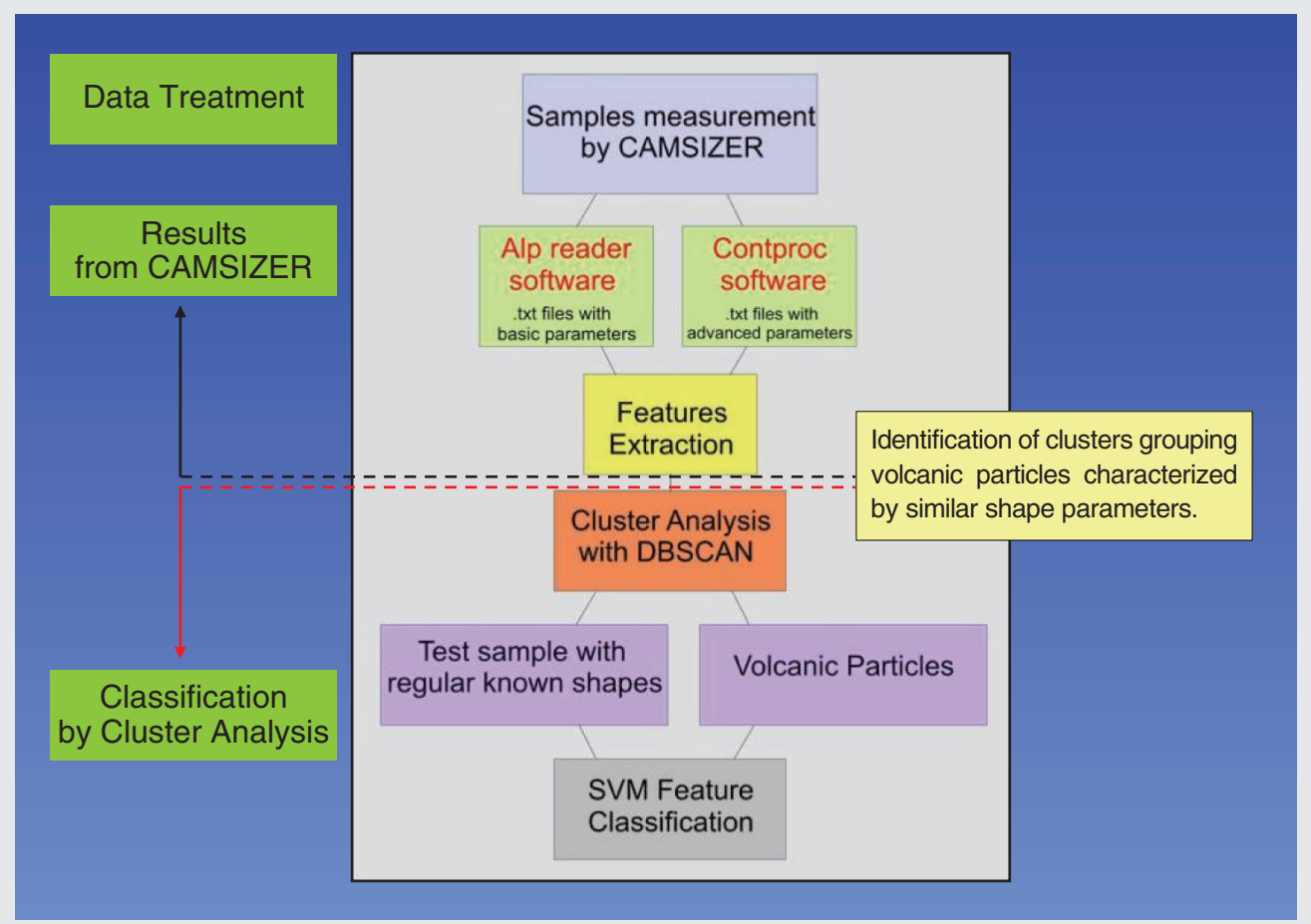

Figure 4

The results of this procedure is illustrated in Figure 5 below. In this theoretical study, three distinct shape characteristics were determined during the Features Extraction portion of the procedure. They were Sphericity (SPHT), b/l and Epol. These shape characteristics were assumed to be significantly enough different to distinguish between the three shapes that were arbitrarily mixed together. As the three dimensional plot indicates the various shapes do, in fact, cluster in different regions of space. By identifying the number of dots in each cluster, the numbers of particles of each type could be identified. Thus such an analysis could identify the precise number of particles of each shape. Since the aspect ratio of these particles is quite similar, the initial results were quite encouraging.

The next step was to attempt this type of analysis on actual volcanic samples. A number of these were performed on several different sets of samples obtained from two different volcanoes. In each case the samples were first sieved in order to restrict the analysis to similarly sized particles. This was necessary in order to remove the effect of the size of the particles on the shape that was being determined. For simplicity's sake, the plotting was reduced to two dimensions instead of three. Typical data from this procedure is shown in Figure 6 below for a lapilli sample from the Mount Etna volcano. This shows two quite distinct clusters of particle shapes for the real sample. The other samples showed very similar types of correlations as this illustration.

In this example for similarly sized particles the correlation was once again SPHT versus b/l. As can be seen the more spherical particles are clustered in the upper right hand corner while the more angular, irregularly shaped particles are clustered in the lower left hand corner. There is a small bit of overlap between the clusters, but the two groupings are very distinguishable from each other. This would indicate the general approach adopted in the study is valid for the samples which were investigated. It does, however, open up many additional issues requiring further investigation.

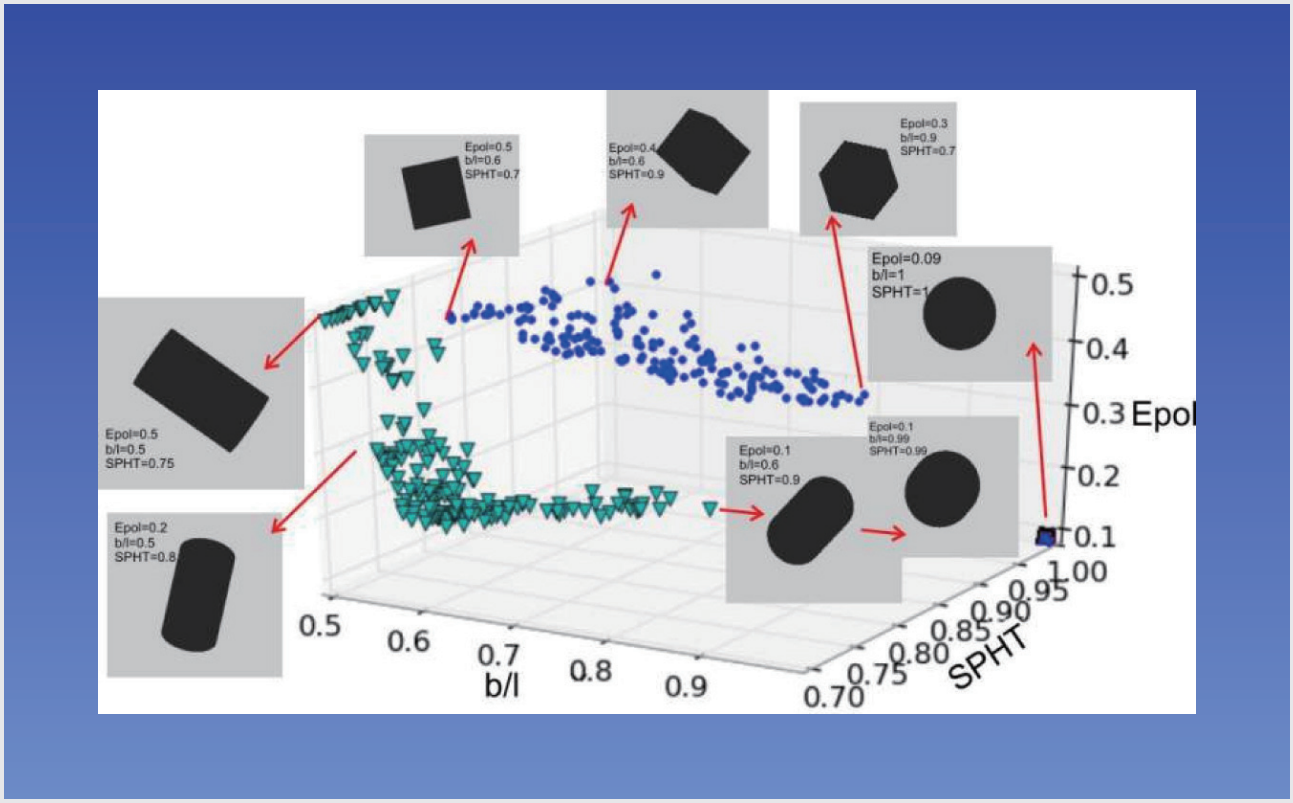

Figure 5 CLUSTER ANALYSIS: Simulation data with cubes, spheres & cylinders

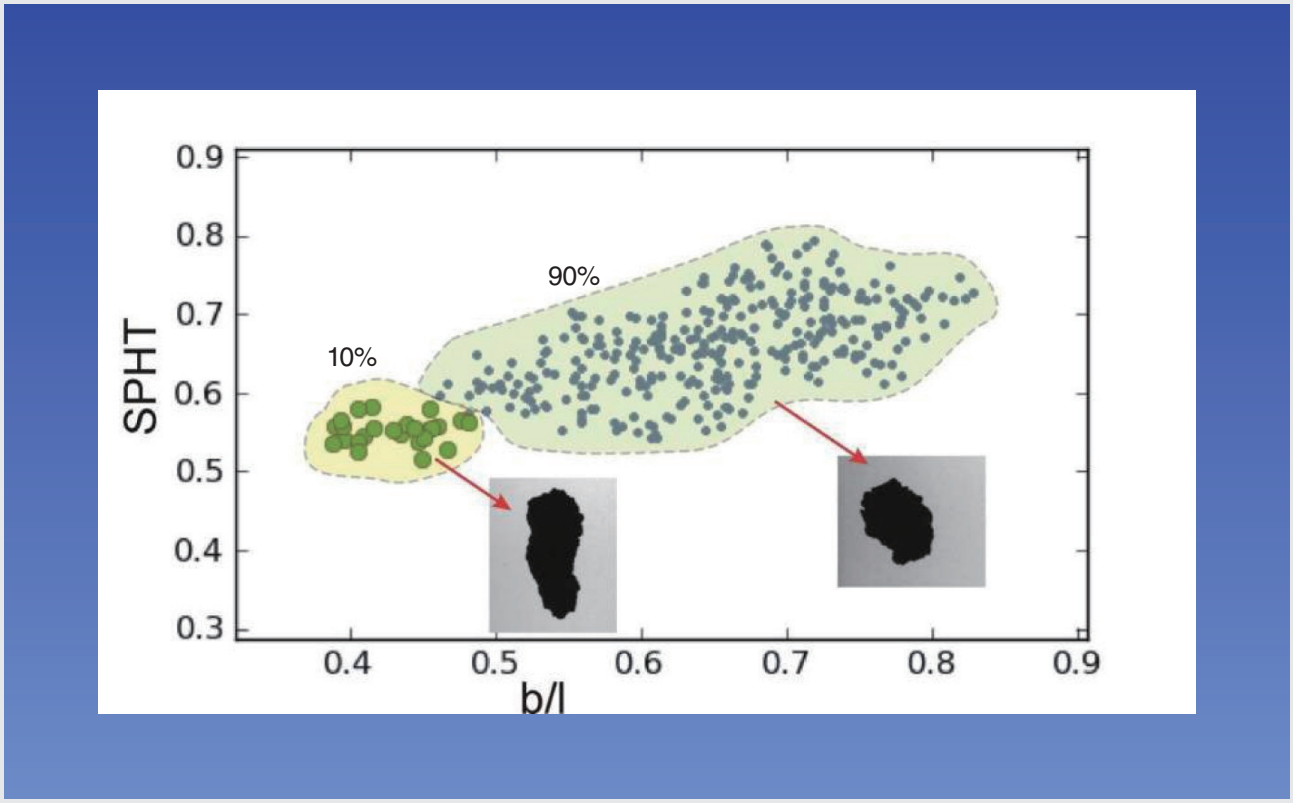

Figure 6 CLUSTER ANALYSIS: Lapilli from Etna volcano

CONCLUSIONS

Probably the first question is how general is this approach to the description of volcanic ash? This data is from separate sets of samples from two volcanoes. Would it be observed for most all volcanic material? Assuming that the answer to this question is affirmative, could each cluster be individually characterized so that these clusters could be used to predict plume behavior? This is very critical because the penultimate goal is to reduce the characteristic shape and size from millions of ash particles into a few useable cluster parameters that would have some predictive value. Once these clusters are identified, next their behavior characteristics must be measured for the parameter of interest, setting velocity.

The next step would be to sum up the characteristics of each cluster into a total sample characteristic. If the hypothesis is correct, this final sample characteristic would correlate to the plume dispersal. The model would then be tested with a number of different eruption samples to determine the applicability of the sample characteristic. If most samples correlated to the plume dispersal which would be independently determined, this would be validation for cluster analysis model. This final determination is a number of years away, but at least a test protocol exists to examine actual sample data.

If this model proved correct, it would prove valuable in a variety of ways. It could predict the dangers associated with living in the general area of an active volcano. It could be used to predict the danger of the plume to general aviation in the immediate vicinity. It could also be used for weather predictions based upon the effect of the volcanic explosion. These are still a bit off in the future, but the first steps toward the predictions have been taken.

ACKNOWLEDGEMENTS

The author wishes to thank Gert Beckmann of Retsch Technology for contributing much of the technical data used in this paper.

Reference

[1] The Instruction Manual Grain Size Analyzer; Camsizer, Retsch Technology GmbH, 42781 Haan, Reinische Strasse 43, Germany.

Michael C. Pohl
Vice President
Scientific Instruments
HORIBA Instruments, Inc.
Ph. D.

HORIBA World-Wide Network

JAPAN

HORIBA, Ltd.
Head Office Factory
2, Miyanohigashi-cho, Kisshoin, Minami-ku Kyoto 601-8510
Phone : (81)75-313-8121 Fax : (81)75-321-8312

HORIBA STEC, Co.,Ltd.
11-5, Hokodate-cho, Kamitoba, Minami-ku Kyoto 601-8116
Phone : (81)75-693-2300 Fax : (81)75-693-2350

HORIBA Advanced Techno Co.,Ltd.
31, Miyanonishi-cho, Kisshoin, Minami-ku Kyoto 601-8306
Phone : (81)75-321-7184 Fax : (81)75-321-7291

HORIBA Techno Service Co.,Ltd.
2, Miyanohigashi-cho, Kisshoin, Minami-ku Kyoto 601-8305
Phone : (81)75-325-5291 Fax : (81)75-315-9972

HORIBA ITECH Co.,Ltd.
2, Miyanohigashi-cho, Kisshoin, Minami-ku Kyoto 601-8510
Phone : (81)75-326-1700 Fax : (81)75-326-0300

U.S.A.

HORIBA International Corporation
17671 Armstrong Avenue Irvine, CA 92614
Phone : (1)949-250-4811 Fax : (1)949-250-0924

HORIBA Instruments Inc.
Irvine Facility
17671 Armstrong Avenue Irvine, CA 92614
Phone : (1)949-250-4811 Fax : (1)949-250-0924

Ann Arbor Facility
5900 Hines Drive Ann Arbor, MI 48108
Phone : (1)734-213-6555 Fax : (1)734-213-6525

HORIBA STEC Inc.
HORIBA Technology Center
3265 Scott Boulevard Santa Clara, CA 95054
Phone : (1)408-730-4772 Fax : (1)408-730-8975

New Hampshire Office
315 Derry Road Suite 13 Hudson, NH 03051
Phone : (1)603-886-4167 Fax : (1)603-886-4267

Portland Office
10240 SW. Nimbus Avenue Suite L-5 Portland, OR 97223
Phone : (1)503-624-9767 Fax : (1)503-968-3236

Austin Office
9701 Dessau Road Suite 605 Austin, TX 78754
Phone : (1)512-836-9560 Fax : (1)512-836-8054

Reno Office
605 Spice Island Drive #5 Sparks, NV 89431
Phone : (1)775-358-2332 Fax : (1)775-358-0434

HORIBA Automotive Test Systems Corp.
2890 John R Road Troy, MI 48033
Phone : (1)248-689-9000 Fax : (1)248-689-8578

HORIBA ABX Inc.
34 Bunsen Drive Irvine Spectrum, Irvine, CA 92618
Phone : (1)949-453-0500 Fax : (1)949-453-0600

HORIBA Jobin Yvon Inc.
3880 Park Avenue Edison, NJ 08820
Phone : (1)732-494-8660 Fax : (1)732-549-5125

CANADA

HORIBA Automotive Test Systems Inc.
555 North Service Road, Unit 102 Burlington Ontario L7L SH7
Phone : (1)905 335 0234 Fax : (1)905-827-8162

BRAZIL

HORIBA ABX Brazil
Av. das Nações Unidas, 21.735 = Jurubatuba São Paulo CEP 04795-100
Phone : (55)11-55-45-1500 Fax : (55)11-55-45-1570

TCA/HORIBA Sistemas de Testes Automotivos Ltda.
Rua Osvaldo Cruz, 1.056 - Sta.Paula - CEP: 09540-280 S. Caetano do Sul - SP
Phone : (55)11-4224-0205 Fax : (55)11- 4227- 3133

RUSSIA

HORIBA, Ltd. Moscow Representative Office
Build 5, h.13, Altuf'evskoe shosse Moscow 127106
Phone : (7)495-221-87-71 Fax : (7)495-221-87-68

GERMANY

HORIBA Europe GmbH / Oberursel Office
Hans-Mess-Strasse 6 D-61440 Oberursel / Ts.
Phone : (49)6172-1396-0 Fax : (49)6172-137385

Darmstadt Office
Landwehr-Strasse 55 D-64293 Darmstadt
Phone : (49)6151-5000-0 Fax : (49)6151-5000-3865

Hanover Office
Bayern-Strasse 29 D-30855 Langenhagen
Phone : (49)511-741095 Fax : (49)511-741053

Leichlingen Facility
Julius-Kronenberg-Strasse 9 D-42799 Leichlingen
Phone : (49)2175-89780 Fax : (49)2175-897850

Munich Office
Josephsburg-Strasse 88a b-81673
Phone : (49)89-2444779-0 Fax : (49)89-2444779-10

Potsdam Office
Neuendorfer-Strasse 39a D-14480 Potsdam
Phone : (49)331-6490070 Fax : (49)331-6490074

Stuttgart Office (Neuhausen)
Zabergaeu-Strasse 2, D-73765 Neuhausen
Phone : (49)7158-933-800 Fax : (49)7158-933-899

Stuttgart Office (Boblingen)
Hans-Klemm-Strasse 56 D-71034 Böblingen
Phone : (49)7031-677-9440 Fax : (49)7031-677-9450

HORIBA Europe Automation Division GmbH
Zabergau-Strasse 3, D-73765 Neuhausen
Phone : (49)7158-933-300 Fax : (49)7158-933-399

HORIBA Jobin Yvon GmbH
Haupt-Strasse 1, 82008 Unterhacing
Phone : (49)89-46231-70 Fax : (49)89-46231-799

Raman Division
Neuhof-Strasse 9 D-64625 Bensheim
Phone : (49)6251-84750 Fax : (49)6251-847520

FRANCE

HORIBA France SARL
12 Av. des Tropiques Hightec Sud F-91955 Les Ulis
Phone : (33)1-69-29-96-23 Fax : (33)1-69-29-95-77

HORIBA ABX S.A.S.
Parc Euromedecine, Rue du Caducée – BP 7290 34184 Montpellier Cedex 4
Phone : (33)4-67-14-15-16 Fax : (33)4-67-14-15-17

HORIBA Jobin Yvon S.A.S.
16-18 rue du Canal 91165 Longjumeau Cedex
Phone : (33)1-64-54-13-00 Fax : (33)1-69-09-07-21

Thin Films Division
5 auenoe Arago, ZA dela Vigne aux Lous 91380 Chilly Mazarin
Phone : (33)1-69-74-88-60 Fax : (33)1-69-74-88-61

Raman Division
231 Rue de Lille 59650 Villeneuve D'ascq
Phone : (33)3-20-59-18-00 Fax : (33)3-20-59-18-08

BELGIUM

HORIBA ABX S.A.S. Belgium Branch
Luchthavenlei 7A Deurne 2100
Phone : (32)3-281-49-08 Fax : (32)3-281-65-04

ITALY

HORIBA Europe GmbH Torino Office
Europalace, Corso, Torino 43/45 10043 Orbassano Torino
Phone : (39)011-904-0601 Fax : (39)011-900-0448

HORIBA ABX S.A.S. Italy Branch
Via Le Luca Gaurico 209/211, 000143 Roma
Phone : (39)6-51-59-22-1 Fax : (39)6-51-96-43-34

HORIBA Jobin Yvon Srl
Via Cesare Pavese 35AB, 20090 Opera Milano
Phone : (39)2-57-60-30-50 Fax : (39)2-57-60-08-76

SPAIN

HORIBA ABX S.A.S. Spain Branch
Avenida Caidos de la Division Azul 16 Madrid 28016
Phone : (34)91-353-30-10 Fax : (34)91-353-30-11

HORIBA Jobin Yvon S.A.S. Spain Branch
Edificio Alcor 1 Bajo 3, Avenida Valdelaparra 27 Alcobendas Madrid 28108
Phone : (34)91-724-16-57 Fax : (34)91-724-13-73

PORTUGAL

HORIBA ABX S.A.S. Portugese Branch
Rua Alfredo da Silva, 8-A, 3C, Quinta Grande Alfragide Amadora 2610-016
Phone : (351)214-72-17-70 Fax : (351)214-72-17-89

AUSTRIA

HORIBA GmbH
Kaplanstrasse 5 A-3430 Tulln
Phone : (430)2272-65225 Fax : (430)2272-65230

CZECH REPUBLIC

HORIBA GmbH Czech Office
Edificio Alcor 1 Bajo 3, Avenida Valdelaparra 27 Alcobendas Madrid 28108
Phone : (42)2717-46480 Fax : (42)2717-47064

SWEDEN

HORIBA Europe GmbH
Sodertalje Office
Sydhamnsvägen 55-57 S-15138 Sodertalje
Phone : (46)8550-80701 Fax : (46)8550-80567

Gothenburg Office
Kaerrlyckegatan 21 S-418 78 Gothenburg
Phone : (46)3164-4268 Fax : (46)3164-4269

NETHERLANDS

HORIBA Europe GmbH Netherland Office
Science Park 5080 (Ekkersrijt) 5692 EA SON
Phone : (31) 40-2900240 Fax : (31)40-2900624

U.K.

HORIBA Instruments Ltd.
Kyoto Close, Summerhouse Road, Moulton Park Northampton NN3 6FL
Phone : (44)1604-542-500 Fax : (44)1604-542-699

HORIBA ABX S.A.S.
Kyoto Close, Summerhouse Road, Moulton Park Northampton NN3 6FL
Phone : (44)1604-542650 Fax : (44)1604-542651

HORIBA Jobin Yvon Ltd.
2 Dalston Gardens Stanmore Middlesex HA7 1BQ
Phone : (44)20-8204-8142 Fax : (44)20-8204-6142

HORIBA Jobin Yvon IBH Ltd.
Skypark 5, Level 1, The Clydeway Centre, 45 Finnieston Street, Glasgow G3 8JU
Phone : (44)141-229-67-89 Fax : (44)141-229-67-90

HORIBA STEC, Co.,Ltd.
Kyoto Close, Summerhouse Road, Moulton Park Northampton NN3 6FL
Phone : (44)1604-542-600 Fax : (44)1604-542-696

SRH Systems Ltd.
Evesham House, Whittington Hall, Whittington Road, Worcester WR5 2ZX
Phone : (44)1905-359359 Fax : (44)1905-359332

Kore Technology Limited
5 Bartholemew's Walk Cambridgeshire Business Park Ely Cambridgeshire CB7 4EA
Phone : (44)0-1353-653035 Fax : (44)0-1353-653031

POLAND

HORIBA ABX Sp. Zo. o.
ul. Wal Miedzeszynski 598-03 994 Warzsawa
Phone : (48)22-673-2022 Fax : (48)22-67-32-026

KOREA

HORIBA Korea Ltd.
202-501 Pucheon Techno Park, 192 Yakdae-Dong, Wonmi-ku Pucheon Kyonggi-do
Phone : (82)32-621-0100 Fax : (82)32-621-0105

Seoul Office
112-6 Sogong-Dong Choong-ku Seoul
Phone : (82)2-753-7911 Fax : (82)2-756-4972

Suwon Office
399-12, 20 Yuljun-Dong Changan-ku Suwon Kyunggido
Phone : (82)31-296-7911 Fax : (82)31-296-7913

Ulsan Office
601, Kaya Bldg, 193-5, Singeong 3 Dong Nam-ku Ulsan
Phone : (82)52-275-0122 Fax : (82)52-276-0136

HORIBA Automotive Test Systems Ltd.
Room #906, World Meridian Venture Centre I, 60-24 Gasan-Dong Geumcheon-Gu Seoul 153-78
Phone : (82)25-62-72-06 Fax : (82)25-62-76-30

HORIBA STEC Korea, Ltd.
110 Suntech-City, 513-15 Sangdaewon Jungwon-ku, Sungnam-city Kyungki-do
Phone : (82)31-777-2277 Fax : (82)31-777-2288

SINGAPORE

HORIBA Instruments (Singapore) PTE, Ltd.
No.200, Taitao Rd, Anting Town, Jiading District, Shanghai 201814
Phone : (65)6745-8300 Fax : (65)6745-8155

CHINA

HORIBA Instruments (Shanghai) Co., Ltd.
No.200, Taitao Rd, Anting Town, Jiading District, Shanghai 201814
Phone : (86)21-6952-2835 Fax : (86)21-6952-2823

HORIBA Trading (Shanghai) Co., Ltd.
United Plaza, Room 1701, 1468 Nanjing Road West Shanghai 200040
Phone : (86)21-6289-6060 Fax : (86)21-6289-5553

Shanghai Zhangjiang Service Center (for Semiconductor business)
Room 303, No.84, Lame 887, Zu-chong-zhi Road, Zhangjiang Hi-tech Park Shanghai 201203
Phone : (86)21-5131-7150 Fax : (86)21-5131-7660

Beijing Branch Office
Room 1801, Capital Tower Beijing, Tower 1 No.6Jia, Jianguomenwai Ave. Chaoyang District Beijing 100022
Phone : (86)10-8567-9966 Fax : (86)10-8567-9066

Guangzhou Office
Room 1810, Golden Digital Network Center,138 Tiyu Road East Guangzhou 510620
Phone : (86)20-3878-1883 Fax : (86)20-3878-1810

TAIWAN

HORIBA, Ltd. Taiwan Representative Office
3F,No.18,Lane 676,Chung-Hua Rd.,Chupei City Hsinchu Hsien 302
Phone : (886)3-656-1012 Fax : (886)3-656-1650

HORIBA STEC, Co., Ltd. Taiwan Branch
3rd Fl., No18, lane 676, Jhonghua Rd., Jhubei City, Hsinchu Conty 302
Phone : (886)3-656-1160 Fax : (886)3-656-8231

Tainan Office
1F., No.117, Chenggong Rd., Shanhua Township Tainan County 741
Phone : (886)6-583-4592 Fax : (886)6-583-2409

INDIA

HORIBA India Private Ltd.
246, Okhla Industrial Estate, Phase - III 110 020 New Delhi
Phone : (91)11-4669-5001 Fax : (91)11-4669-5010

Pune Office
502, 5th Floor, Purushottam Plaza,Baner Road, Baner, Pune - 411045
Phone : (91)20-2729-1121

Bangalore Office
Golden Square Business Centre 53/A, 16th C Main, 4th block, Koramangala, Bangalore - 560034
Phone : (91)80-4261-3203 Fax : (91) 80-4092-9225

HORIBA ABX S.A.S. India Representative Office
246, Okhla Industrial Estate, Phase - III 110 020 New Delhi
Phone : (91)11-4646-5000 Fax : (91)11-4646-5020

THAILAND

HORIBA ABX Diagnostics Thailand Ltd
395, Latya Road, Somdetchaopraya Sub-district Klongsan District Bangkok 10600
Phone : (66)2-861-59-95 Fax : (66)2-861-52-00

Readout **HORIBA Technical Reports English Edition No.38**

Publication Date : May 24th, 2011
Publisher : HORIBA, Ltd.
Editor : Kozo Ishida
Associate Editor : Seiji Usui
Publication Member : Donna Merithew, Keiko Saito, Hideyo Seki
DTP, Printing : SHASHIN KAGAKU CO.,LTD.
Imformation : Legal Affairs and Intellectual Property Center, HORIBA, Ltd.
2, Miyanohigashi-cho, Kisshoin, Minami-ku, Kyoto 601-8510, Japan
Phone : (81)75-313-8121 Fax : (81)75-321-5648
E-mail : readout@horiba.co.jp
http://www.horiba.com/publications/readout/

HORIBA

Explore the future

Printed on 100% recycled paper.

This article is printed using environment-friendly process qualified as SILVER status by E3PA. E3PA : Environment Pollution Prevention Printing Association http://www.e3pa.com